

A NEW METHOD FOR CHARACTERIZING SPINDLE
RADIAL ERROR MOTION: A TWO- DIMENSIONAL
POINT OF VIEW

by

Arash Jamalian

B.A.Sc., Simon Fraser University, 2008

A THESIS SUBMITTED IN PARTIAL FULFILMENT OF
THE REQUIREMENTS FOR THE DEGREE OF

MASTER OF APPLIED SCIENCE

in

The Faculty of Graduate Studies

(Mechanical Engineering)

THE UNIVERSITY OF BRITISH COLUMBIA

(Vancouver)

May 2010

© Arash Jamalian, 2010

Abstract

This thesis presents a new two dimensional (2D) method based on complex Fourier series to characterize spindle radial error motions. One subtlety of spindle metrology is that the radial motion measurements have an undesired component caused by the ball installation eccentricity. The current standard methods cannot distinguish between this undesired component and fundamental radial error motion of spindle. The new 2D method identifies what fundamental radial error motion is and how it can be distinguished from the test ball installation eccentricity.

Current standard methods give the consequence of radial error motion in two classes of spindle applications, but not the radial error motion itself. By identifying the fundamental radial error motion, the 2D method can not only determine the axis of rotation radial error motion, but also the consequence of error motion in all classes of spindle applications, including a new class of applications with two radial sensitive directions.

Experiments are carried out on two types of spindles to confirm that fundamental radial error motion not only exists but it can have a magnitude higher than any other error motion component. The 2D method is used to find the actual radial error motion of the spindles as well as the consequence of error motion in applications. Possible physical causes of the fundamental error motion are also discussed and experiments are carried out to identify their actual effect on the spindles under test.

Table of Contents

Abstract.....	ii
List of Tables	vi
List of Figures.....	vii
Nomenclature.....	xi
Acknowledgements.....	xiii
Dedication.....	xv
Chapter 1. Introduction.....	1
1.1. Axis of rotation error motion	1
1.2. Prior art in measuring axes of rotation.....	2
1.2.1. The current ISO and ASME/ANSI standards.....	2
1.2.2. Radial error motion in two dimensions	7
1.3. Existing methods for specifying axis of rotation error motion	8
1.4. Current standard methods vs. 2D method.....	10
1.4.1. Radial error motion and its consequence.....	10
1.4.2. Fundamental radial error motion	11
1.4.3. Applications with two radial sensitive directions.....	12
1.5. Thesis overview	12
Chapter 2. Two-dimensional radial motion theory	14
2.1. Metrology reference frame.....	15
2.2. Test point radial motion	16
2.3. Axis of rotation radial error motion.....	21
2.3.1. Concept of axis of rotation	21
2.3.2. Perfect spindle	22
2.3.3. Axis of rotation radial error motion.....	23
2.3.4. Factors affecting spindle motion components	28
2.3.5. Illustration of fundamental radial error motion	28
2.4. Radial error motion consequence in various spindle applications.....	32
2.4.1. Applications with single radial sensitive direction.....	34
2.4.1.1. Applications with single fixed radial sensitive direction (SFSD).....	35
2.4.1.2. Applications with single rotating radial sensitive direction (SRSD)	36

2.4.2.	Applications with two sensitive directions (TSD).....	38
2.4.3.	Case study: Beam writing on a spindle with fundamental radial error motion	40
2.4.3.1.	Axis-symmetric pattern writing with one tool	41
2.4.3.2.	Axis-asymmetric pattern writing with one tool.....	42
2.4.3.3.	Axis-symmetric pattern writing with multiple tools	43
2.4.4.	Case study: Multi-tool boring on a spindle with 2-cpr error motion	45
2.5.	Comparison between 2D method and current standard methods.....	46
2.5.1.	Implementation of the current standard methods in the 2D framework	47
2.5.2.	Case study: spindle with 1,2, and 3 cpr radial error motion	48
Chapter 3.	Experimental results	50
3.1.	General consideration	50
3.1.1.	Probe misalignment with the target ball center	50
3.1.2.	Target ball curvature.....	51
3.1.3.	Aliasing.....	55
3.1.4.	Indexing error	56
3.2.	Experiments on a ball bearing spindle	57
3.2.1.	Experimental results at 1000 rpm	58
3.2.1.1.	Test ball motion measurement	58
3.2.1.2.	Spindle 2D radial error motion.....	61
3.2.1.3.	Comparison with current standards.....	62
3.2.2.	Experimental results at 4000 rpm	63
3.2.2.1.	Test ball motion measurement	63
3.2.2.2.	Spindle 2D radial error motion.....	66
3.2.2.3.	Comparison with current standards.....	66
3.2.3.	Experiments across speed	67
3.3.	Experiments on an aerostatic bearing spindle.....	70
3.3.1.	Radial error motion measurements using the ball-probe setup	72
3.3.1.1.	Measurement procedures and theories	72
3.3.1.2.	Experimental results at 400 rpm.....	74
3.3.1.3.	Comparison with current standards.....	80
3.3.2.	Radial error motion measurements using the ring-probe setup	81
3.3.3.	Radial error motion measurements using the four encoder head setup	84

3.3.4.	Comparison of three methods for spindle motion measurement	86
Chapter 4.	Physical causes of fundamental error motion	89
4.1.	Interaction between unbalance and spindle bearing axis-asymmetric stiffness.....	90
4.1.1.	Unbalance	91
4.2.	Interaction between unbalance and supporting structure axis-asymmetric stiffness	93
4.3.	Interaction between off-axis load and spindle bearing axis-asymmetric tilt stiffness	94
4.4.	Rotor surface misalignment and spindle bearing axis-asymmetric tilt stiffness.....	96
4.5.	Interaction between magnetized rotor and stator	97
4.6.	Physical cause experiments on the ball bearing spindle	98
4.7.	Physical cause experiments on the aerostatic bearing spindle	100
4.7.1.	Unbalance experiment	100
4.7.2.	Tilt stiffness measurement	104
4.7.3.	Other physical factors affecting $V(-I)$	106
4.7.3.1.	Loose bolt test	106
4.7.3.2.	Drift test.....	107
Chapter 5.	Conclusion and future work.....	109
5.1.	Conclusion	109
5.2.	Future work	110
5.2.1.	Experimental setup modifications	110
5.2.2.	Cause of fundamental radial error motion	112
References	113
Appendices	115
Appendix A	115
Appendix B	117
Appendix C	119
Appendix D	122

List of Tables

Table 2-1. Various 2D error motion values of the numerical example.	27
Table 2-2. Spindle error motion calculation.	31
Table 2-3. Radial error motion comparison between the current standards and the 2D method..	48
Table 3-1. Sensors and data acquisition system.....	58
Table 3-2. Sensors and data acquisition system.....	71
Table 4-1. Types of interaction which cause spindle synchronous error motion.	89
Table 4-2. Types of interaction which cause spindle fundamental radial error motion.	90

List of Figures

Figure 1.1. Types of axis of rotation error motion.....	2
Figure 1.2. Tlusty’s rotating sensitive direction method setup. Redrawn from [3]......	3
Figure 1.3. Numerical example illustration of Tlusty’s rotating sensitive direction method.	4
Figure 1.4. Bryan’s fixed sensitive direction method. Redrawn from [5].	4
Figure 1.5. Numerical example illustration of Bryan’s fixed sensitive direction.	5
Figure 1.6. Vanherck and Peters digital measurement setup. Redrawn from [6].	6
Figure 1.7. Numerical example illustration of existing methods to specify radial error motion in two dimensions.	7
Figure 1.8. Numerical example illustration of two existing methods of specifying radial error motion from polar plots.	9
Figure 2.1. Typical metrology setup: (a) 3D model. (b) 2D cross-sectional view at the specified axial location.	14
Figure 2.2. Spindle radial error motion analysis sequences.....	15
Figure 2.3. A numerical example of the X and Y components of the test ball 2D motion. Data over four revolutions are overlaid together.	17
Figure 2.4. Test ball’s synchronous and asynchronous motion of the numerical example: (a) Synchronous radial motion in X. (b) Synchronous radial motion in Y. (c) Asynchronous radial motion in X. (d) Asynchronous radial motion in Y.	18
Figure 2.5. Physical meaning of $V(I)$ Fourier coefficient.....	19
Figure 2.6. Fourier coefficients of the test ball’s synchronous motion for the numerical example.	20
Figure 2.7. Vector representation of point P’s synchronous radial motion for the numerical example.	20
Figure 2.8. The concepts of axis of rotation and axis average line.....	21
Figure 2.9. Relation between the average point A, the rotation center C, and the test ball center P on a perfect spindle. The dashed arrow line indicates the rotary position of the spindle rotor. Points A and C coincide. The distance between C and P is the eccentricity of the test ball installation.....	23
Figure 2.10. Relation between the average point A, the rotation center C, and the test ball center P on a spindle with radial error motion. The dashed arrow line indicates the rotary position of the spindle rotor. The vector $\varepsilon(\theta)$ from A to C is the spindle radial error motion at the current angular position. The distance between C and P is the eccentricity of the test ball installation... ..	24
Figure 2.11. The Axis of rotation 2D radial error motion Fourier coefficients of the numerical example.	26
Figure 2.12. The Axis of rotation 2D radial error motion components of the numerical example.	27
Figure 2.13. Vector representation of the 2D radial error motion of the numerical example.	27

Figure 2.14. Comparison between a perfect spindle (a) and a spindle with fundamental radial error motion.	30
Figure 2.15. Vector decomposition of test point motion: (a) Perfect spindle. (b) Spindle with fundamental radial error motion.	31
Figure 2.16. Categories of spindle applications based on radial sensitive direction	33
Figure 2.17. The relation between $\varepsilon(\theta)$ (radial error motion) and $\varepsilon_{\phi}(\theta)$ (the radial error motion in a specified direction).....	34
Figure 2.18. Comparison between the spindle radial error motion and its consequence in applications with single radial sensitive direction: (a) in X direction, (b) in Y direction, and (c) in a rotating direction.	38
Figure 2.19. Face turning of axis-asymmetric patterns with a fast tool servo.	39
Figure 2.20. Axis-asymmetric pattern turning on a drum lathe with a fast tool servo.	40
Figure 2.21. A rotary beam writing machine.	41
Figure 2.22. The simulated pattern when the desired pattern is a circle. The origin is the spindle rotation center.	42
Figure 2.23. Simulated result of axis-asymmetric pattern writing with single beam. Instead of lines, only discrete points are shown.	43
Figure 2.24. A multi-beam rotary writing machine.	43
Figure 2.25. Axis-symmetric pattern writing with two beams. (a) the desired pattern. (b) the produced pattern on a spindle with fundamental radial error motion.	44
Figure 2.26. Multi-tool boring operation. Four concentric holes are produced in a single boring operation.	45
Figure 2.27. Holes produce by two orthogonal boring tools.	46
Figure 3.1. Effect of probe misalignment on measuring the motion of target ball least squares center P_{ball}	51
Figure 3.2. Lion precision capacitance probe against a spherical target.....	52
Figure 3.3. Effect of a spherical target on the sensed capacitance of C2-A probe (50- μ m stroke).	53
Figure 3.4. Effect of a spherical target on the sensed capacitance of C5-D probe (10- μ m stroke).	53
Figure 3.5. Finding adjustment factor for C2-A probe (50- μ m stroke).	54
Figure 3.6. Finding adjustment factor for C5-D probe (10- μ m stroke).	54
Figure 3.7. Typical data acquisition setup.	55
Figure 3.8. Data acquisition setup used in the experiments.	56
Figure 3.9. Indexing error on the spindle metrology setup.	57
Figure 3.10. Radial error motion measurement setup of the ball bearing spindle.	58
Figure 3.11. Test ball motion measurement data over 20 revolutions at 1000 rpm.	59
Figure 3.12. Test ball synchronous 2D motion on the ball bearing spindle at 1000 rpm.	60
Figure 3.13. Fourier coefficients of the test ball 2D motion at 1000 rpm.	60
Figure 3.14. The test ball asynchronous motion in X and Y directions at 1000 rpm.	61

Figure 3.15. The ball bearing spindle synchronous radial error motion measurement result at 1000 rpm.	62
Figure 3.16. Radial error motion comparison between the current standards and the new 2D method.....	63
Figure 3.17. Test ball motion measurement over 20 revolutions at 4000 rpm.	64
Figure 3.18. Test ball synchronous 2D motion on the ball bearing spindle at 4000 rpm.	64
Figure 3.19. Fourier coefficients of the test ball 2D radial motion at 4000 rpm.	65
Figure 3.20. The test ball asynchronous motion in X and Y directions at 4000 rpm.	65
Figure 3.21. The test ball asynchronous motion in X and Y directions at 4000 rpm.	66
Figure 3.22. Radial error motion comparison between the current standards and the 2D method.	67
Figure 3.23. Test ball motion at 4000 rpm and 4500 rpm	68
Figure 3.24. Spindle 2D radial error motion Fourier coefficients versus speed.	69
Figure 3.25. The change of axis of rotation position relative to the test ball center, $V_p(+1)$	70
Figure 3.26. Aerostatic bearing spindle test setups.....	71
Figure 3.27. Four steps in spindle radial error motion test using setup (a).....	73
Figure 3.28. Probe measurement results at 400 rpm from the four steps. 20 revolutions are overlaid.	74
Figure 3.29. Synchronous component of the measurements from the four steps at 400 rpm.....	75
Figure 3.30. Asynchronous component of the measurements from the four steps at 400 rpm. ...	76
Figure 3.31. The test ball out-of-roundness.	77
Figure 3.32. Target ball synchronous 2D motion of the aerostatic bearing spindle at 400 rpm, using the ball-probe setup. (a) X_B motion versus rotary angle. (b) Y_B motion versus rotary angle. (c) Y_B versus X_B motion trace plot.	78
Figure 3.33. A second test of the target ball synchronous 2D motion at 400 rpm. The target ball installation location on the rotor is changed to a rotor location different from the one in Figure 3.32 results. (a) X_B motion versus rotary angle. (b) Y_B motion versus rotary angle. (c) Y_B versus X_B motion trace plot.....	79
Figure 3.34. Spindle radial error motion measurement results from two tests with very different target ball eccentricity.....	80
Figure 3.35. Radial error motion comparison between the current standards and the 2D method.	81
Figure 3.36. The ring-probe setup for axis of rotation radial error motion measurement.	82
Figure 3.37. Probe measurement results at 400 rpm using the ring-probe setup. 500 revolutions are overlaid.....	83
Figure 3.38. Synchronous motion of the ring-probe setup measurements.	83
Figure 3.39. Asynchronous radial error motion results.	84
Figure 3.40. Setup (c): radial error motion measurement using four encoder scanning heads.....	85
Figure 3.41. Calibrated encoder error maps of four encoder scanning heads at 400 rpm.	86
Figure 3.42. Relationship between the measurement coordinate of the three setups	87
Figure 3.43. Comparison of the fundamental radial error motion measurement $V(-1)$ results from the three setups.....	88

Figure 4.1. Axis symmetric air gap between rotor and stator of an aerostatic bearing spindle at zero speed.....	91
Figure 4.2. An unbalanced spindle with axis-asymmetric radial stiffness.	93
Figure 4.3. Axis-asymmetric stiffness of a five axis machine.....	94
Figure 4.4. Axis-asymmetric stiffness of a diamond turning machine.....	94
Figure 4.5. Off-axis load on a rotary table.....	95
Figure 4.6. An aerostatic spindle with misaligned rotor thrust plate and elliptical stator surface. a) spindle rotor and stator. b) assembled rotor and stator.	97
Figure 4.7. Interaction between a spindle stator and rotor's magnetic fields.	98
Figure 4.8. Experimental setup for radial compliance measurement.....	99
Figure 4.9. Spindle compliance measurement test results.	100
Figure 4.10. Unbalance mass mounted on the aerostatic spindle rotor.	101
Figure 4.11. Effect of unbalance mass on magnitude of $V_{P(+I)}$	102
Figure 4.12. Effect of unbalance mass on phase of $V_{P(+I)}$. a) Phase of $V_{P(+I)}$ for all the mounting positions, b) difference between $V_{P(+I)}$ phases shown in (a).	102
Figure 4.13. Effect of unbalance mass on magnitude of $V_{P(-I)}$	103
Figure 4.14. Effect of unbalance mass on phase of $V_{P(-I)}$. a) Phase of $V_{P(+I)}$ for all the mounting positions, b) difference between $V_{P(+I)}$ phases shown in (a).	104
Figure 4.15. Experimental setup for tilt stiffness measurement.	104
Figure 4.16. Measuring static deformation of the the aerostatic spindle.	105
Figure 4.17. Static tilt stiffness of the aerostatic spindle.	106
Figure 4.18. Aerostatic bearing assembly solid model.	107
Figure 4.19. Effect of loosening the stator bolts on $V(-I)$	107
Figure 4.20. Change in $V(-I)$ due to temperature and pressure change.....	108
Figure 5.1. Modying aerostatic bearing spindle setup for more accurate radial error measurements.....	112
Figure B. 1. Example polar plot with centering error.	117
Figure D. 1. Experimental setup for radial compliance measurement.....	122
Figure D. 2. Spindle compliance measurement test results.	123

Nomenclature

θ	spindle rotary continuous position
n	index for spindle discrete rotary position
x_p	test ball motion in the X direction
y_p	test ball motion in the Y direction
\bar{v}_p	test ball synchronous 2D radial motion
\bar{x}_p	test ball synchronous motion component in the X direction
\bar{y}_p	test ball synchronous motion component in the Y direction
\tilde{v}_p	test ball asynchronous 2D radial motion
\bar{V}_p	Fourier coefficients of \bar{v}_p
\bar{X}_p	Fourier coefficients of \bar{x}_p
\bar{Y}_p	Fourier coefficients of \bar{y}_p
v_A	average location of the rotation center
v_C	spindle rotation center radial motion
\bar{v}_C	spindle rotation center synchronous radial motion
\tilde{v}_C	spindle rotation center asynchronous radial motion
ε	spindle radial error motion
$\bar{\varepsilon}$	spindle synchronous radial error motion
$\tilde{\varepsilon}$	spindle asynchronous radial error motion
ε_ϕ	spindle error motion in a specified radial direction
A_{ϕ_0}	radial error motion consequence in applications with single fixed radial sensitive direction
A_θ	radial error motion consequence in applications with single rotating radial sensitive direction
A	radial error motion consequence in applications with two radial sensitive directions
N	the number of sampling points per revolution
M	the number of revolutions used for synchronous and asynchronous motion calculation

- ϕ the angle between a specified radial direction and the X axis
- $\bar{\rho}_\theta$ radial error motion specified with the rotating sensitive direction method in the current standards
- $\bar{\rho}_{\phi_0}$ radial error motion specified with the fixed sensitive direction method in the current standards
- r_θ radial error motion polar plot for a rotating sensitive direction
- r_{ϕ_0} radial error motion polar plot for a fixed sensitive direction

Types of functions and variables

- (θ) continuous signals as a function of θ
- $[n]$ discrete signals with index n
- (k) k -th Fourier coefficient of continuous periodic signals
- $[k]$ k -th Fourier coefficient of discrete periodic signals

Acknowledgements

I am most thankful to my supervisor, Professor Xiaodong Lu for all his support and guidance. He thought me spindle metrology, introduced me to the spindle experts, and initiated a fruitful dialogue in the field about the concepts discussed in this research. It has been a very exciting two years with many heated discussions to demonstrate the truth about the spindle error motion. He took me to ASPE conference and gave me the opportunity to take part in the discussions and learn how to communicate most effectively. He transformed this research beyond my expectations and made it a thrilling experience.

I am thankful to Professor Yusuf Altintas and Professor Steve Feng for being in my thesis committee. Professor Altintas taught me machine tool structures and vibrations, MECH 592, which helped me in identifying causes of spindle error motion in this research. He also provided access to the Mori Seiki machine in UBC Manufacturing Automation Lab. Credits for initiating this research should also be given to Professor Altintas and Darcy Montgomery. Darcy first asked Professor Altintas about ANSI B89.3.4 and pointed out that in the current standards the removal of fundamental components from probe measurements would not be correct if fundamental components from two radial probes have different amplitudes. Professor Altintas forwarded Darcy's question to my supervisor which motivated him to develop the presented 2D analysis method.

Over the past two years, I got the chance to learn from many experts in the field of spindle metrology. Special thanks go to Don Martin, Dan Debra, Mel Liebers, and Tim Dalrymple whom I had a chance to meet in person. I would like to also thank Dave Arneson, James Bryan, Bob Donaldson, Alkan Donmez, W. Tyler Estler, Wolfgang Knapp, Paul Vanherck for their valuable questions and comments regarding this work.

Darya Amin-Shahidi, former graduate student at UBC, designed the aerostatic bearing spindle. He gave me a lot of help in the early stage of this research and was always enthusiastic to answer my questions regarding his design. Richard Graetz, another graduate student at UBC, had a significant contribution in the aerostatic bearing experiments. The result from his research, on-axis self-calibration of angle encoders, is also presented as an alternative proof of the existence of fundamental error motion.

During my studies at UBC, I was very fortunate to have the support of my great friends and colleagues. Azadeh Jamalian, my sister and best friend, has always inspired me to make the most

of my life. Darya Amin-Shahidi made my experience at UBC much more pleasant. Ata Naemi and Shadi Agha-Kazem Shirazi have been my classmates during my studies both at UBC and SFU. Ata helped me choose Precision Mechatronics Laboratory for my graduate studies. Shadi has always been a true friend and helped me beyond academic life. Markus Fengler helped me with the machine shop. Mustafa Kaymakci and Burak Sencer helped with the Mori Seiki machine. Irfan-ur-rab Usman and Kris Smeds worked alongside me in the past two years and gave me many useful feedbacks.

I was very fortunate to have my family with their tremendous encouragement alongside me. My mother has made many sacrifices to give me the opportunity to study at UBC. My uncle, Mohsen Jamalian, encouraged me to pursue graduate studies and provided me with an incredible support.

This project is supported by Natural Sciences and Engineering Research Council of Canada (NSERC). KLA-Tencor provided most of the test equipments.

To my dad

Chapter 1. Introduction

Error motion of axis rotation is a major criterion for evaluating accuracy of machine tools. By the turn of the 20th century, primitive techniques were available to measure the spindle runout [1]. Usually the measurement was carried out by attaching a mandrel to the spindle and measuring the movement of the mandrel's surface using a dial indicator. Schlesinger, in 1927, was first to publish standards for spindle runout to set a benchmark for accuracy of machine tools.

Over the past few decades, techniques were developed to extract the error motion of the spindle from the run out measurements and predict the quality of the finished work piece. In 1985, American National Standards Institute (ANSI) adopted a standard which fully describes the testing of axes of rotation and its terminology (ANSI/ASME B89.3.4 M [2]). International Organization for Standardization (ISO) later published its own version: ISO 230-7 [3]. These techniques were generally focused on traditional machining operations such as turning and boring where there is a single sensitive direction.

Today, spindles are not restricted to generating axis-symmetric patterns. Some processes, such as FTS-assisted turning, machining of non-round holes, and rotary beam writing, are simultaneously sensitive to radial error motion in two dimensions. To evaluate spindle performance for these applications, a new 2D method is developed based on complex Fourier series. This method gives a new perspective of the motion of axis of rotation and reveals error motion components which cannot be measured using the existing methods.

1.1. Axis of rotation error motion

As the axis of rotation rotates around an axis, any motion in other five degrees of freedom is considered as error motion. Interaction between excitation forces coming from internal or external sources with the mass, damping and elasticity of the axis and its supporting structure causes the error motion [2].

As defined in the current standards [2] and [3], there are three primary categories of error motion: tilt motion (Figure 1.1(a)), pure radial motion (Figure 1.1(b)), and axial motion (Figure 1.1(c)). Furthermore, there are two secondary error motions which are radial and face error motions. Radial error motion is a combination of tilt and pure radial motion at a particular axial position. Face error motion is a combination of axial and tilt error motion at a specified radius of the spindle face.

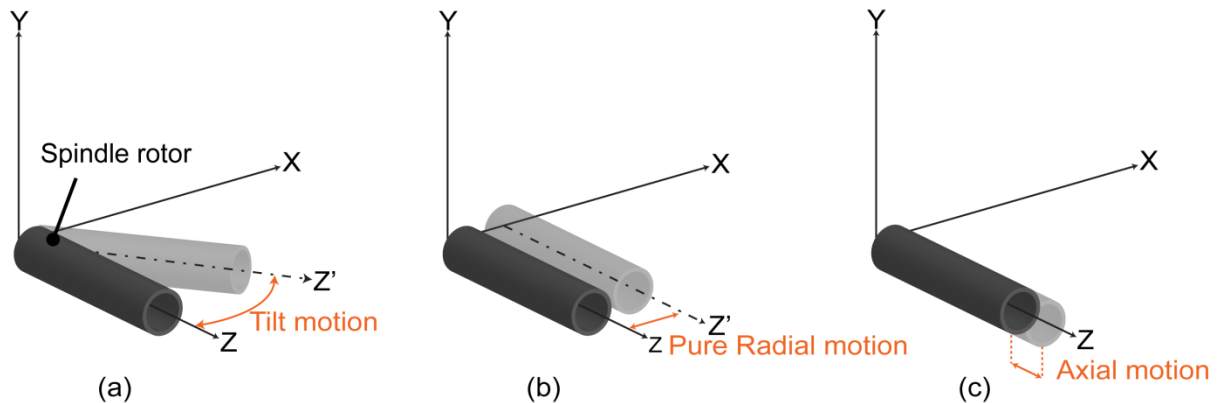


Figure 1.1. Types of axis of rotation error motion.

In ANSI standard [2], the term error motion is referred to relative displacement between the spindle and the tool or gage head only in the sensitive direction. As defined by standard, “sensitive direction is perpendicular to the ideal generated work piece surface through the instantaneous point of machining or gaging”. In machining applications with a single sensitive direction, such as boring and turning, any motion perpendicular to the sensitive direction has a second order effect. Therefore, standard methods neglect these motions when characterizing spindle performance. But these methods are not sufficient for applications with two simultaneous radial sensitive directions, such as axis-asymmetric and/or multiple-tool machining. In contrast, this research introduces a new 2D method which characterizes spindle based on error motion in any radial direction.

1.2. Prior art in measuring axes of rotation

1.2.1. The current ISO and ASME/ANSI standards

Spindle motion in the sensitive direction is defined as the “component of the axis motion that moves toward or away from a cutting tool or gage head” [2]. Over the years, researchers focused

on specifying spindle performance for applications where the spindle has a single sensitive direction. To this end, methods for measuring axes of rotation radial error motion have been divided in two categories: rotating sensitive direction method and fixed sensitive direction method.

Thusty [4] realized the need to generate a base circle for better visualizing the motion of axis of rotation. Using two mutually perpendicular gage heads as shown in Figure 1.2, the motion of the test sphere was measured and the resulting runout was displayed on the oscilloscope X-Y plot. To generate the base circle, Thusty installed the test sphere slightly eccentric with respect to the rotation axis. This eccentricity generates once-per-revolution sinusoidal signals superimposed on the probe signals.

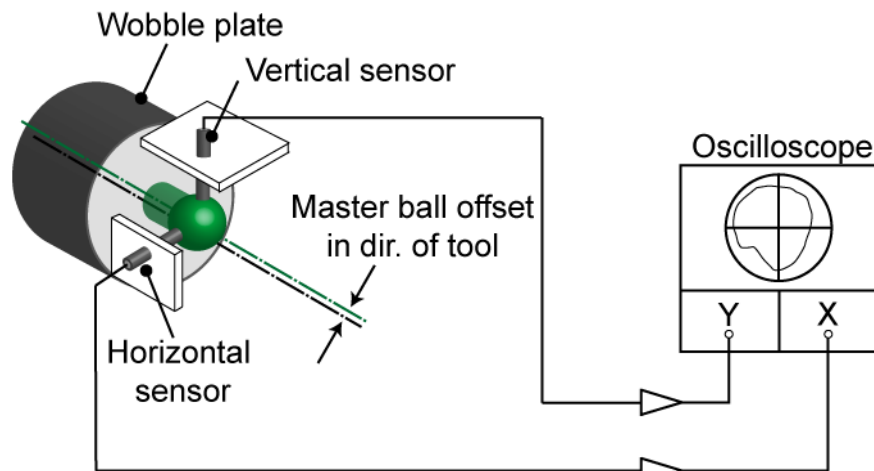


Figure 1.2. Thusty's rotating sensitive direction method setup. Redrawn from [3].

As an example, Figure 1.3(a) shows a numerical example of the motion captured by the vertical and horizontal sensors. Figure 1.3(b) shows the resulting polar plot displayed on the oscilloscope.

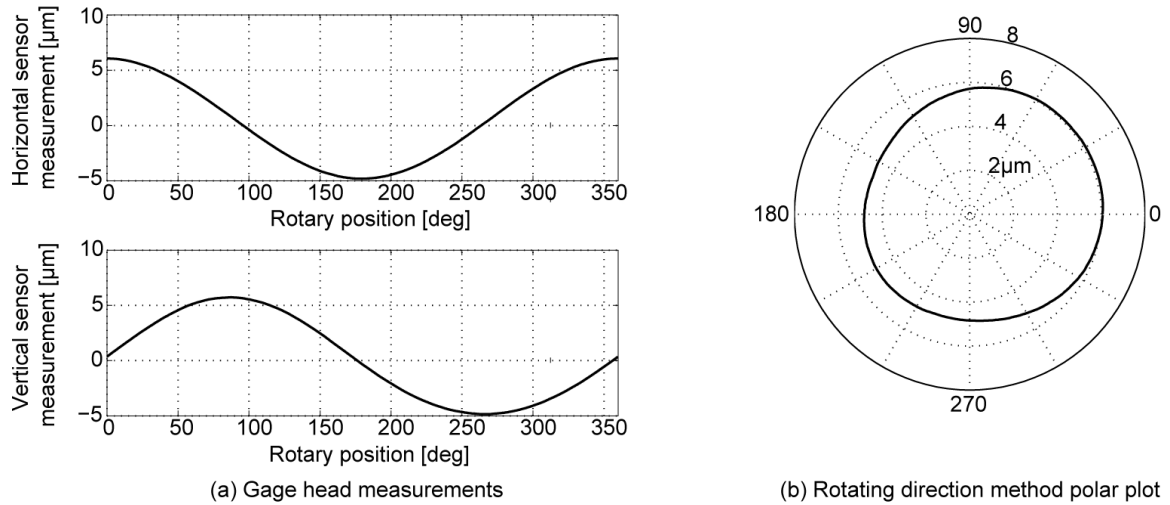


Figure 1.3. Numerical example illustration of Tlustý's rotating sensitive direction method.

The deviation of the polar plot shown in Figure 1.3(b) from a perfect circle gives the radial error motion of the spindle. Tlustý's method is referred as rotating sensitive direction method since it can only capture error motions in the direction of the eccentricity of the ball. This method is insensitive to spindle motions which are tangential to test sphere eccentricity. In applications where the tool is fixed, such as outside cylinder surface turning, these tangential motions have a direct effect on the finished part when they are in the sensitive direction. For these applications, Bryan [5] introduced a new method referred as fixed sensitive direction method. This method measures the spindle motion moving toward or away from a fixed tool. Figure 1.4 shows Bryan's setup which generates radial error motion polar plot on the oscilloscope.

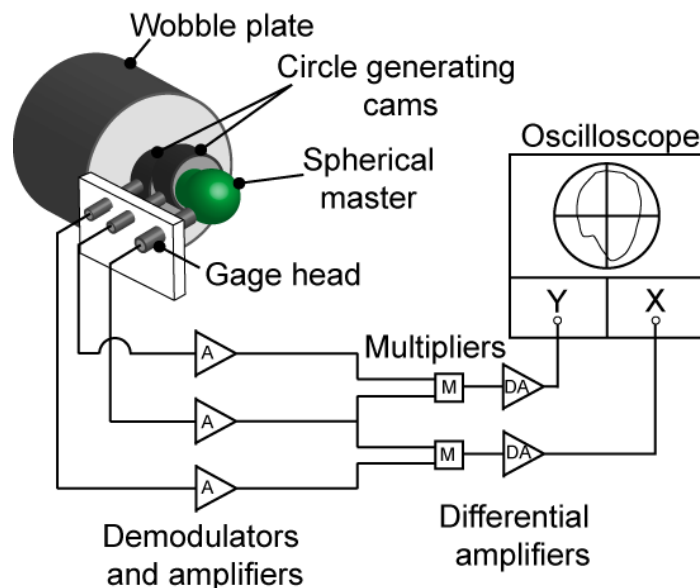


Figure 1.4. Bryan's fixed sensitive direction method. Redrawn from [5].

To generate the base circle for the polar plot, Bryan used two cylinders which were equally eccentric with respect to the rotation axis but had 90 degree phase shift. Two low-magnification gage heads measured the runout of the cylinders. A single high-magnification gage head was used to measure the runout of the spherical master which is centered as close as possible. The two signals coming from the circle generating gage heads were electrically multiplied by the signal measuring the spherical master runout and fed into the oscilloscope. Figure 1.5(b) shows an example of the polar plot for the example data of Figure 1.5(a). The deviation of the polar plot shown in Figure 1.5(b) from a perfect circle gives the radial error motion of the spindle in the direction of the gage installation.

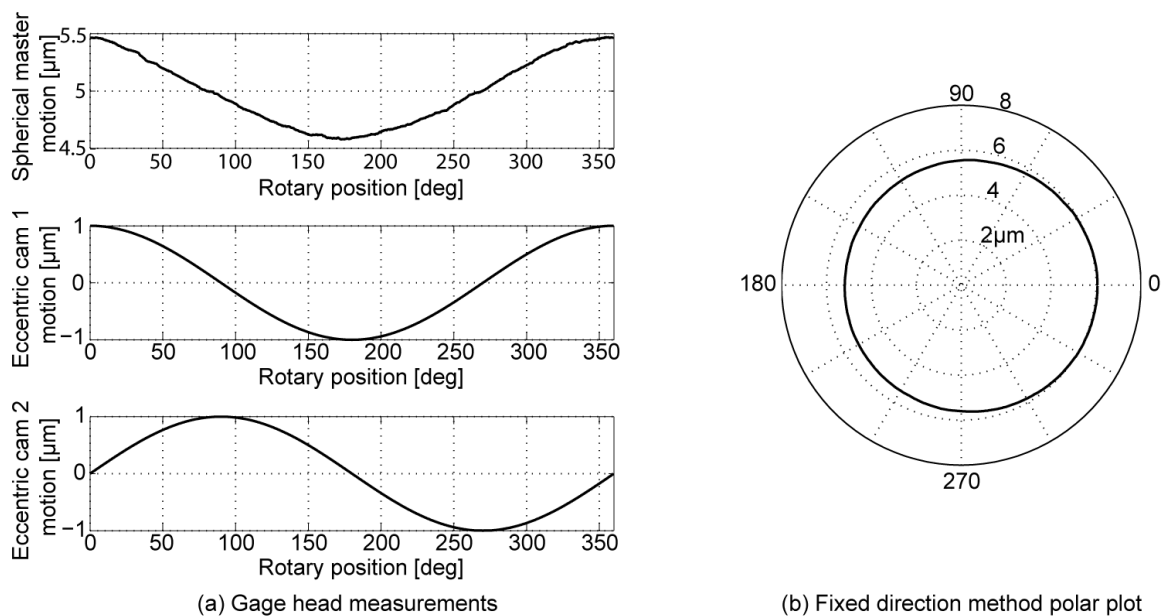


Figure 1.5. Numerical example illustration of Bryan's fixed sensitive direction.

In 1973, Vanherck and Peters [6] presented a setup which used encoder for measuring rotary position instead of eccentric cams. In addition, the new setup used computer to capture and display the data instead of oscilloscope. This setup is shown in Figure 1.6.

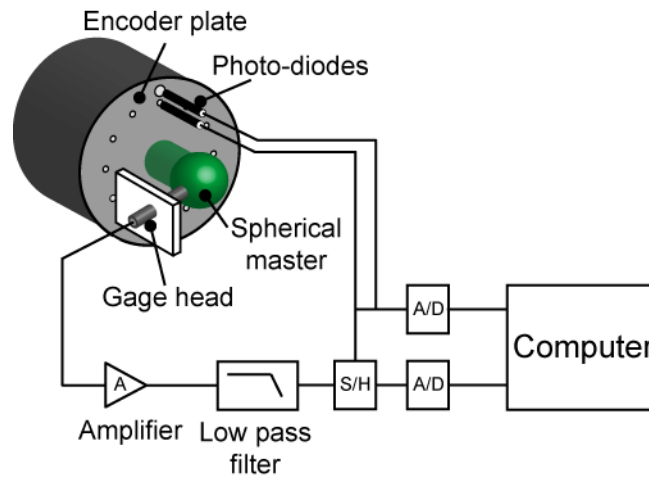


Figure 1.6. Vanherck and Peters digital measurement setup. Redrawn from [6].

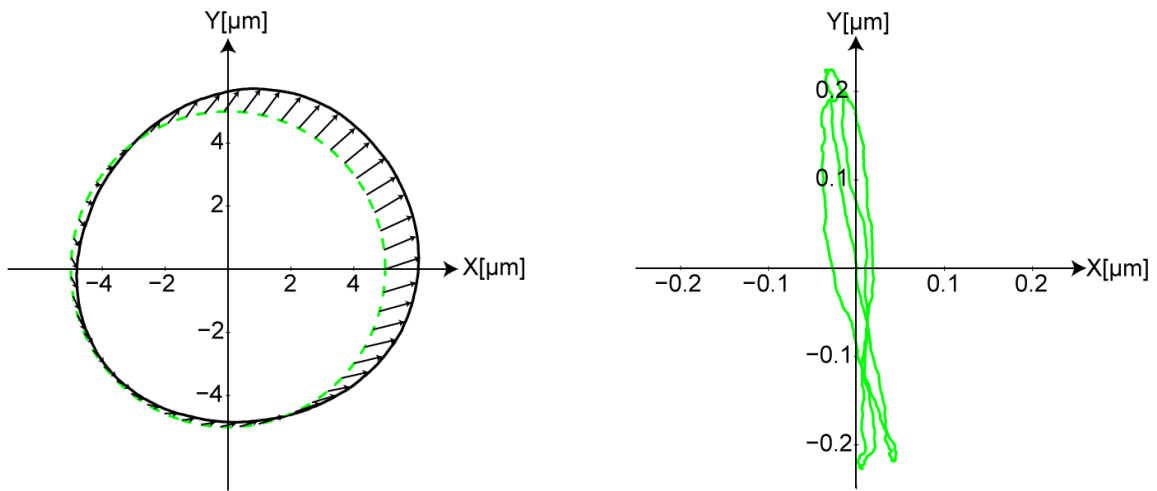
In addition, Vanherck and Peters introduced digital processing such as Fourier transform into spindle metrology. The transformation of data from time domain into frequency domain is a convenient way to distinguish between synchronous and asynchronous error motions. As defined in [3], synchronous error motion is the portion of the total error motion that occurs at integer multiples of the rotation frequency. The polar plot of synchronous motion is indicative of roundness errors of the work piece under ideal cutting conditions. Asynchronous error motion consists of motion components that are random or have frequencies other than spindle rotational frequency and its integer multiples. The polar plot of asynchronous error motion presents the surface roughness under ideal cutting conditions. The mathematical derivation of synchronous and asynchronous error motions using both Frequency and time domain is given in Appendix A.

Artifact roundness is another important issue for axis-of-rotation metrology, and several methods have been developed to remove ball roundness from radial indicator measurement, including reversal methods [7, 8], multiple-step method [9], and multiple-point methods (also known as multiple-probe method) [10, 11, 12]. As an alternative to test balls, another aerostatic bearing spindle can be used as a probe target in master axis method to measure the axis of rotation under test [13]. Bryan summarized the major milestones in the history of rotation axis research [14]. All these works helped establish the foundation of the current standards for geometric accuracy of rotation axes [2, 3]. The codes presented by the standards are widely accepted and are the common language used for technical communication regarding the subject. A recent book by Marsh documented and illustrated these existing methods with many practical details and experimental examples [15].

1.2.2. Radial error motion in two dimensions

Any motion of the axis of rotation in X-Y plane at a particular axial location is radial error motion. Therefore, to find the actual spindle radial trajectory, a two dimensional point of view is required. Tlusty's rotating sensitive direction polar plot was the first attempt to visualize the motion of axis of rotation in X-Y plane. This plot is redrawn in Figure 1.7(a) as a set of spindle error motion vectors: the origin of each vector is a point on the base circle corresponding to the rotary angle of the axis. The vectors include both the radial motion of the axis and the eccentricity of the target at a particular rotary position.

Naguchi *et al.* published one of the earliest papers to investigate spindle radial error motion in two dimensions. In his method, the spindle error motion vectors are obtained after removing the ball eccentricity from the X and Y probe measurements [16]. The plot of these vectors gave the motion path of the axis of rotation in X-Y plane (Figure 1.7(b)). Naguchi's method removes ball eccentricity by applying least squares fitting method to X and Y measurements together.



(a) Tlusty's rotating sensitive polar plot (b) Naguchi's vector indication plot
Figure 1.7. Numerical example illustration of existing methods to specify radial error motion in two dimensions.

1.3. Existing methods for specifying axis of rotation error motion

According to the current standards, the polar plots themselves are not radial error motion, but the error motion values can be extracted from them by removing the centering error. There are two methods proposed in the standard to eliminate the centering error.

Figure 1.8 shows the existing methods applied to a polar plot. The polar plot is the one obtained in Bryan's fixed sensitive direction in the previous section but same conclusion can be obtained with any polar plot. In the least squares fitting method shown in Figure 1.8(left), the least squares circle of the polar plot is found and the deviation of the polar plot from this circle is specified as radial error motion. This process removes the DC (the radius of the least squares fitting circle) and fundamental component (the offset from the polar chart center to the least squares circle center) from the polar plot data. In the frequency domain method shown in Figure 1.8(right) the polar plot data (N points per revolution) is first transferred to frequency domain. Next, the DC (0 cpr) and fundamental component (both 1 cpr and -1 cpr) is removed from the spectrum [6]. The data is then transferred back to angle domain by inverse Fourier transform.

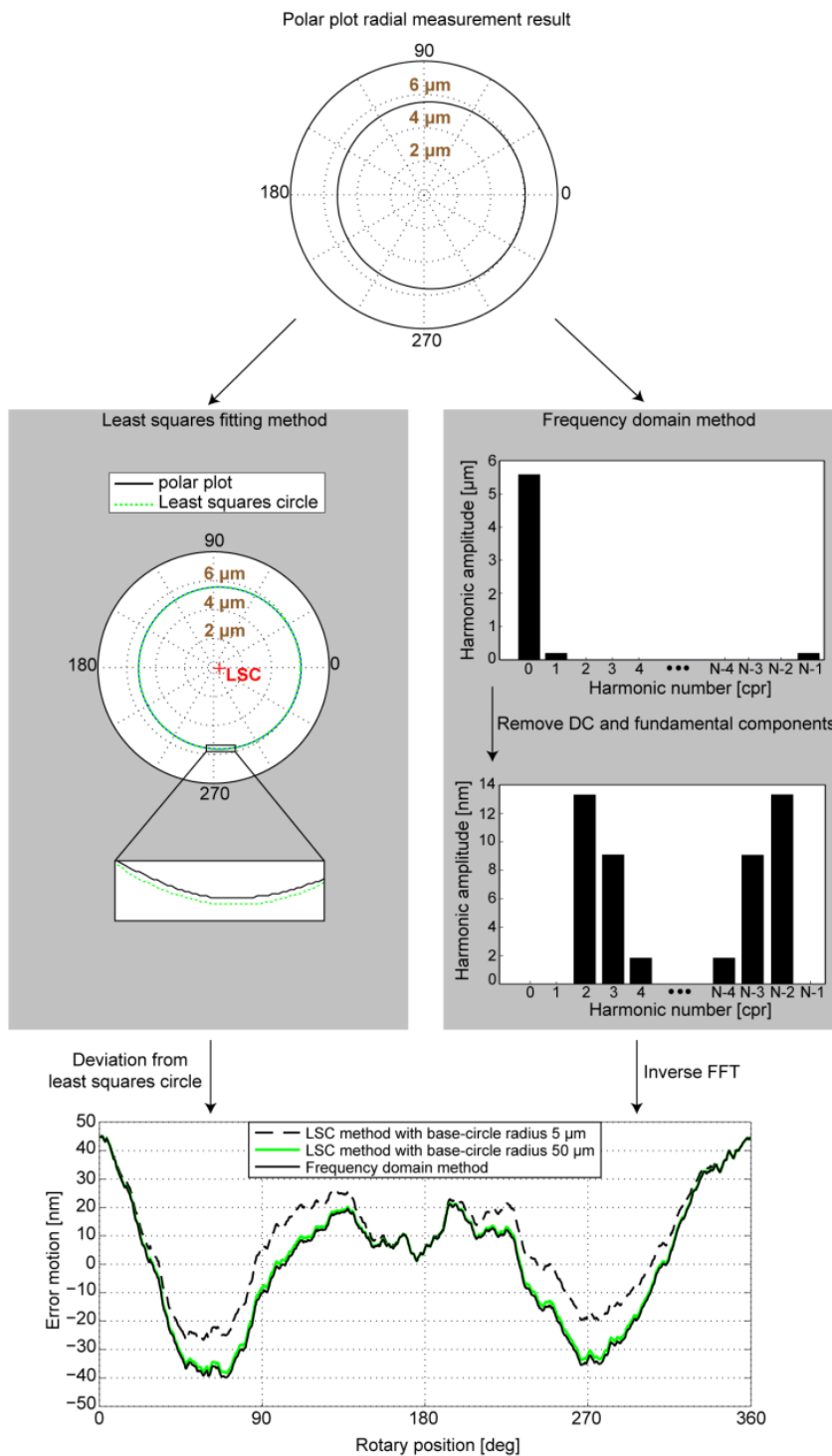


Figure 1.8. Numerical example illustration of two existing methods of specifying radial error motion from polar plots.

These two methods are essentially equivalent. Least squares fitting was very convenient for presenting the results graphically at the time when digital processing was not readily available. However, it suffers from a second-order distortion effect which is dependent on the polar plot

base-circle radius, as discussed in [2]. To show this effect, the radial error motion is plotted in Figure 1.8(bottom) for a radius of $r_0 = 5 \mu\text{m}$ and $r_0 = 50 \mu\text{m}$. When the polar plot base circle radius is big enough, the error motion extracted from polar plot least squares fitting will be the same as that from the frequency domain method. In comparison, the frequency domain method can consistently give results independent of base-circle radius, r_0 . Appendix B shows why these two methods converge as the base-circle radius increases.

1.4. Current standard methods vs. 2D method

In current standards [2, 3] “error motion is used to refer to relative displacement in the sensitive direction between the tool or gage head and the workpiece”. As a result, the major tool for specifying the spindle performance has been polar plots. The problem is that polar plots do not represent the actual error motion of axes of rotation. They only indicate the consequence of spindle error motion in the specified application. On the other hand, the new 2D method gives the actual radial error motion of the spindle regardless of whether the spindle is used to make something or how the spindle is used in a particular application. In addition, 2D analysis reveals the fundamental error motion of the spindle which cannot be identified with the existing methods. This fundamental component has a significant effect in application with two radial sensitive directions. In summary the new 2D method:

1. Distinguishes between radial error motion and its consequence. It gives enough information to visualize the actual radial error motion regardless of spindle application.
2. Captures all the components of the error motion including the fundamental error motion which is considered to be nonexistent in the current standards.
3. Gives the consequence of spindle error motion for all types of applications including the ones which are sensitive to radial error motion in two directions.

In the following subsections, a detailed description of the above points is given.

1.4.1. Radial error motion and its consequence

When a spindle is used in a surface cutting machine, the consequence of spindle radial error motion refers to the produced part surface/shape distortion that is caused by the spindle radial

error motion. When a spindle is used in a rotary CMM, the consequence of spindle radial error motion refers to the measurement data error that is caused by spindle radial error motion. Therefore, axis of rotation error motion and its consequence in a particular spindle application are two related but distinct concepts. Error motion consequence is certainly caused by error motion, but consequence also depends on the application details, such as how the cutting tools are installed, how many tools are installed, what type of parts to be made, and so on. Whenever the axis of rotation error motion consequence is discussed, the full details of the spindle application should be clearly specified. Current standards have adopted this approach and proposed two distinct methods for testing axes of rotation: one for applications with a fixed sensitive direction, and one for applications with a rotating sensitive direction. Each method gives a polar plot which indicates the consequence of spindle error motion in the corresponding category of applications. The specified performance of a spindle will differ based on the method used for testing it (rotating or fixed). This has been illustrated in A15 of [2], by Donaldson. He has given a case where the fixed sensitive direction method gives an elliptical pattern (2-lobe shape) polar plot while the rotating sensitive direction method gives a perfect circular shape polar plot. As a result, the spindle has a twice per revolution error motion when tested with fixed sensitive direction method but it has no error motion when tested with rotating sensitive direction method.

In reality, any motion deviation of the axis of rotation from a fixed line in space is error motion. This error motion cannot be fully captured using the current standard methods. This thesis introduces a new 2D method for testing axes of rotation in which spindle's behavior is characterized regardless of the spindle application. Instead of polar plot, the 2D method gives enough information to visualize the error motion of axis of rotation in two dimensions. This new approach distinguishes between spindle error motion and consequence of spindle error motion in a particular application.

1.4.2. Fundamental radial error motion

In the fixed sensitive direction method, spindle error motion is obtained by eliminating the centering error in the polar plot. As discussed in section 1.3., this is done by removing the fundamental component of the polar plot data. However, no reason has been given to support the assumption that fundamental (one cycle-per-revolution or 1 cpr) radial error motion cannot physically exist in the fixed sensitive direction. Current belief is that the motion component

removed is generated only by the eccentricity of the target ball. Similarly, in Tlustý's rotating sensitive direction method, the fundamental component of the polar plot data is removed but no reason has been given to support that spindle cannot have a fundamental error motion in the rotating direction. Therefore, the routine practice of eliminating a 1-cpr component from radial motion measurement is questionable. By proper and careful installation of the test artifact, the 1 cpr component in one probe measurement (X or Y) can be completely eliminated, but the 1 cpr in the other probe measurement does not necessarily vanish. The results of the new 2D analysis shows that 1 cpr radial error motion not only exists but it can also have a magnitude higher than any other error motion component.

1.4.3. Applications with two radial sensitive directions

Today, spindles are not restricted to generating axis-symmetric patterns. Some processes, such as FTS-assisted turning, machining of non-round holes, and rotary beam writing, are simultaneously sensitive to radial error motion in two dimensions. As a result, the fundamental spindle error motion of spindles has a significant effect on the finished pattern. The current standard methods which remove any first order harmonic from the measurements are not sufficient to characterize spindles for these types of applications. The new 2D analysis on the other hand can be used to specify the spindle error motion for any type of application.

1.5. Thesis overview

This thesis introduces a new 2D method for testing the radial error motion of axis of rotation. Chapter 2 introduces the theory behind the new 2D method and uses an analytical example to illustrate the concepts. The spindle error motion as well as the consequence of this error motion in different types of applications are derived and compared with the current standard method analysis.

Chapter 3 presents the results of 2D analysis on two types of spindles: ball bearing spindle on a Mori Seiki 5-axis machining center and 10 R Block-Head aerostatic bearing spindle from Professional Instruments. These experiments prove that fundamental spindle error motion exists and its magnitude is higher than any other error motion component. In addition, experimental results are used to derive the potential out-of-roundness of the work piece in different types of applications.

Chapter 4 discusses the possible causes of fundamental error motion. Dynamic stiffness test results on the ball bearing spindle and unbalance test results on the aerostatic spindle will be used to backup the discussion. Additional tests will be presented to illustrate effect of temperature and pressure on spindle error motion measurements.

Chapter 5 concludes this thesis and points out some areas for future work on testing axes of rotation.

Chapter 2. Two-dimensional radial motion theory

Figure 2.1 shows a widely-used spindle metrology setup: two radial displacement measurement indicators are orthogonally installed to read against the rotor-mounted test ball's surface. The subtlety of spindle metrology is that the two radial indicators plus a rotary encoder capture not only spindle radial error motion, but also two undesired components: the ball installation eccentricity and the test ball roundness. The artifact roundness is composed of harmonic components of 2 and higher cycles per revolution (cpr), and the installation eccentricity brings a 1-cpr component to the indicator measurements. The major task of spindle metrology is to precisely strip off these undesired components and present the true radial error motion.

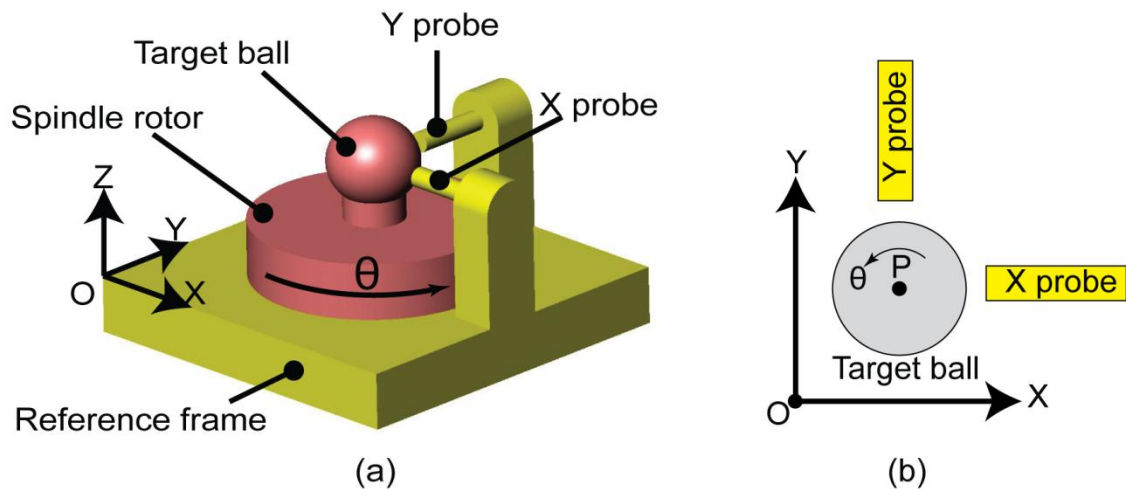


Figure 2.1. Typical metrology setup: (a) 3D model. (b) 2D cross-sectional view at the specified axial location.

This chapter introduces the new 2D method for testing the radial error motion of axes of rotation. By using complex Fourier analysis, this method is able to identify all the components of radial error motion and give a complete description of the axis trajectory in space. Figure 2.2 presents the framework of this novel 2D method.

The metrology reference frame and the concept of structural loop are discussed in section 2.1. Section 2.2 analyzes the radial motion of a particular test point on the spindle rotor, with respect to the specified metrology reference frame. Based on the result of the test point motion analysis, the axis of rotation radial error motion is determined in Section 2.3. Section 2.4

identifies the consequence of spindle radial error motion in spindle applications. In Section 2.5, the 2D method and the current standard methods are compared and discussed.

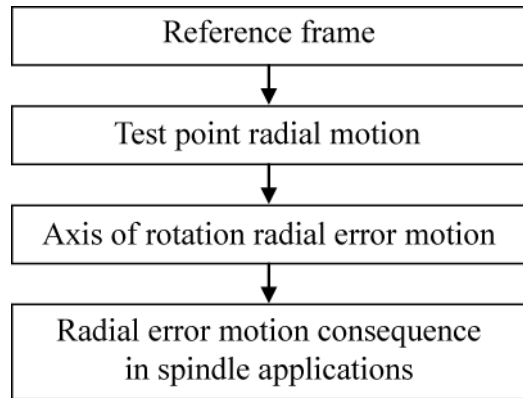


Figure 2.2. Spindle radial error motion analysis sequences.

2.1. Metrology reference frame

In general, motion is the movement of one object relative to another reference body. When discussing motion, a rigid body should be assigned explicitly as a reference frame, with respect to which motion can be described without ambiguity. Axis of rotation error motion is not an exception.

Different reference frame selections will result in different motion measurements. For example, in a five-axis machining center, it will be more meaningful to measure the tool spindle error motion relative to the work-holding table than to the spindle stator; therefore the work-holding table is chosen as the reference frame, and the error motion induced by the machine structural loop is included as part of the measurement. Spindle suppliers usually select the spindle housing or stator as the reference frame to demonstrate spindles' best possible performance, with a structural loop as short as possible. The selection of metrology reference frame is governed by the objective of axis-of-rotation motion analysis. Different choice of metrology reference frame reveals different information, which can serve different purposes. Generally, a rigid body with a minimum varying radial force load is preferred, but there is not a single best choice for reference frame. When presenting an axis-of-rotation error motion result, the chosen reference frame should be clearly stated so that the analysis result can be properly interpreted.

Once the metrology reference frame is determined, the gauge indicators, such as capacitance probes, should be rigidly installed in this reference frame to measure the relative motion between the rotor-installed test artifact (a ball or a cylinder) and the metrology reference frame. In a typical setup as shown in Figure 2.1, the reference frame is the rigid body on which the X and Y motion-measurement probes are installed. The reference directions of the two radial dimensions X and Y, as well as the rotary position θ , are set by the right-hand rule.

The metrology frame origin location can be set arbitrarily without any effect on the analysis result. In measurement, the origin location is determined by factors such as the probe installation, probe zero-biasing adjustment, and other possible offset values added by data acquisition and analysis software. For the purpose of spindle metrology, it is not necessary to know the exact location of the reference frame origin. When investigating the axis average line shift under various conditions, such as different loads and speeds, the reference origin location should remain unchanged.

2.2. Test point radial motion

Once defining the reference frame, the radial indicator measurements give the test artifact center point motion in two orthogonal radial directions. Specifically, in the test setup shown in Figure 2.1, the test ball has a geometric center P, which is the least squares center of the ball profile in the cross-sectional plane where the two indicators are installed [17]. Each indicator measurement includes both the radial motion of the point P and the ball's out-of-roundness. The out-of-roundness component can be removed from each indicator measurement using one of the methods presented in [7, 8, 9, 10, 11 or 12]. Consequently, the motion of a single point P on the spindle rotor is fully extracted. In this sense, the goal of installing a test artifact (ball or cylinder) on the rotor under test is to make the motion of one particular point on the rotor accessible to the radial measurement indicators.

After removing the test ball out-of-roundness from the measurement data, the test ball's center 2D radial motion in the X-Y plane can be represented by a rotation-dependent complex variable:

$$v_p(\theta) = x_p(\theta) + jy_p(\theta) \quad (2-1)$$

where $x_p(\theta)$ and $y_p(\theta)$ are the point P motion in the X and Y directions respectively, as shown in Figure 2.1(b).

In order to illustrate the theoretical formulation on experimental data, Figure 2.3 shows a numerical example that will be used throughout this paper: $x_p(\theta)$ and $y_p(\theta)$ are test ball center motions over four consecutive revolutions.

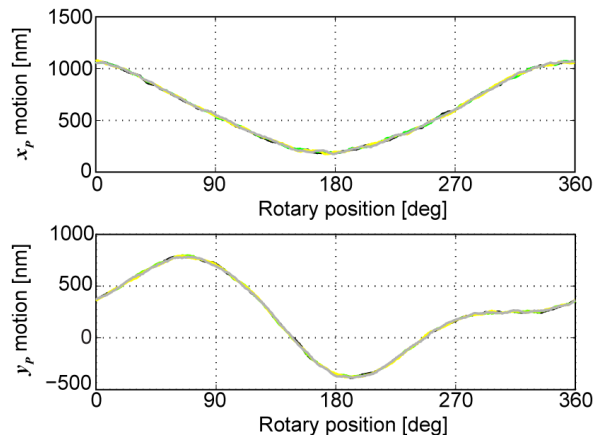


Figure 2.3. A numerical example of the X and Y components of the test ball 2D motion. Data over four revolutions are overlaid together.

In a procedure similar to current standards [2, 3], the test point's 2D motion $v_p(\theta)$ can be decomposed into synchronous motion and asynchronous motion. The synchronous motion $\bar{v}_p(\theta)$ is the synchronized average of $v_p(\theta)$ over M (an integer number) revolutions:

$$\begin{aligned}\bar{v}_p(\theta) &= \frac{1}{M} \sum_{i=1}^M v_p(\theta + 2\pi i) = \bar{x}_p(\theta) + j\bar{y}_p(\theta) \\ \bar{x}_p(\theta) &= \frac{1}{M} \sum_{i=1}^M x_p(\theta + 2\pi i) \\ \bar{y}_p(\theta) &= \frac{1}{M} \sum_{i=1}^M y_p(\theta + 2\pi i)\end{aligned}\tag{2-2}$$

where $\bar{x}_p(\theta)$ and $\bar{y}_p(\theta)$ are the synchronous motion of the test ball's center P in the X and Y directions, respectively.

The asynchronous motion $\tilde{v}_p(\theta)$ is the difference between $v_p(\theta)$ and $\bar{v}_p(\theta)$:

$$\begin{aligned}\tilde{v}_p(\theta) &= v_p(\theta) - \bar{v}_p(\theta) = \tilde{x}_p(\theta) + j\tilde{y}_p(\theta) \\ \tilde{x}_p(\theta) &= x_p(\theta) - \bar{x}_p(\theta) \\ \tilde{y}_p(\theta) &= y_p(\theta) - \bar{y}_p(\theta)\end{aligned}\tag{2-3}$$

where $\tilde{x}_p(\theta)$ and $\tilde{y}_p(\theta)$ are the asynchronous motion of the test ball's center P in X and Y directions, respectively. The asynchronous motion components do not repeat at integer cycles per revolution: some of them are random and some of them may repeat at non-integer cycle per revolution, such as the half-speed whirling motion found in hydrodynamic-bearing spindles. The

target ball synchronous and asynchronous motion calculation results are shown in Figure 2.4 for the example data in Figure 2.3.

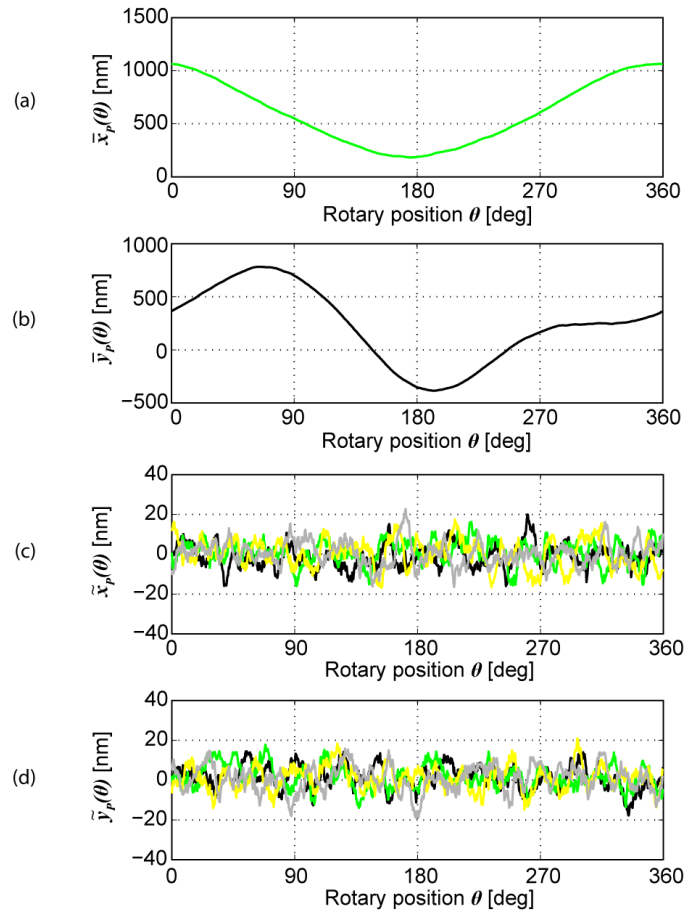


Figure 2.4. Test ball's synchronous and asynchronous motion of the numerical example: (a) Synchronous radial motion in X. (b) Synchronous radial motion in Y. (c) Asynchronous radial motion in X. (d) Asynchronous radial motion in Y.

By using Fourier analysis, the periodic function $\bar{v}_p(\theta)$ can be represented as the sum of vectors rotating at various harmonic rotation frequencies in both the positive and negative directions:

$$\bar{v}_p(\theta) = \sum_{k=-\infty}^{\infty} \bar{V}_p(k) e^{jk\theta} \quad (2-4)$$

where k is an arbitrary integer number and $\bar{V}_p(k)$ is $\bar{v}_p(\theta)$'s k -th Fourier coefficient, as given by:

$$\bar{V}_p(k) = \frac{1}{2\pi} \int_0^{2\pi} \bar{v}_p(\theta) e^{-jk\theta} d\theta \quad (2-5)$$

It should be noted that the Fourier coefficients of a real-valued function such as $\bar{x}_p(\theta)$ are always in complex conjugate pairs with redundant information at k and $-k$ cpr. However, the

complex-valued function $\bar{v}_p(\theta)$'s Fourier coefficients $\bar{V}_p(k)$ and $\bar{V}_p(-k)$ are generally independent from each other, representing two vectors rotating k times faster than the speed of the axis of rotation but in opposite directions. Figure 2.5 illustrates this concept for the case where measurements $x(\theta)$ and $y(\theta)$ have only generated $k = 1$ harmonic component. Note that the trajectory of the measured point is a full circle in X-Y plane.

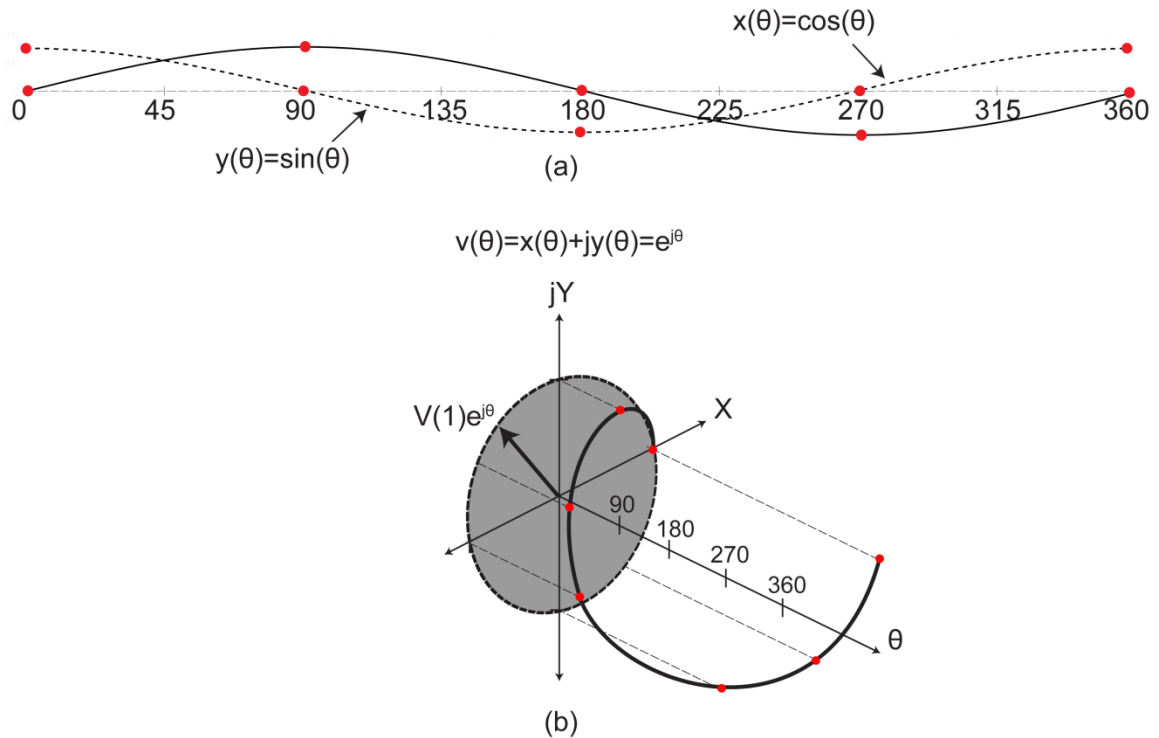


Figure 2.5. Physical meaning of $V(1)$ Fourier coefficient

Figure 2.6 shows the amplitude and phase of the first 20 Fourier coefficients $\bar{V}_p(k)$ for the numerical example.

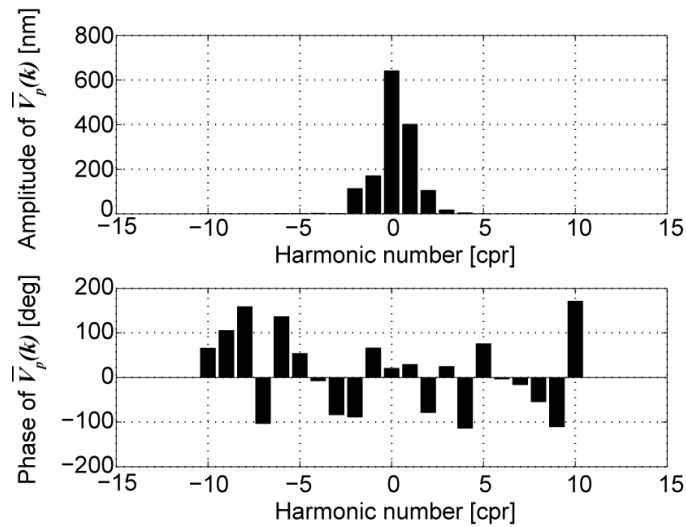


Figure 2.6. Fourier coefficients of the test ball's synchronous motion for the numerical example.

Based on Eq. (2-4), Figure 2.7 illustrates the test ball's 2D synchronous motion represented by the sum of the rotating vectors. When each vector rotates with the direction and speed indicated, the point P will travel along the dashed trajectory.

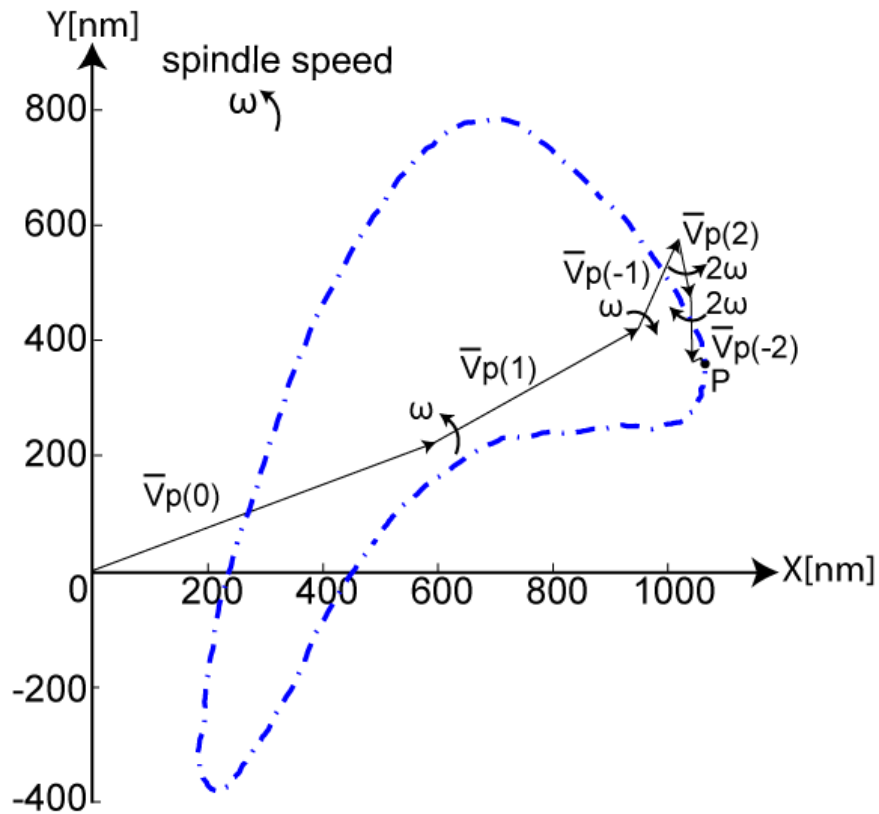


Figure 2.7. Vector representation of point P's synchronous radial motion for the numerical example.

2.3. Axis of rotation radial error motion

In this section, the concept of axis of rotation is first discussed. Then, by relating the test ball center P's radial motion to the axis of rotation, the location of this axis as well as its error motion are analytically derived.

2.3.1. Concept of axis of rotation

There are two key concepts introduced in [2, 3] to specify spindle error motion: axis of rotation and axis average line. Axis of rotation is a straight line about which the rotor rotates. Axis average line is the spatial average position of the axis of rotation in the reference frame. Therefore, at a specified test condition, the axis of rotation is a line fixed on the spindle rotor and the axis average line is a line fixed to the reference frame. As shown in Figure 2.8, the spindle rotor (in gray) rotates about the axis of rotation. The axis of rotation itself moves relative to the stationary axis average line, and this relative motion is referred as the spindle error motion. As long as the spindle rotor spins, the axis of rotation error motion can be determined, and therefore, does not rely on how the spindle is used in a particular application.

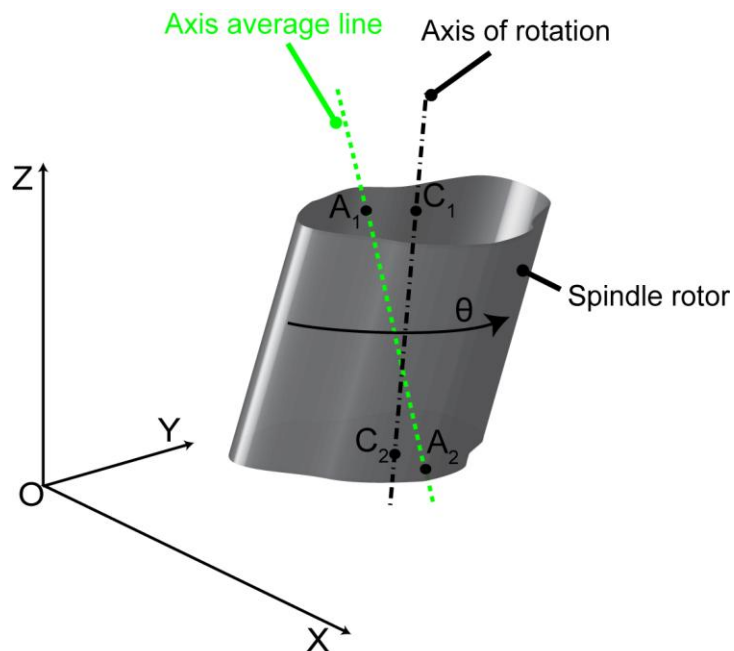


Figure 2.8. The concepts of axis of rotation and axis average line.

At a specified axial location, such as the rotor's top surface as shown in Figure 2.8, the spindle rotor is represented by its cross-section; the axis of rotation is represented by the rotation center C_1 ; the axis average line is represented by the average point A_1 . Accordingly, the 2D picture is as follows: the rotation center C_1 is a point of the rotor cross-section, and this rotor cross-section rotates around C_1 ; the rotation center C_1 itself moves around a stationary point A_1 . The 2D radial error motion is the motion vector pointing from the average point A_1 to the rotation center C_1 . From the rotation centers at two axial locations such as C_1 and C_2 , the tilt error motion can be fully specified.

It should be noted that the rotation center here is different from the instantaneous center, which is a totally different concept and is not used in spindle error motion definition.

2.3.2. Perfect spindle

On a perfect spindle, the axis of rotation and axis average line are the same. As shown in Figure 2.9, at a specified axial location, the rotation center C is a stationary point in the XOY plane and coincides with the average point A . When a test ball is installed, the ball's center P will revolve around C , or the vector from C to P rotates with the rotor. If the spindle speed is n [rpm], then the vector from C to P rotates at n [rpm], in the same direction as the spindle rotation. For this simple case, the motion vector of P will contain only a DC component and $k = +1$ component:

$$v_p(\theta) = \bar{V}_p(0) + \bar{V}_p(1)e^{j\theta} \quad (2-6)$$

Obviously, $\bar{V}_p(1)$ represents the eccentricity of the test ball's center P to the rotation center C .

The eccentricity can only bring in $k = +1$ component $\bar{V}_p(1)$ to the test ball's radial motion. The DC component $\bar{V}_p(0)$ is the position of the axis average line in the metrology frame.

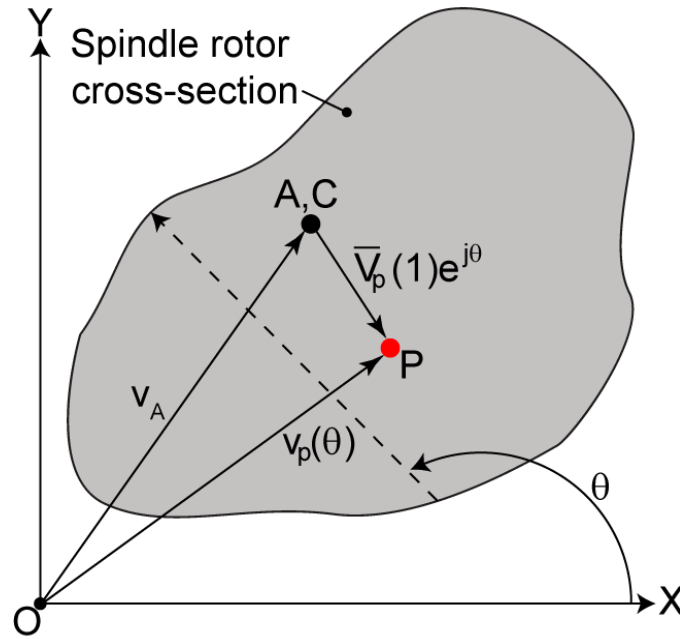


Figure 2.9. Relation between the average point A, the rotation center C, and the test ball center P on a perfect spindle. The dashed arrow line indicates the rotary position of the spindle rotor. Points A and C coincide. The distance between C and P is the eccentricity of the test ball installation.

2.3.3. Axis of rotation radial error motion

For a general spindle, under a specified test condition and at a specified axial location, Figure 2.10 shows the relation among P (the test ball's center), C (the rotation center), and A (the average point). P and C are two points on the rotor, and A is a stationary point in the XOY plane. The vector from C to P has constant length and rotates at exactly the same speed and direction as the spindle rotation. Same as the perfect spindle, the eccentricity from C to P will bring the $k = +1$ component $\bar{V}_p(1)e^{j\theta}$ to the radial motion of P. Removing the $k = +1$ component $\bar{V}_p(1)e^{j\theta}$ from the test ball center P's radial motion gives the motion of rotation center C:

$$v_C(\theta) = v_P(\theta) - \bar{V}_p(1)e^{j\theta} \quad (2-7)$$

Further, the synchronous and asynchronous motion of the rotation center C is

$$\bar{v}_C(\theta) = \sum_{\substack{k=-\infty \\ k \neq 1}}^{\infty} \bar{V}_p(k)e^{jk\theta} \quad (2-8)$$

and

$$\tilde{v}_C(\theta) = \tilde{v}_P(\theta) \quad (2-9)$$

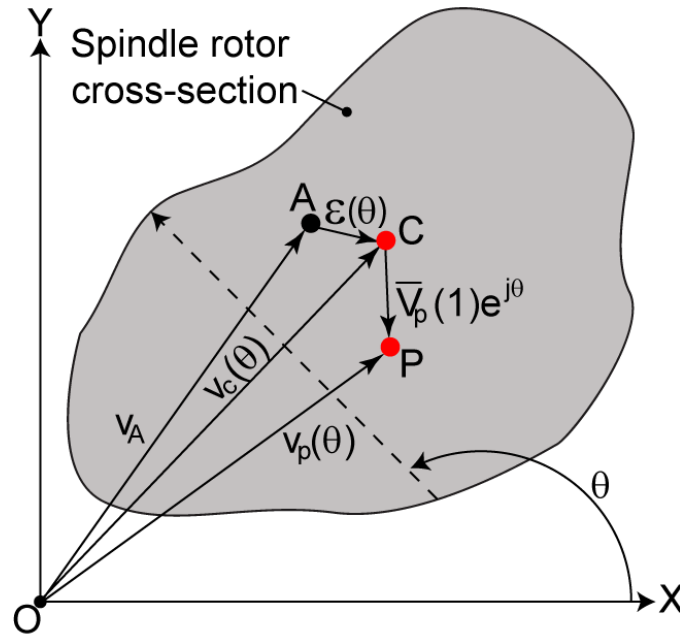


Figure 2.10. Relation between the average point A, the rotation center C, and the test ball center P on a spindle with radial error motion. The dashed arrow line indicates the rotary position of the spindle rotor. The vector $\varepsilon(\theta)$ from A to C is the spindle radial error motion at the current angular position. The distance between C and P is the eccentricity of the test ball installation.

By taking the average of the spindle rotation center C over M revolutions, the average location of the spindle rotation center C can be found as follows:

$$\begin{aligned}
 v_A &= \frac{1}{2M\pi} \int_0^{2M\pi} v_C(\theta) d\theta \\
 &= \frac{1}{2M\pi} \int_0^{2M\pi} (\bar{v}_C(\theta) + \tilde{v}_C(\theta)) d\theta \\
 &= \frac{1}{2M\pi} \int_0^{2M\pi} \bar{V}_P(0) d\theta + \frac{1}{2M\pi} \int_0^{2M\pi} \sum_{\substack{k=-\infty \\ k \neq 0,1}}^{\infty} \bar{V}_P(k) e^{jk\theta} d\theta + \frac{1}{2M\pi} \int_0^{2M\pi} \tilde{v}_C(\theta) d\theta \\
 &= \bar{V}_P(0)
 \end{aligned} \tag{2-10}$$

as the asynchronous motion and non-zero frequency synchronous motion component of C have zero mean value over the recorded M revolutions.

The radial error motion $\varepsilon(\theta)$ is the vector from A to C:

$$\begin{aligned}
 \varepsilon(\theta) &= v_C(\theta) - v_A \\
 &= v_P(\theta) - \bar{V}_P(1)e^{j\theta} - \bar{V}_P(0)
 \end{aligned} \tag{2-11}$$

Further, the synchronous radial error motion can be calculated as

$$\begin{aligned}\bar{\varepsilon}(\theta) &= \bar{v}_C(\theta) - \bar{V}_P(0) \\ &= \sum_{\substack{k=-\infty \\ k \neq 0,1}}^{\infty} \bar{V}_P(k) e^{jk\theta}\end{aligned}\quad (2-12)$$

The synchronous radial error motion in X and Y directions can be calculated by taking the real and imaginary parts of the 2D error motion:

$$\begin{aligned}\bar{\varepsilon}_x(\theta) &= \text{Re}(\bar{\varepsilon}(\theta)) \\ \bar{\varepsilon}_y(\theta) &= \text{Im}(\bar{\varepsilon}(\theta))\end{aligned}\quad (2-13)$$

where $\text{Re}[\cdot]$ and $\text{Im}[\cdot]$ mean taking the real and imaginary part, respectively. The asynchronous radial error motion is

$$\tilde{\varepsilon}(\theta) = \tilde{v}_C(\theta) = \tilde{v}_P(\theta) \quad (2-14)$$

The radial error motion vector $\varepsilon(\theta)$ is a 2D vector function of θ . Here are some ways to quantitatively specify its overall amplitude:

- (a) The Root-Mean-Square (RMS) value of the synchronous radial error motion:

$$\bar{\varepsilon}_{RMS} = \sqrt{\frac{1}{2\pi} \int_0^{2\pi} |\bar{\varepsilon}(\theta)|^2 d\theta} \quad (2-15)$$

According to Parseval's relation [18], the RMS $\bar{\varepsilon}_{RMS}$ can also be calculated from its Fourier coefficients as

$$\bar{\varepsilon}_{RMS} = \sqrt{\sum_{\substack{k=-\infty \\ k \neq 0,1}}^{\infty} |\bar{V}_P(k)|^2} \quad (2-16)$$

- (b) RMS asynchronous error motion:

$$\tilde{\varepsilon}_{RMS} = \sqrt{\frac{1}{2M\pi} \int_0^{2M\pi} |\tilde{\varepsilon}(\theta)|^2 d\theta} \quad (2-17)$$

- (c) RMS total error motion:

$$\varepsilon_{RMS} = \sqrt{\tilde{\varepsilon}_{RMS}^2 + \bar{\varepsilon}_{RMS}^2} \quad (2-18)$$

- (d) maximum synchronous error motion:

$$\bar{\varepsilon}_{MAX} = \max_{0 \leq \theta < 2\pi} |\bar{\varepsilon}(\theta)| \quad (2-19)$$

- (e) maximum asynchronous error motion:

$$\tilde{\varepsilon}_{MAX} = \max_{0 \leq \theta < 2M\pi} |\tilde{\varepsilon}(\theta)| \quad (2-20)$$

(f) maximum total error motion:

$$\varepsilon_{MAX} = \max_{0 \leq \theta < 2M\pi} |\varepsilon(\theta)| \quad (2-21)$$

The above derivations are based on continuous motion measurements $x_p(\theta)$ and $y_p(\theta)$. When a test ball's motion is measured at discrete rotary locations with equally-spaced sample intervals, similar analysis can be carried out as shown in the Appendix C.

For the numerical example, Figure 2.11 shows the Fourier coefficients of the axis of rotation 2D radial error motion by eliminating the $k = 0$ and $k = +1$ components from Figure 2.11. The spindle error motion X and Y components $\bar{\varepsilon}_x(\theta)$ and $\bar{\varepsilon}_y(\theta)$ are shown in Figure 2.12.

Accordingly, the 2D radial error motion can be represented by the sum of rotating vectors, as shown in Figure 2.13. The calculation results for various specified error motion values (15)-(21) are listed in Table 2-1.

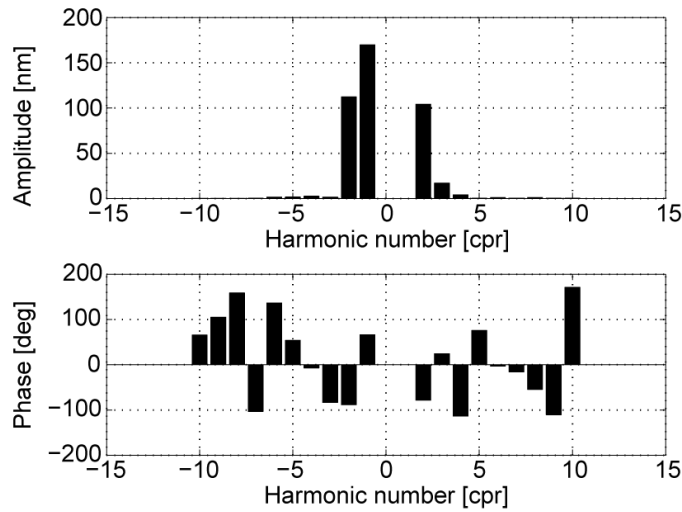


Figure 2.11. The Axis of rotation 2D radial error motion Fourier coefficients of the numerical example.

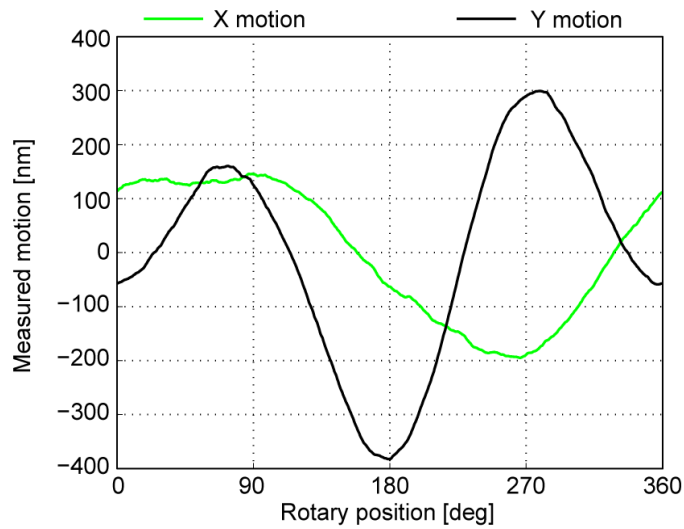


Figure 2.12. The Axis of rotation 2D radial error motion components of the numerical example.

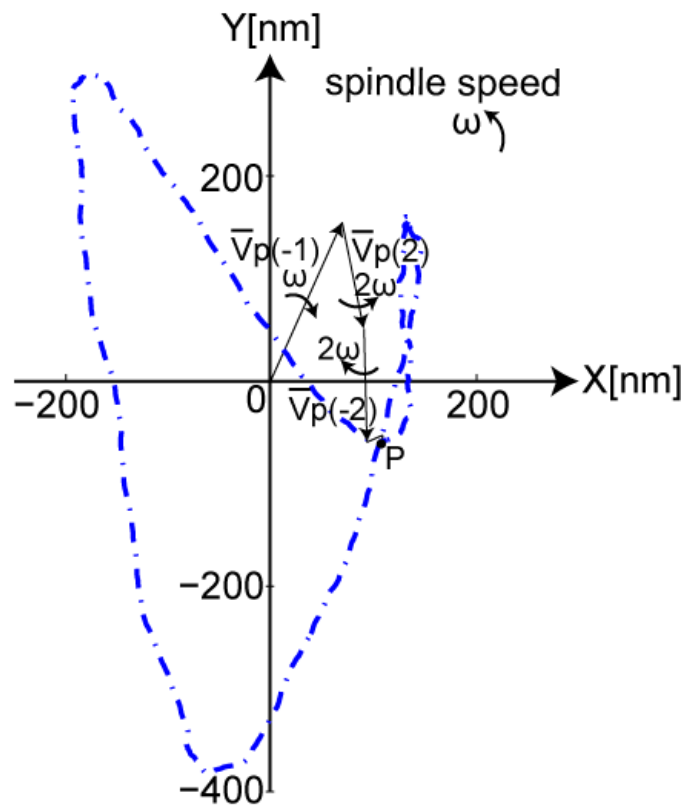


Figure 2.13. Vector representation of the 2D radial error motion of the numerical example.

Table 2-1. Various 2D error motion values of the numerical example.

Error motion	$\bar{\epsilon}_{RMS}$	$\tilde{\epsilon}_{RMS}$	ϵ_{RMS}	$\bar{\epsilon}_{MAX}$	$\tilde{\epsilon}_{MAX}$	ϵ_{MAX}
Values [nm]	229.5	8.8	230.0	387.4	22.7	407.5

2.3.4. Factors affecting spindle motion components

$\bar{V}_p(0)$ represents the average point (axis average line) location relative to the origin of the metrology frame. The origin is determined by the probe installation and zero-biasing adjustments and can be changed by adding a DC offset to the measurements. Given a fixed reference origin, the axis average line might shift during the test under different test conditions such as change in temperature, loads and speeds.

$\bar{V}_p(1)$ represents the motion of a test point with respect to the rotation center on the rotor. By changing the ball installation, the target ball center motion will match the motion of a different point on the rotor. The new test point on the rotor will have a different motion relative to the rotation center and as a result $\bar{V}_p[1]$ changes. Given a fixed ball installation point, the test point on the rotor will still change if the rotation center or the axis average line shift under different test conditions.

$\bar{V}_p(-1)$ is part of spindle error motion and does not depend on the location of axis average line or test ball eccentricity. This means choosing a different reference origin, shifting the axis average line, or changing the test ball installation point does not affect $\bar{V}_p[-1]$ component. On the other hand, changing test conditions such as temperature, speed, or load can change the affect $\bar{V}_p[-1]$ component. This is also true for any other harmonic of the measurement which represents spindle error motion. As a result, radial error motion vector $\varepsilon(\theta)$ excludes both $k = +1$ and $k = 0$ of the point P radial motion but should include $\bar{V}_p[-1]$ component.

2.3.5. Illustration of fundamental radial error motion

The axis of rotation fundamental (1 cpr) radial error motion is considered as non-existent in the current standards [2, 3]. In this section, the 2D radial error motion analysis is applied to some hypothetical examples to show that the fundamental ($k = -1$) radial error motion can actually exist.

Figure 2.14 shows the trajectories of labeled points on both a perfect spindle (a) and a spindle with fundamental radial error motion (b). Figure 2.14(a) shows the trajectories of 3 points (A_1 , A_2 , and A_3) on a perfect spindle rotor as it goes through one full revolution. The trajectories of all points are concentric circles. For a particular point such as A_1 , its X and Y motions are sinusoidal with identical amplitude, and the Y motion lags the X motion by 90

degrees. By applying Eq. (2-12) as shown in Table 2-2, the radial error motion of the spindle is always zero, regardless of test point selection (test ball installation); therefore, spindle A is a perfect spindle, which means there exists a point on the rotor that remains stationary relative to the metrology frame as the spindle rotates. This point is unique since standing on the metrology frame all other points on the rotor have a circular motion around this point in the direction of spindle rotation.

Figure 2.14(b) shows the trajectories of three points (B_1 , B_2 , and B_3) on a spindle with fundamental radial error motion as it goes through one full revolution. For a particular point B_1 , the trajectory is also circular where both the X and Y motions are once-per-revolution sinusoidal with equal amplitude; however, the Y motion leads the X motion by 90 [deg], which is opposite to the trajectory of A_1 in Figure 2.14(a). When the spindle rotates counter-clockwise, B_1 's motion can be represented by a vector rotating clockwise with respect to the circle center. The trajectories of other points on the same spindle rotor could be very different. For example, if a test ball is installed at B_2 or B_3 , the trajectory will be an ellipse or a straight line, respectively. This spindle is obviously not perfect, despite the fact that X and Y motion measurements of any point on the rotor are once per revolution sinusoidal. Applying Eq. (2-12) as shown in Table 2-2, the spindle exhibits a fundamental radial error motion rotating opposite to the spindle's main rotation, regardless of which point is selected.

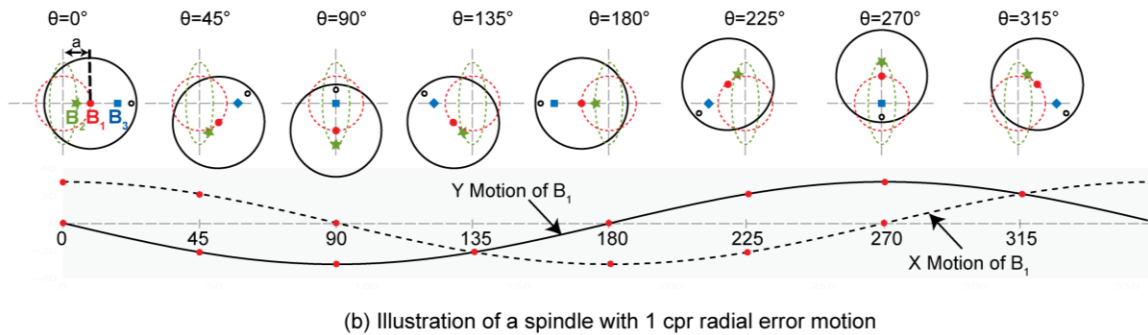
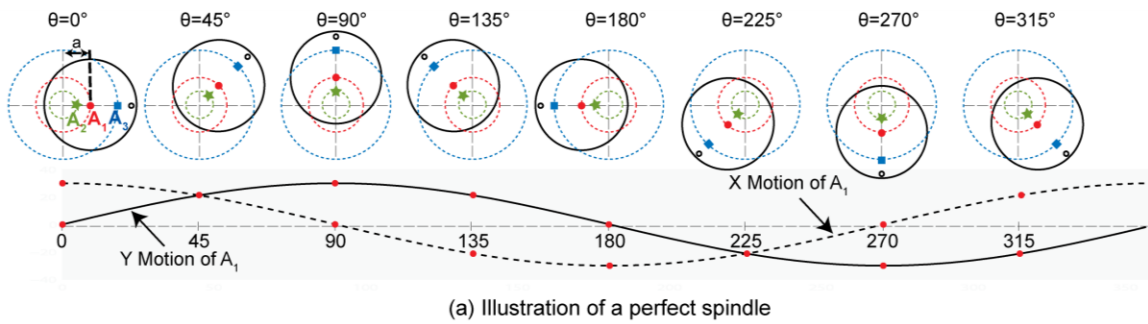
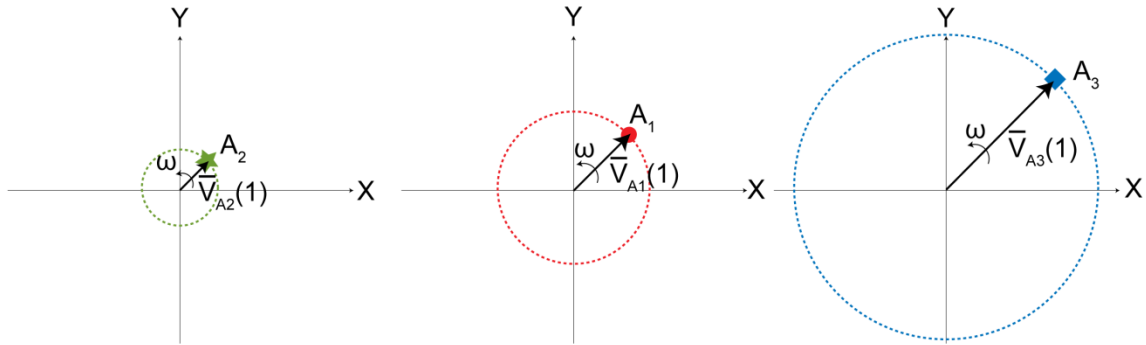


Figure 2.14. Comparison between a perfect spindle (a) and a spindle with fundamental radial error motion.

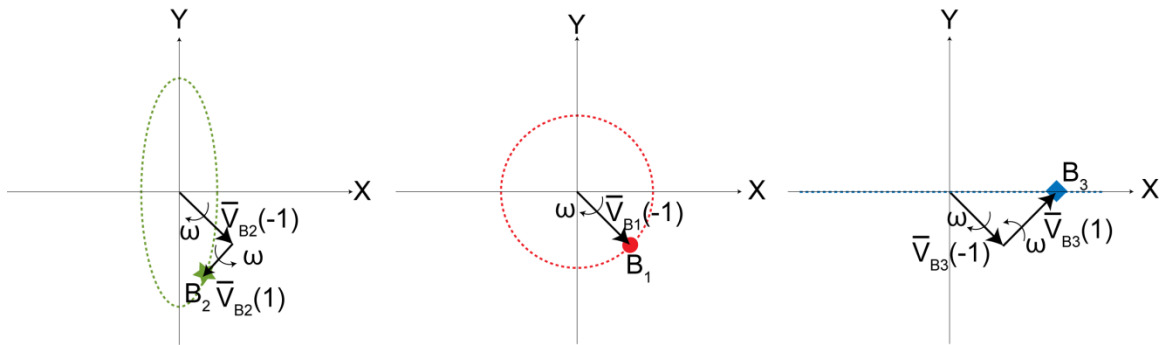
Comparing the trajectories in Figure 2.14, A_1 and B_1 both have a circular motion path, but belong to two different spindles. Therefore, the spindle error motion information cannot be found purely from the X-Y plot of test ball's motion measurements. Also, two points on the same spindle, such as B_1 and B_2 , can have very different trajectories in X-Y plane. Using the 2D method, the 1 cpr error motion of the spindle can be derived regardless of the test ball installation. The vector representation of these points at $\theta = 45^\circ$ is shown in Figure 2.15. Note that the $k = -1$ rotating vectors for points on the same spindle are the same, while the $k = +1$ rotating vectors can change significantly. This confirms that $V(-1)$ is a property of the spindle motion and $V(+1)$ is eccentricity of the test point.

Table 2-2. Spindle error motion calculation.

	Test point motion	Fourier Coefficient		Radial Error motion
		V(+1)	V(-1)	
Spindle in Figure 2.14(a)	$\bar{v}_{A_1}(\theta) = ae^{j\theta} + 0 \cdot e^{-j\theta}$	a	0	$\bar{\varepsilon}(\theta) = 0$
	$\bar{v}_{A_2}(\theta) = \frac{a}{2}e^{j\theta} + 0 \cdot e^{-j\theta}$	$\frac{a}{2}$	0	
	$\bar{v}_{A_3}(\theta) = 2ae^{j\theta} + 0 \cdot e^{-j\theta}$	$2a$	0	
Spindle in Figure 2.14(b)	$\bar{v}_{B_1}(\theta) = 0 \cdot e^{j\theta} + ae^{-j\theta}$	0	a	$\bar{\varepsilon}(\theta) = ae^{-j\theta}$
	$\bar{v}_{B_2}(\theta) = -\frac{a}{2}e^{j\theta} + ae^{-j\theta}$	$-\frac{a}{2}$	a	
	$\bar{v}_{B_3}(\theta) = ae^{j\theta} + ae^{-j\theta}$	a	a	



(a) Illustration of a perfect spindle at $\theta=45^\circ$



(b) Illustration of a spindle with 1 cpr radial error motion at $\theta=45^\circ$

Figure 2.15. Vector decomposition of test point motion: (a) Perfect spindle. (b) Spindle with fundamental radial error motion.

2.4. Radial error motion consequence in various spindle applications

Based on the test ball motion measurement, section 2.3 gave the actual radial error motion of axis of rotation with respect to a specified reference frame, regardless of whether the spindle is used to make something or how the spindle is used in a particular application. In this sense, the axis of rotation radial error motion is a pure geometric property, representing the deviation between the axis of rotation and the axis average line.

From application point view, a spindle user may be only concerned with the consequence of axis of rotation error motion under a particular spindle application scenario, instead of the axis of rotation error motion itself. As discussed in section 1.4.1. axis of rotation error motion and its consequence in a particular spindle application are two related but distinct concepts: error motion consequence is certainly caused by error motion, but consequence also depends on the application details, such as how the cutting tools are installed, how many tools are installed, what type of parts to be made, and so on. Whenever the axis of rotation error motion consequence is discussed, the full details of the spindle application should be clearly specified. As far as radial error motion is concerned, spindle applications are classified into two categories: applications with single radial sensitive direction and applications with two radial sensitive directions. Each category can be further subdivided as shown in Figure 2.16.

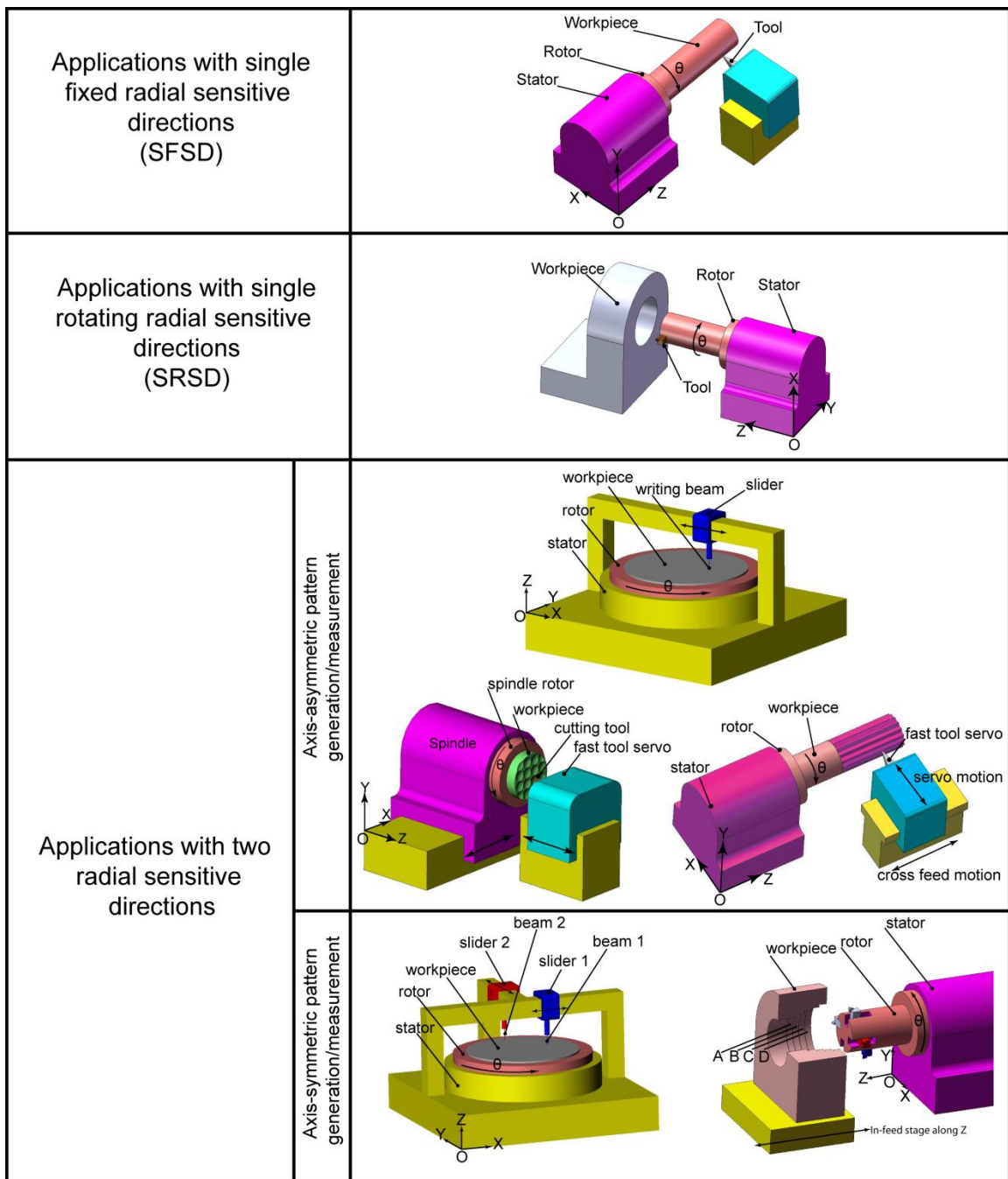


Figure 2.16. Categories of spindle applications based on radial sensitive direction

In the following sections, the new 2D method is used to derive the consequence of spindle radial error motion in all types of applications shown in Figure 2.16. Three case studies will also be presented to illustrate the difference between the actual radial error motion and its consequence.

2.4.1. Applications with single radial sensitive direction

Applications with the single radial sensitive direction refer to those applications which are affected by error motion in only one particular radial direction and are insensitive to error motion in the other orthogonal radial direction. Depending on whether this radial direction is fixed or rotating with respect to the reference frame, the application is referred to as single fixed radial direction (SFSD) or single rotating radial direction (SRSD). As shown in Figure 2.17, the specified radial sensitive direction has angle ϕ with reference to the X axis, and $\varepsilon(\theta)$ is the spindle radial error motion vector calculated according to Eq. (2-11). Generally, $\varepsilon(\theta)$'s phase angle α (the angle between vector $\varepsilon(\theta)$ and the X axis) has no direct relation to the spindle rotary position θ . The radial error motion in the specified sensitive direction is represented by $\varepsilon_\phi(\theta)$, which is the projection of the vector $\varepsilon(\theta)$ on the unity vector $e^{j\phi}$:

$$\varepsilon_\phi(\theta) = \text{Re}[\varepsilon(\theta)e^{-j\phi}] = \varepsilon_x(\theta)\cos\phi + \varepsilon_y(\theta)\sin\phi \quad (2-22)$$

where $\varepsilon_x(\theta)$ and $\varepsilon_y(\theta)$ are the X (real) and Y (imaginary) components of error motion vector $\varepsilon(\theta)$.

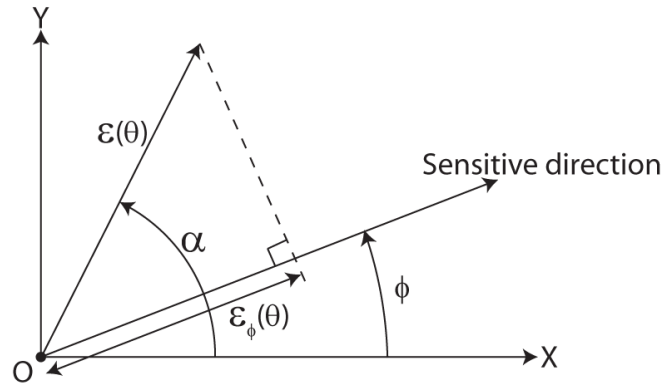


Figure 2.17. The relation between $\varepsilon(\theta)$ (radial error motion) and $\varepsilon_\phi(\theta)$ (the radial error motion in a specified direction).

Further, the synchronous component $\bar{\varepsilon}_\phi(\theta)$ and asynchronous component $\tilde{\varepsilon}_\phi(\theta)$ can be calculated as:

$$\bar{\varepsilon}_\phi(\theta) = \text{Re}[\bar{\varepsilon}(\theta)e^{-j\phi}] = \text{Re}\left[\sum_{\substack{k=-\infty \\ k \neq 0,1}}^{\infty} \bar{V}_p(k)e^{j(k\theta-\phi)}\right] = \bar{\varepsilon}_x(\theta)\cos\phi + \bar{\varepsilon}_y(\theta)\sin\phi \quad (2-23)$$

and

$$\tilde{\varepsilon}_\phi(\theta) = \text{Re}[\tilde{\varepsilon}(\theta)e^{-j\phi}] = \tilde{x}_p(\theta)\cos\phi + \tilde{y}_p(\theta)\sin\phi \quad (2-24)$$

2.4.1.1. Applications with single fixed radial sensitive direction (SFSD)

As discussed in the current spindle standards [2, 3], an example of SFSD application is outside cylinder surface turning with a fixed cutting tool, where the sensitive direction angle is a constant: $\phi = \phi_0$. According to Eq. (2-23), the spindle synchronous radial error motion in the specified fixed sensitive direction can be calculated from test ball's motion measurement:

$$\bar{\varepsilon}_{\phi_0}(\theta) = \text{Re} \left[\sum_{\substack{k=-\infty \\ k \neq 0,1}}^{\infty} \bar{V}_p(k)e^{j(k\theta-\phi_0)} \right] = \bar{\varepsilon}_x(\theta)\cos\phi_0 + \bar{\varepsilon}_y(\theta)\sin\phi_0 \quad (2-25)$$

In general, there exists a once-per-revolution component $\text{Re}[\bar{V}_p(-1)e^{j(-\theta-\phi_0)}]$ in $\bar{\varepsilon}_{\phi_0}(\theta)$. The main consequence of $\text{Re}[\bar{V}_p(-1)e^{j(-\theta-\phi_0)}]$ in this example (turning axis-symmetric surface with single fixed tool) is that the produced part center is offset from the axis of rotation by a distance of $|\bar{V}_p(-1)|$. Another consequence brought by $\text{Re}[\bar{V}_p(-1)e^{j(-\theta-\phi_0)}]$ is part out-of-roundness with amplitude $|\bar{V}_p(-1)|^2/2R$, which is a second-order effect of $|\bar{V}_p(-1)|$ and therefore is negligible. Therefore, this once-per-revolution component $\text{Re}[\bar{V}_p(-1)e^{j(-\theta-\phi_0)}]$ does not produce defect or error on the finished part. Accordingly, $\bar{\varepsilon}_{\phi_0}(\theta)$'s consequence in this SFSD application, $\bar{A}_{\phi_0}(\theta)$, should exclude the once-per-revolution component:

$$\bar{A}_{\phi_0}(\theta) = \bar{\varepsilon}_{\phi_0}(\theta) - \text{Re}[\bar{V}_p(-1)e^{-j(\theta+\phi_0)}] = \text{Re} \left[\sum_{\substack{k=-\infty \\ k \neq -1,0,1}}^{\infty} \bar{V}_p(k)e^{j(k\theta-\phi_0)} \right] \quad (2-26)$$

In particular, when the fixed sensitive direction is X, $\phi_0 = 0$ and the synchronous radial error motion consequence is

$$\bar{A}_x(\theta) = \text{Re} \left[\sum_{\substack{k=-\infty \\ k \neq -1,0,1}}^{\infty} \bar{V}_p(k)e^{j(k\theta)} \right] \quad (2-27)$$

Similarly, when the fixed sensitive direction is Y, $\phi_0 = \pi/2$ and the synchronous radial error motion consequence is

$$\bar{A}_y(\theta) = \text{Re} \left[\sum_{\substack{k=-\infty \\ k \neq -1, 0, 1}}^{\infty} \bar{V}_p(k) e^{j(k\theta - \pi/2)} \right] \quad (2-28)$$

The asynchronous radial error motion consequence is the asynchronous error motion projection in the sensitive direction:

$$\tilde{A}_{\phi_0}(\theta) = \tilde{\varepsilon}_{\phi_0}(\theta) = \tilde{x}_p(\theta) \cos \phi_0 + \tilde{y}_p(\theta) \sin \phi_0 \quad (2-29)$$

2.4.1.2. Applications with single rotating radial sensitive direction (SRSD)

As discussed in the current spindle motion standards [2, 3], an example of SRSD is the operation of boring a round hole with single tool attached to the spindle rotor, where the sensitive direction rotates synchronously with the spindle rotor and its phase angle is $\phi = \theta$. According to Eq. (2-23), the spindle synchronous radial error motion in the specified rotating sensitive direction can be calculated from the test ball's motion measurement as:

$$\begin{aligned} \bar{\varepsilon}_{\theta}(\theta) &= \text{Re}[\bar{\varepsilon}(\theta) e^{-j\theta}] \\ &= \text{Re} \left[\sum_{\substack{k=-\infty \\ k \neq 0, 1}}^{\infty} \bar{V}_p(k) e^{j(k-1)\theta} \right] \\ &= \bar{\varepsilon}_x(\theta) \cos \theta + \bar{\varepsilon}_y(\theta) \sin \theta \end{aligned} \quad (2-30)$$

Clearly, the spindle synchronous radial error motion vector $\bar{\varepsilon}(\theta)$ is modulated by the rotating vector $e^{-j\theta}$ in Eq. (2-30). As a result, the k -cpr component $\bar{V}_p(k) e^{jk\theta}$ in $\bar{\varepsilon}(\theta)$ will become the $(k-1)$ -cpr component $\text{Re}[\bar{V}_p(k) e^{j(k-1)\theta}]$ in $\bar{\varepsilon}_{\theta}(\theta)$. In general, there exists a once-per-revolution component $\text{Re}[\bar{V}_p(2) e^{j\theta}]$ in $\bar{\varepsilon}_{\theta}(\theta)$, due to the spindle synchronous error motion at $k=2$ cpr. The main effect of this 1-cpr component $\text{Re}[\bar{V}_p(2) e^{j\theta}]$ in the example of boring axis-symmetric hole surfaces with single tool is that the produced part center is offset from the axis of rotation by a distance of $|\bar{V}_p(2)|$. Another effect is the hole out-of-roundness error with amplitude $|\bar{V}_p(2)|^2 / 2R$, which is a second-order effect of $|\bar{V}_p(2)|$. All these are not considered as out-of-roundness errors. Therefore the synchronous radial error motion consequence in SRSD application, $\bar{A}_{\theta}(\theta)$, does not include the once-per-revolution component:

$$\bar{A}_\theta(\theta) = \bar{\varepsilon}_\theta(\theta) - \text{Re}[\bar{V}_p(2)e^{j\theta}] = \text{Re} \left[\sum_{\substack{k=-\infty \\ k \neq 0,1,2}}^{\infty} \bar{V}_p(k)e^{j(k-1)\theta} \right] \quad (2-31)$$

The asynchronous error motion consequence in SRSD application can be derived directly from the spindle asynchronous error motion projection in the sensitive direction as:

$$\tilde{A}_\theta(\theta) = \tilde{\varepsilon}_\theta(\theta) = \tilde{x}_p(\theta)\cos\theta + \tilde{y}_p(\theta)\sin\theta \quad (2-32)$$

For the numerical example, Figure 2.18 shows the synchronous radial error motion consequence in applications with single sensitive direction in X, Y, and the rotating direction. For comparison, the spindle synchronous radial error motions in the specified sensitive directions are also shown. Clearly, radial error motion and its consequence are very different.

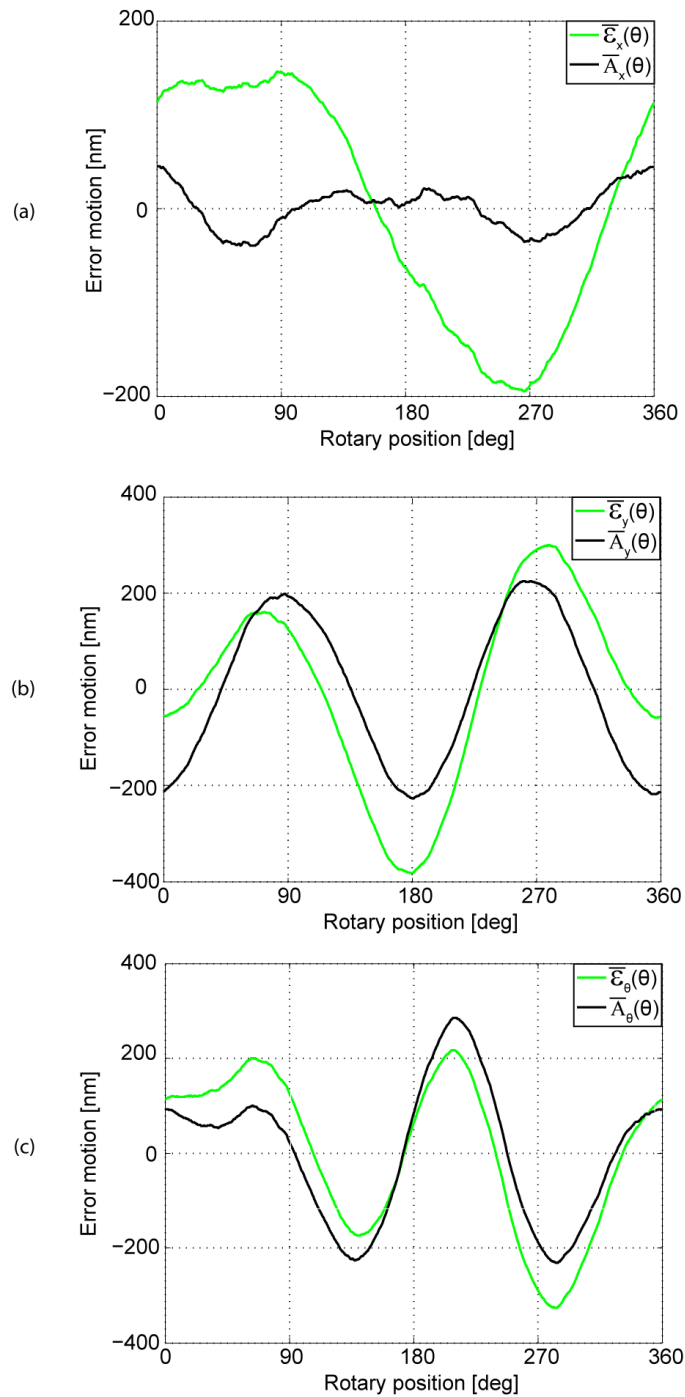


Figure 2.18. Comparison between the spindle radial error motion and its consequence in applications with single radial sensitive direction: (a) in X direction, (b) in Y direction, and (c) in a rotating direction.

2.4.2. Applications with two sensitive directions (TSD)

Applications with two radial sensitive directions refer to those applications which are simultaneously sensitive to spindle error motion in two radial directions, such as 2D or axis-asymmetric pattern generation and measurement. One example is turning axis-asymmetric

patterns with a fast tool servo (FTS) on a lathe. As shown in Figure 2.19, the horizontal turning spindle is mounted on the cross slide traveling in the X direction, and the fast tool servo on the in-feed slide can generate fast cutting tool motion in the Z direction. In face turning of a three dimensional sculptured surface, the desired Z motion of the fast tool servo changes with the spindle angular position and the cross slide position in the X axis. Spindle rotor radial error motion in both X and Y will result in radial dislocation of each feature relative to their desired positions. The process of turning a sculptured surface on a cylinder drum with a FTS also has two sensitive directions, as shown in Figure 2.20.

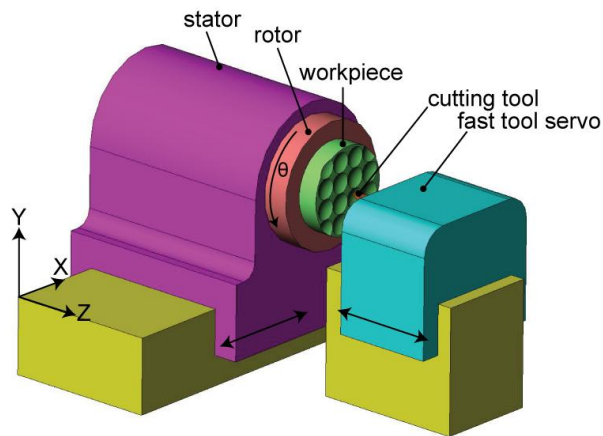
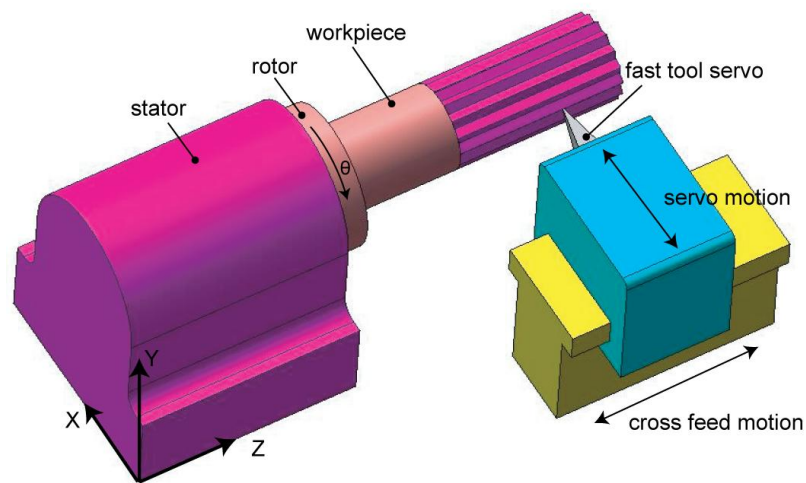
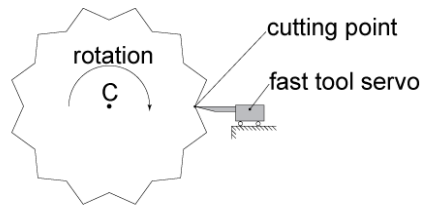


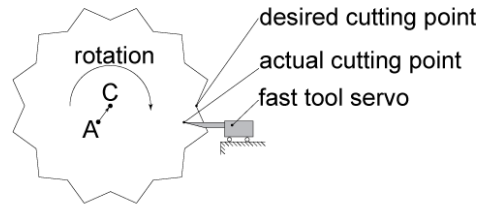
Figure 2.19. Face turning of axis-asymmetric patterns with a fast tool servo.



(a) Machine configuration



(b) Free-form surface turning on an ideal spindle



(c) Free-form surface turning on a spindle with radial error motion

Figure 2.20. Axis-asymmetric pattern turning on a drum lathe with a fast tool servo.

Applications with TSD are not limited to processes involving axis-asymmetric patterns. In some instances of axis-symmetric pattern generation with multiple tools, the produced parts can be affected by spindle error motion in two radial directions. This is discussed later in section 2.4.4.

In spindle applications with TSD, the radial error motion consequence should include all radial error motion components:

$$\bar{A}(\theta) = \bar{\varepsilon}(\theta) = \sum_{\substack{k=-\infty \\ k \neq 0,1}}^{\infty} \bar{V}_p(k) e^{jk\theta} \quad (2-33)$$

and

$$\tilde{A}(\theta) = \tilde{\varepsilon}(\theta) = \tilde{v}_p(\theta) \quad (2-34)$$

2.4.3. Case study: Beam writing on a spindle with fundamental radial error motion

Figure 2.21 shows a rotary beam writing process, used in applications such as optical disk mastering with a laser, electron beam lithography, and plasmonic lithography [19]. The overall structure is a vertical spindle and bridge type machine. A beam writer is attached to a linear slider that travels in the X direction. A substrate is installed on top of the spindle rotor to be written with some desired patterns. When the writing beam on/off is properly synchronized with the slider's X position and the spindle's rotary angle, arbitrary two-dimensional patterns can be generated on the substrate.

In order to evaluate the effect of the fundamental ($k = -1$) radial error motion in this spindle application, the motion of the spindle rotation center (the intersection between the axis of rotation and the substrate top surface) is assumed to be:

$$\begin{cases} x_c(\theta) = \cos(\theta) \\ y_c(\theta) = -\sin(\theta) \end{cases} \quad (2-35)$$

In the following sub-sections, several pattern examples and radial error motion consequences are discussed.

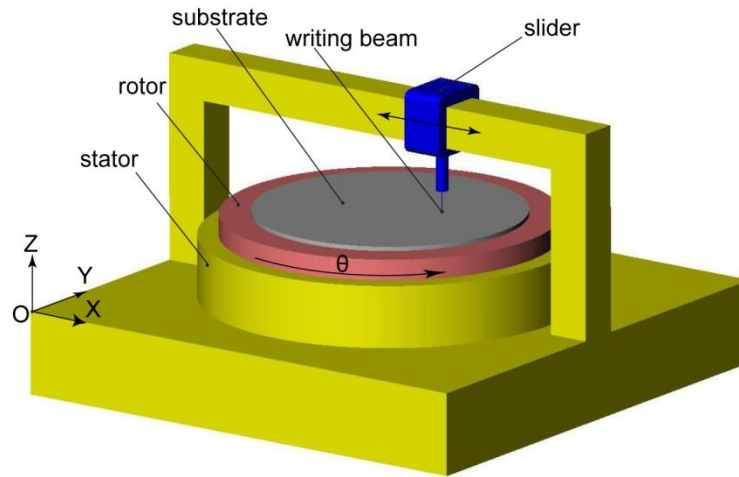


Figure 2.21. A rotary beam writing machine.

2.4.3.1. Axis-symmetric pattern writing with one tool

In this case, the desired pattern is a circle, and only one beam writer is used as shown in Figure 2.22. For such pattern writing, the beam writer needs to position itself at a fixed location and then turn the beam on all the time. This is an application with a fixed radial sensitive direction, similar to turning a cylindrical surface on a vertical lathe. If a spindle with error motion of Eq. (2-35) were examined with the fixed sensitive direction method [3], the radial error motion value would be zero as the fundamental component is removed in the current standards.

Figure 2.22 shows the simulated pattern on the work piece. Although the produced pattern center is offset from the spindle rotation center, the pattern deviation from a perfect circle is negligible, much less than the spindle $k = -1$ error motion magnitude of 1. Therefore, the value specified by the fixed sensitive direction method can effectively predict the consequence of the spindle error motion in this application case.

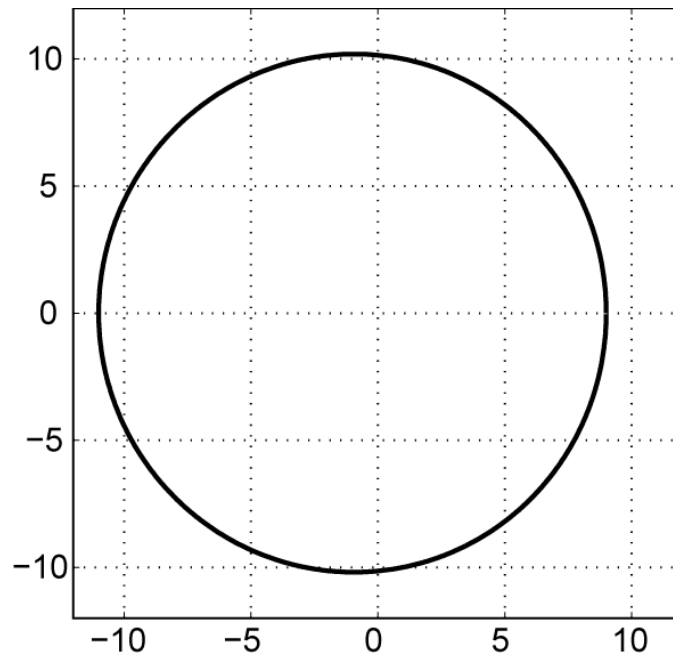


Figure 2.22. The simulated pattern when the desired pattern is a circle. The origin is the spindle rotation center.

2.4.3.2. Axis-asymmetric pattern writing with one tool

In this case, the desired pattern is a cross as shown in Figure 2.23(a) and the setup is the same as shown in Figure 2.21. Obviously, the cross pattern is axis-asymmetric. In order to produce such a pattern on a perfect spindle, at each radial location, the beam writer needs to be momentarily turned on at spindle rotary angles 0, 90, 180, and 270 degrees, and remain off at other rotary positions of the spindle.

When the spindle has the fundamental radial error motion of Eq. (2-35), the produced pattern is shown in Figure 2.23(b). There exists significant distortion: the intersection point of is not the center of the horizontal line, and is shifted by a distance 1, which is the fundamental radial error motion amplitude. Such distortion indicates that this spindle is not perfect, although it can produce an axis-symmetric pattern as shown previously in Figure 2.22. Therefore, the spindle application of writing an axis-asymmetric pattern with single tool is an example of an application with two radial sensitive directions, and the 2D method is required to predict the consequence of spindle error motion.

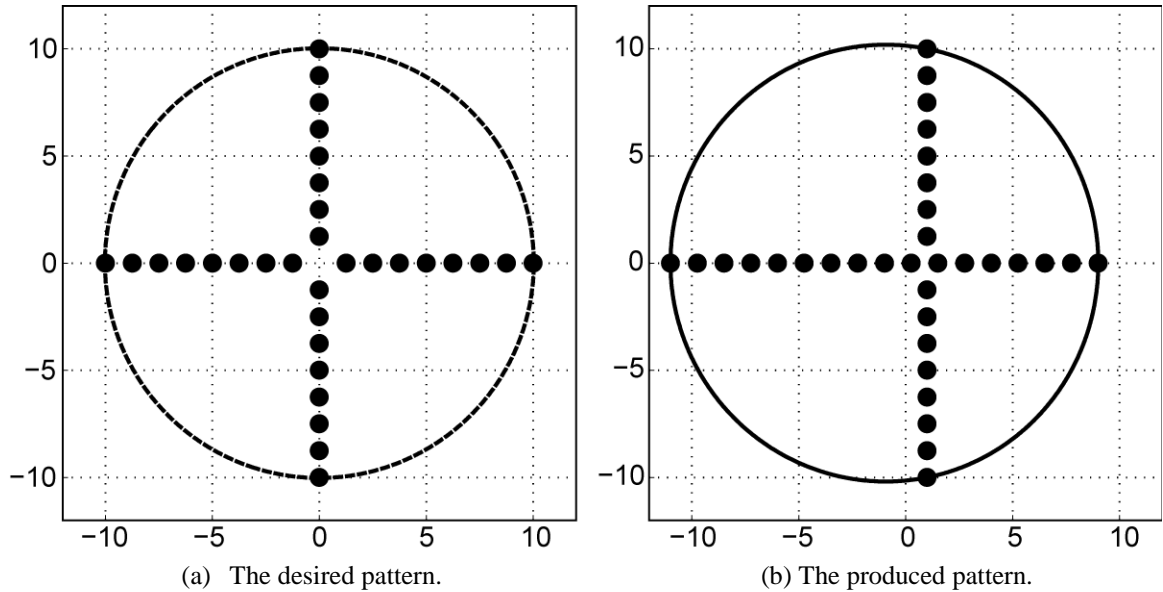


Figure 2.23. Simulated result of axis-asymmetric pattern writing with single beam. Instead of lines, only discrete points are shown.

2.4.3.3. Axis-symmetric pattern writing with multiple tools

In this case, the machine setup is shown in Figure 2.24. Two tools are installed at different radial locations, either to speed up the writing process or for on-line inspection.

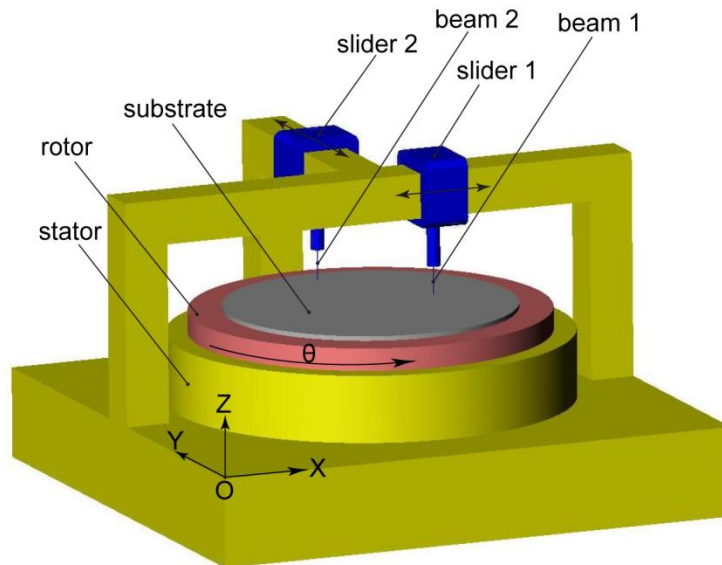


Figure 2.24. A multi-beam rotary writing machine.

As shown in Figure 2.25(a), the desired pattern is two concentric circles. Slider 1 is used to produce the bigger circle of radius 10 and slider 2 is used to produce the smaller circle of radius

8. Once these two sliders are positioned properly, they are held stationary and the beams remain on during the spindle rotation process.

Figure 2.25(b) shows the simulated pattern produced on a spindle with fundamental radial error motion. There exists significant deviation from the desired pattern as the two circles are not concentric at all. Both circle centers are shifted away from the spindle rotation center by the amplitude of the fundamental error motion, but in opposite directions. Therefore, the spindle application of writing an axis-symmetric pattern with two tools has two radial sensitive directions.

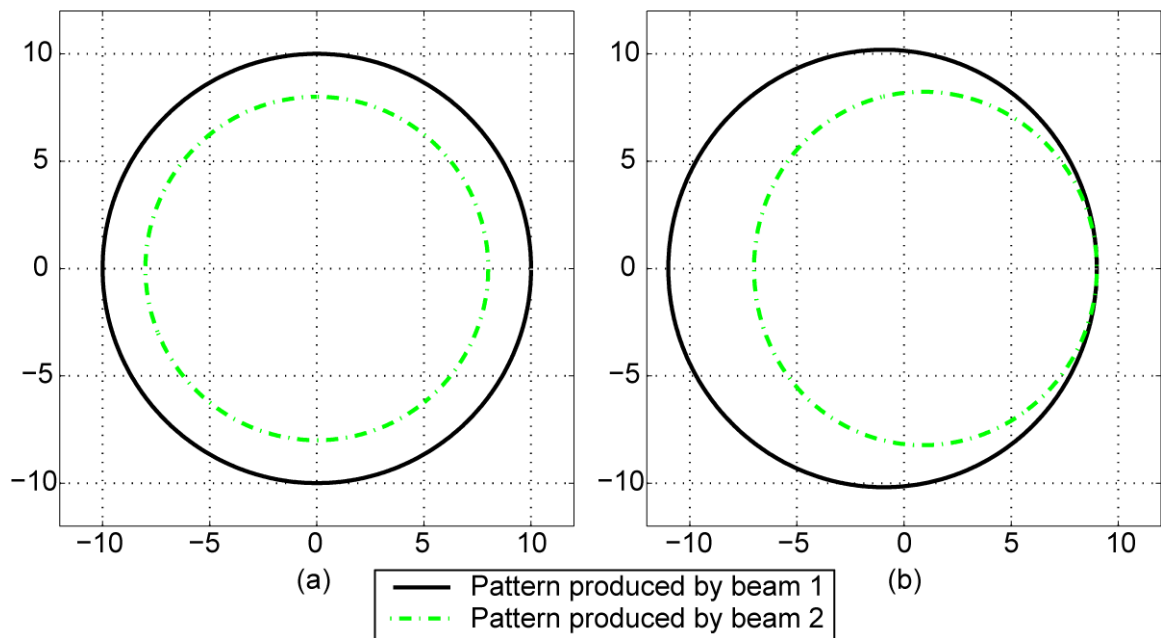


Figure 2.25. Axis-symmetric pattern writing with two beams. (a) the desired pattern. (b) the produced pattern on a spindle with fundamental radial error motion.

This example demonstrates that the fixed radial sensitive direction method in the current standards can predict the consequence of spindle radial error motion in single beam writing of axis symmetric pattern. On the other hand, it cannot predict the consequence of fundamental spindle error motion in single beam writing of axis-asymmetric patterns or multi-beam writing.

2.4.4. Case study: Multi-tool boring on a spindle with 2-cpr error motion

Figure 2.26 shows the setup of multi-tool boring operation. Four boring tools are installed to produce four concentric step holes in one boring operation. The advantage is higher productivity and balanced cutting forces for improved machining accuracy. In order to evaluate the effect of $k = 2$ radial error motion in this spindle application, the motion of the rotation center motion of the spindle is assumed to be:

$$\begin{cases} x_C(\theta) = \cos(2\theta) \\ y_C(\theta) = \sin(2\theta) \end{cases} \quad (2-36)$$

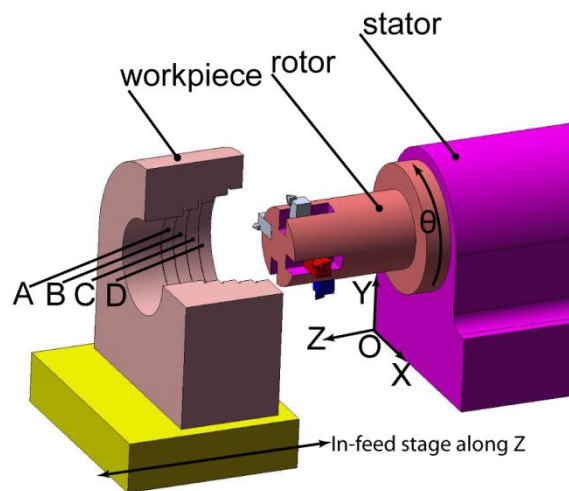


Figure 2.26. Multi-tool boring operation. Four concentric holes are produced in a single boring operation.

As pointed out in [7], the rotating sensitive direction method gives zero error for this spindle, which means that each single boring tool installed on this spindle can produce a round hole with negligible distortion. However, when multiple tools are combined together in step-boring operation, the $k = 2$ radial error motion can generate significant distortion. If looking at the simulated holes produced by two orthogonal tools as shown in Figure 2.27, they are not concentric at all. Therefore, the $k = 2$ radial error motion can produce consequences that cannot be predicted by the rotating sensitive direction method in the current standards.

This example demonstrates that the rotating sensitive direction method in the current standards can predict the consequences of spindle radial error motion in single tool boring but cannot predict the distortion caused by 2-cpr spindle error motion in multi-tool boring. The 2D method needs to be used for spindle applications with two rotating radial sensitive directions.

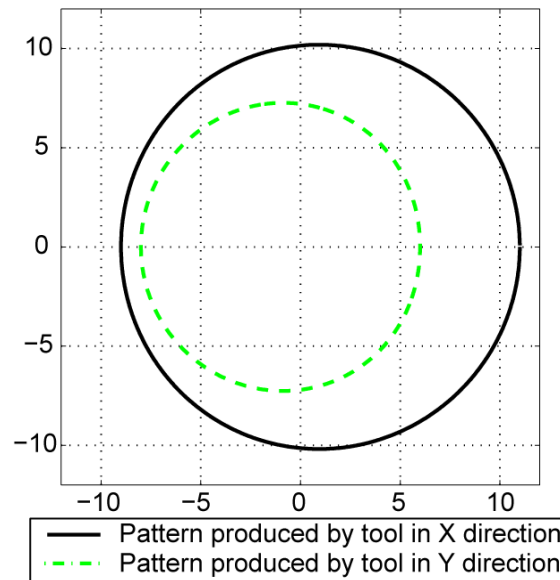


Figure 2.27. Holes produce by two orthogonal boring tools.

2.5. Comparison between 2D method and current standard methods

This section illustrates the differences between the new 2D method and the current standard methods. As discussed in section 1.2 current standard methods employ polar plots to characterize spindle error motion. The problem with this approach can be summarized as follows

1. Polar plots do not give a full picture of axis of rotation radial error motion.
2. The fundamental error motion of the spindle cannot be identified.
3. Polar plots cannot predict consequence of spindle error motion when there are more than one sensitive direction.

In the following section, the 2D framework will be used to illustrate the problems mentioned above. It will be shown that current standard methods are sufficient to predict error motion consequences when there is a single sensitive direction. On the other hand, the 2D method gives a full description of radial error motion and can be used to characterize spindles for any type of application. A case study is also presented to further illustrate the difference between current standard methods and the new 2D analysis.

2.5.1. Implementation of the current standard methods in the 2D framework

As illustrated in the section 1.3, the least squares fitting method and the frequency domain method are equivalent in calculating radial error motion from polar plots when the base-circle radius is big enough. Therefore, the following analysis will be carried out using only the frequency domain method.

Using the 2D framework, the synchronous measurement polar plot for the rotating sensitive direction method is

$$\begin{aligned}
 \bar{r}_\theta(\theta) &= r_0 + \bar{x}_p(\theta) \cos\theta + \bar{y}_p(\theta) \sin\theta \\
 &= r_0 + \text{Re}[\bar{v}_p(\theta)e^{-j\theta}] \\
 &= r_0 + \text{Re}\left[\sum_{k=-\infty}^{\infty} \bar{V}_p(k)e^{j(k-1)\theta}\right]
 \end{aligned} \tag{2-37}$$

The DC component in $\bar{r}_\theta(\theta)$ is $r_0 + \text{Re}[\bar{V}_p(1)]$, and the fundamental component is $\text{Re}[\bar{V}_p(0)e^{-j\theta} + \bar{V}_p(2)e^{j\theta}]$. Removing these components as specified by the standards, the radial error motion for the rotating sensitive direction is:

$$\bar{\rho}_\theta(\theta) = \text{Re}\left[\sum_{\substack{k=-\infty \\ k \neq 0,1,2}}^{\infty} \bar{V}_p(k)e^{j(k-1)\theta}\right] \tag{2-38}$$

Note that the error motion component $\bar{V}_p(2)$ is excluded in the rotating sensitive direction method, as pointed out by Donaldson [7]. In comparison with the 2D analysis, the error motion specified by the rotating sensitive direction method, $\bar{\rho}_\theta(\theta)$, is the same as the spindle radial error motion consequence in application with SRSD $\bar{A}_\theta(\theta)$ (Eq. (2-31)), not the synchronous error motion in the rotating direction $\bar{\varepsilon}_\theta(\theta)$ (Eq. (2-30)).

For the fixed sensitive direction method, the synchronous polar plot is

$$\begin{aligned}
 \bar{r}_{\phi_0}(\theta) &= r_0 + \bar{x}_p(\theta) \cos\phi_0 + \bar{y}_p(\theta) \sin\phi_0 \\
 &= r_0 + \text{Re}[\bar{v}_p(\theta)e^{-j\phi_0}] \\
 &= r_0 + \text{Re}\left[\sum_{k=-\infty}^{\infty} \bar{V}_p(k)e^{j(k\theta-\phi_0)}\right]
 \end{aligned} \tag{2-39}$$

The DC component in $\bar{r}_{\phi_0}(\theta)$ is $r_0 + \text{Re}[\bar{V}_p(0)e^{-j\phi_0}]$ and the fundamental component is $\text{Re}[\bar{V}_p(-1)e^{-j\theta-j\phi_0} + \bar{V}_p(1)e^{j\theta-j\phi_0}]$. After removing these components, the radial error motion in the ϕ_0 sensitive direction specified in the current standards is

$$\bar{\rho}_{\phi_0}(\theta) = \text{Re} \left[\sum_{\substack{k=-\infty \\ k \neq -1, 0, 1}}^{\infty} \bar{V}_p(k) e^{j(k\theta - \phi_0)} \right] \quad (2-40)$$

Note that the error motion component $\bar{V}_p(-1)$ is excluded in the fixed sensitive direction method. In comparison with the 2D analysis, the error motion specified by the fixed sensitive direction method, $\bar{\rho}_{\phi_0}(\theta)$, is the spindle radial error motion consequence in application with SFSD, $\bar{A}_{\phi_0}(\theta)$ (Eq. (2-26)), not the synchronous error motion in the ϕ_0 direction, $\bar{\varepsilon}_{\phi_0}(\theta)$ (Eq. (2-25)).

Another observation in the above analysis is that the same error motion component can have a different cpr in the fixed frame and in the rotating frame. The $k = -1$ error motion, $\bar{V}_p(-1)e^{-j\theta}$ will be 1 cpr or fundamental in a fixed radial direction, but will become 2 cpr in a rotating radial direction due to modulation effect. Similarly, the $k = 2$ error motion, $\bar{V}_p(2)e^{j2\theta}$, will be 2 cpr in a fixed radial direction, but will become 1 cpr or fundamental in a rotating radial direction.

Table 2-3 summarizes the above results in terms of error motion and its consequence. It shows that the radial error motion values specified in the current standards are radial error motion consequence in spindle application with single radial sensitive direction. For this type of application, the current standards are sufficient to evaluate axis of rotation radial error motion effect. For spindle application with two radial sensitive directions, the 2D method needs to be used. In addition, the 2D method is able to give the actual radial error motion in any direction. In the next section, a case study is presented to illustrate this with more details.

Table 2-3. Radial error motion comparison between the current standards and the 2D method.

Physical meaning		Existing methods	2D method
Radial error motion	In a fixed direction	N/A	$\bar{\varepsilon}_{\phi_0}(\theta)$
	In a rotating direction	N/A	$\bar{\varepsilon}_{\theta}(\theta)$
	In two dimensions	N/A	$\bar{\varepsilon}(\theta)$
radial error motion consequence in spindle applications	Application with SFSD	$\bar{\rho}_{\phi_0}(\theta)$	$\bar{A}_{\phi_0}(\theta)$
	Application with SRSD	$\bar{\rho}_{\theta}(\theta)$	$\bar{A}_{\theta}(\theta)$
	Application with TSD	N/A	$\bar{A}(\theta)$

2.5.2. Case study: spindle with 1,2, and 3 cpr radial error motion

In this example, it is assumed that the test ball measurement data from two orthogonal radial probes are:

$$\begin{cases} x_p(\theta) = 6\cos(\theta) + 3\cos(2\theta) - \cos(3\theta) \\ y_p(\theta) = 4\sin(\theta) + 3\sin(2\theta) - \sin(3\theta) \end{cases} \quad (2-41)$$

By combining the measurement data into a vector, the 2D radial motion of the test ball can be expressed as:

$$v_p(\theta) = x_p + jy_p = 5e^{j\theta} + e^{-j\theta} + 3e^{j2\theta} - e^{j3\theta} \quad (2-42)$$

Eliminating the $k=1$ component (the eccentricity of the test ball), the 2D error motion of the axis of rotation becomes:

$$\varepsilon(\theta) = e^{-j\theta} + 3e^{j2\theta} - e^{j3\theta} \quad (2-43)$$

According to the current standards, the polar plot in the fixed X direction is

$$\bar{r}_X(\theta) = r_0 + 6\cos(\theta) + 3\cos(2\theta) - \cos(3\theta) \quad (2-44)$$

The radial error motion in the X direction specified by the standards, $\rho_X(\theta)$, is obtained by removing the fundamental component from the polar plot as discussed in section 1.3:

$$\rho_X(\theta) = 3\cos(2\theta) - \cos(3\theta) \quad (2-45)$$

Similarly, the radial error motion in the Y direction specified by the standards is:

$$\rho_Y(\theta) = 3\sin(2\theta) - \sin(3\theta) \quad (2-46)$$

Eq. (2-45) and Eq. (2-46) show that the fixed sensitive direction method is blind to the $k=-1$ fundamental radial error motion component.

For the rotating sensitive direction method in the current standards, the radial error motion polar plot is:

$$\bar{r}_\theta(\theta) = r_0 + x_p \cos\theta + y_p \sin\theta = r_0 + 5 + 3\cos\theta \quad (2-47)$$

After removing the fundamental component and the DC component from Eq. (2-47), the radial error motion along the rotating sensitive direction specified by the standards becomes:

$$\varepsilon_\theta(\theta) = 0 \quad (2-48)$$

The rotating sensitive direction method is unable to capture the radial error motion that rotates at twice the spindle speed, as pointed out in [7]. In addition, the rotating sensitive direction polar plot (Eq. (2-47)) is unable to tell the difference between $k=-1$ and $k=3$ radial error motion components. For the example shown, the radial error motion value specified by the rotating sensitive direction method missed all 3 error motion components in the 2D radial error motion Eq. (2-43).

Chapter 3. Experimental results

Experiments

This chapter presents the experiments carried out on two types of spindle: 1) ball bearing spindle in a Mori Seiki high-speed 5 Axis machining center, and 2) an aerostatic bearing spindle(10R Block-Head by Professional Instruments). Using the new 2D method, the radial error motion of the spindles are measured and analyzed. In addition, the consequence of these error motions in spindle applications is obtained. Furthermore, the 2D method analysis is compared against the result obtained using current standard methods.

3.1. General consideration

The aim of the spindle metrology setup is to measure the actual motion of the test ball center in X-Y plane as a function of the spindle rotary angle. Probe misalignment with the target ball center, target ball curvature, aliasing, and indexing introduce uncertainty in the measurements. To make sure the capacitance probe read outs are meaningful, these issues are addressed in the following subsections.

3.1.1. Probe misalignment with the target ball center

As discussed in section 2.2., in the ideal test setup shown in Figure 2.1, the probes are aligned with P_{ball} which is the least squares center of the ball profile in the cross-sectional plane where the two indicators are installed. This ensures that roundness profile measured by the probe is the actual roundness profile of the target ball, $r_{ball}(\theta)$. For the ideal setup, the measurements in X and Y directions are:

$$\begin{aligned} p_x(\theta) &= \Delta x(\theta) + r_{ball}(\theta) \\ p_y(\theta) &= \Delta y(\theta) + r_{ball}(\theta) \end{aligned} \tag{3-1}$$

where $\Delta x(\theta)$ and $\Delta y(\theta)$ are the radial motion of the target ball center, P_{ball} , relative to X and Y probes. In reality, the capacitance probes are not perfectly aligned with P_{ball} as the spindle rotates (Figure 3.1).

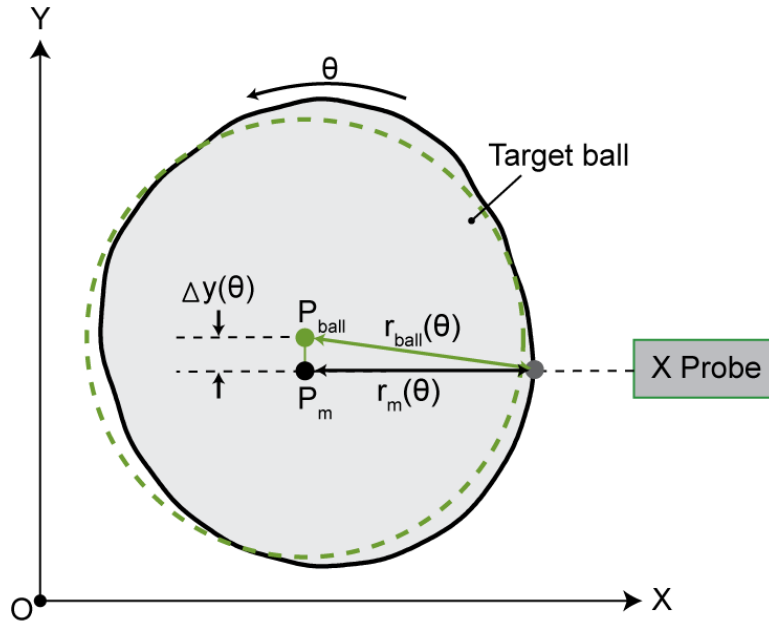


Figure 3.1. Effect of probe misalignment on measuring the motion of target ball least squares center P_{ball} .

This misalignment, $\Delta y(\theta)$, causes an error in the probe readout equal to $r_{ball}(\theta) - r_m(\theta)$ where $r_m(\theta)$ is the roundness profile measured by the probe. This error is a second order effect with a maximum value of:

$$\max |r_{ball}(\theta) - r_m(\theta)| \cong \frac{(\Delta y(\theta))^2}{2r_{ball}(\theta)} \quad (3-2)$$

which is very small due to large radius of the target ball, $r_{ball}(\theta)$, relative to the motion $y(\theta)$.

Similar analysis can be done for the probe in Y direction. Therefore, the capacitance probe measurements can be interpreted as the motion of the test ball center, P_{ball} , and the actual roundness profile of the target ball $r_{ball}(\theta)$.

3.1.2. Target ball curvature

The capacitance probes used in the experiments are calibrated by the manufacturer (Lion Precision) for flat target surfaces. A detailed investigation on effect of spherical targets on the capacitance probe measurements is given in [20]. The spherical targets give higher change in voltage read out for a given change in target displacement. In addition, a spherical target needs to be closer to the probe than the flat target to maintain the same capacitance between the probe and the target. For spindle error motion measurements, the change in the gap between the target and

the probe should be measured accurately but the absolute distance of the probe from the target is irrelevant.

The output voltage of the capacitance probe V corresponds to the inverse of measured capacitance:

$$V = K / C(x) \quad (3-3)$$

where the proportionality constant K , is determined by the probe internal circuitry. The sensitivity of the probe is defined as

$$G = \frac{dV}{dx} = K \frac{d}{dx} \left(\frac{1}{C} \right) \quad (3-4)$$

The change in capacitance (ΔC) for a given change in the gap (Δx) is different for flat and spherical targets. The sensitivity value given by the manufacturer, G , corresponds to $\frac{d}{dx} \left(\frac{1}{C} \right)$ of a flat target. Figure 3.2 shows a spherical target facing the probe. For this target, $\frac{d}{dx} \left(\frac{1}{C} \right)$ is different and as a result the sensitivity needs to be adjusted by a factor A :

$$G_{round} = AG_{flat} \quad (3-5)$$

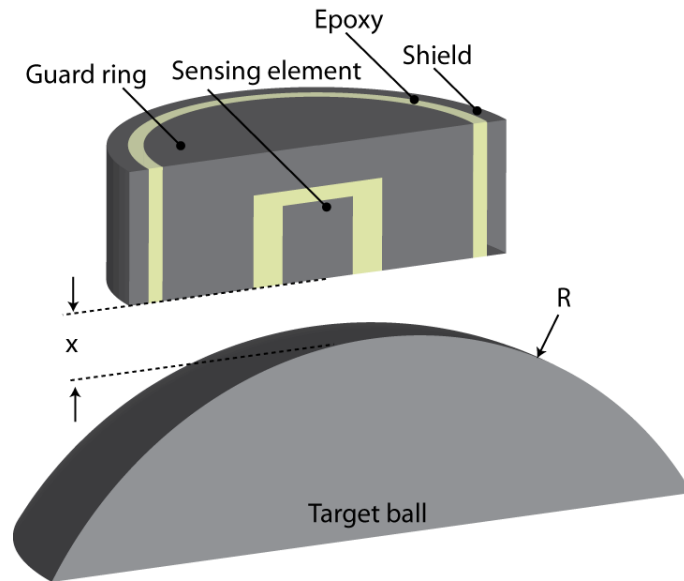


Figure 3.2. Lion precision capacitance probe against a spherical target.

To find the adjusting factor A , first step is to find the relationship between the inverse capacitance and the gap distance for both a flat target and the round target. Two methods, numerical analysis in MATLAB, and finite element analysis in FEMM, have been utilized to

calculate the capacitance sensed by the probe at different distances from the target. Both methods agree with each other while the numerical method is much faster to compute. By reducing the mesh size, finite element results converge to numerical method results. Figure 3.3 and Figure 3.4 show the results of simulation for two types of probes: C2-A with 50- μm stroke and $G = 0.400 \text{ V}/\mu\text{m}$ sensitivity, and C5-D with 10- μm stroke and $G = 2.000 \text{ V}/\mu\text{m}$ sensitivity.

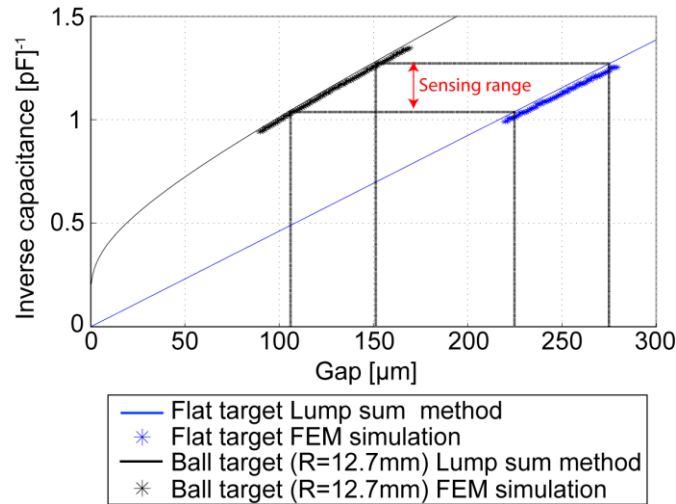


Figure 3.3. Effect of a spherical target on the sensed capacitance of C2-A probe (50- μm stroke).

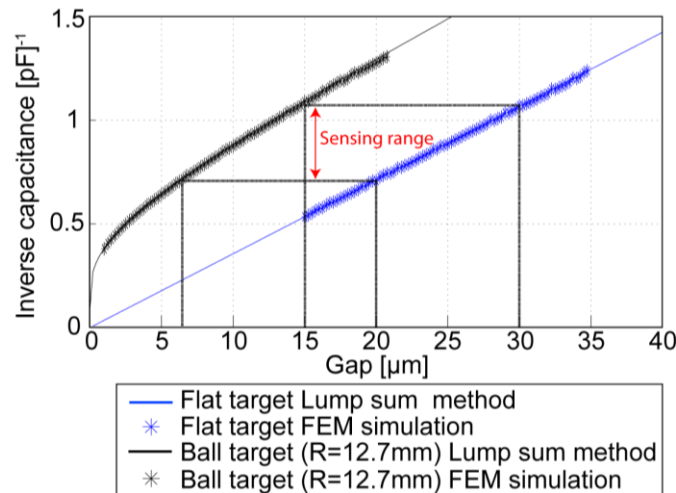


Figure 3.4. Effect of a spherical target on the sensed capacitance of C5-D probe (10- μm stroke).

Above plots show that with a round target, the gap corresponding to the sensing range is smaller and closer to the sensing electrode. In addition, the slope of the plots indicate that to get the same change in inverse capacitance $\Delta(1/C)$ (and output voltage ΔV), the round target needs to move less than a flat target.

Next, for the capacitance values within the sensing range of the probe, the corresponding gap distances from the round target is plotted against the corresponding gap distances from a flat

target (Figure 3.5 and Figure 3.6). The slope of the least squares line through data points is the adjusting factor A which will be applied to the measurements.

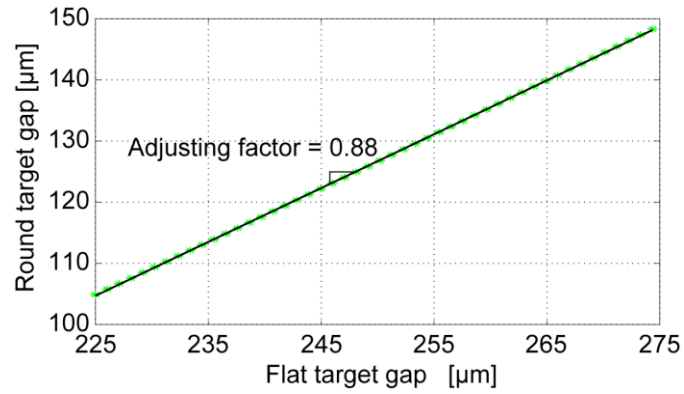


Figure 3.5. Finding adjustment factor for C2-A probe (50- μm stroke).

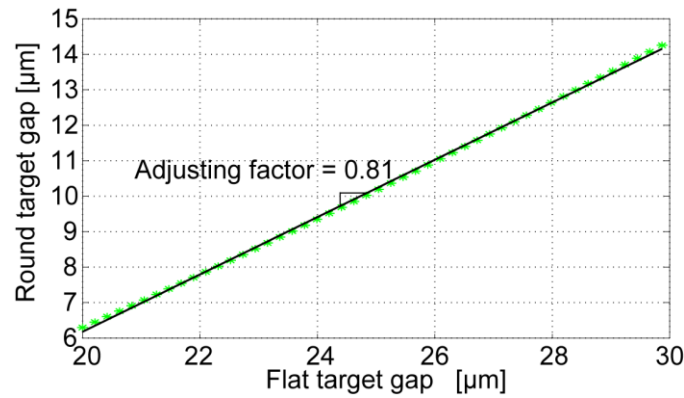


Figure 3.6. Finding adjustment factor for C5-D probe (10- μm stroke).

3.1.3. Aliasing

Digital processing of the spindle motion measurements require that the sampled points from the probe be equally spaced in spatial domain. Figure 3.7 shows an ideal setup for testing axis of rotation.

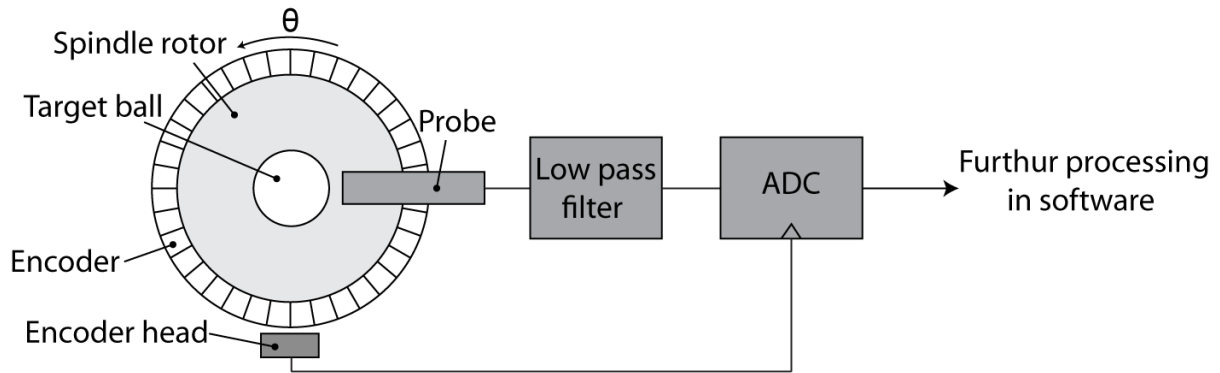


Figure 3.7. Typical data acquisition setup.

In this setup, capacitance probe signal is sampled at every count of encoder signal. This ensures that samples correspond to rotary positions which are equally spaced. Lion Precision TMP190 drive employs this type of configuration. Using this setup, the highest harmonic of spindle motion which can be captured is half the number of encoder counts per revolution (Nyquist frequency). To avoid aliasing, harmonics which are higher than the Nyquist frequency are removed using a low pass filter before sampling the signal.

Figure 3.8 shows the setup used for the experiments presented in this thesis. Lion Precision CPL190 drive with a bandwidth of 15 kHz is used for the capacitance probes. Both the encoder signals as well as the capacitance probe signals are captured using dSPACE 1103 digital control system. The probe signals are then interpolated in software to get measurements at equally spaced angular intervals. Two issues need to be addressed here:

- 1) The error of the interpolation depends on how constant the spindle speed is over one revolution.
- 2) The Nyquist frequency is half the clock frequency of the dSPACE 1103 (given that the interpolation does not down sample the probe signal). Aliasing will happen if two conditions are met: the bandwidth of the low pass filter is lower than the Nyquist frequency, and the probe signal contain harmonics higher than the Nyquist frequency.

In the experiments presented, the interpolation error is negligible due to relatively constant spindle speed over each revolution. In addition, the spindle's error motion harmonics above the Nyquist frequency are negligible. This is true over the whole tested speed range; therefore, the effect of aliasing can be neglected.

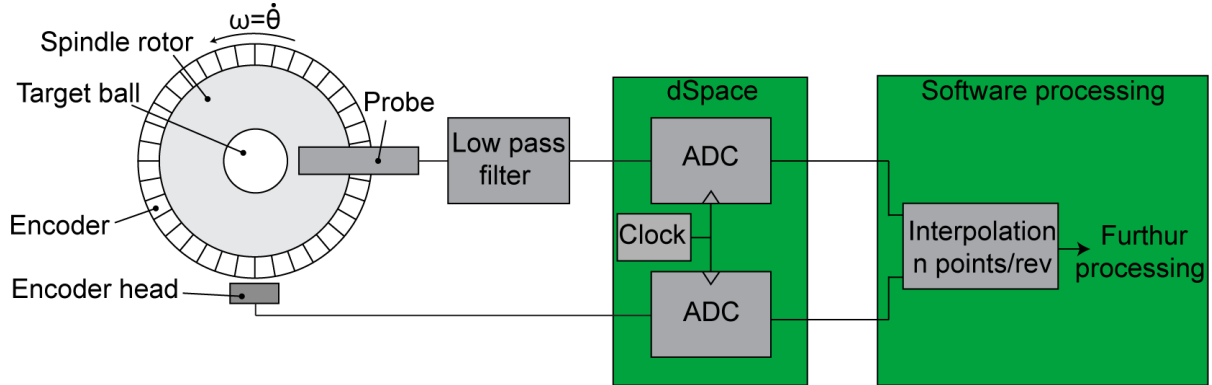


Figure 3.8. Data acquisition setup used in the experiments.

3.1.4. Indexing error

The new 2D method requires the measurement of the test point motion be in orthogonal directions. As shown in Figure 3.9, indexing error happens when any of the probes is placed with an offset to the corresponding axis. With an offset angle φ , the measurements become

$$x_m(\theta) = x_p(\theta) \quad (3-6)$$

$$y_m(\theta) = y_p(\theta)\cos(\varphi) - x_p(\theta)\sin(\varphi) \quad (3-7)$$

In the frequency domain, the measurements are

$$X_m(k) = X_p(k) \quad (3-8)$$

$$Y_m(k) = Y_p(k)\cos(\varphi) - X_p(k)\sin(\varphi) \quad (3-9)$$

The 2D motion measurement will be

$$V_m(k) = X_m(k) + jY_m(k) \quad (3-10)$$

and the error in measurement is

$$|E(k)| = |V_m(k) - V_p(k)| \quad (3-11)$$

where

$$V_p(k) = X_p(k) + jY_p(k) \quad (3-12)$$

For small angular offset, the error can be approximated as

$$|E(k)| \cong |X_p(k)\phi| \quad (3-13)$$

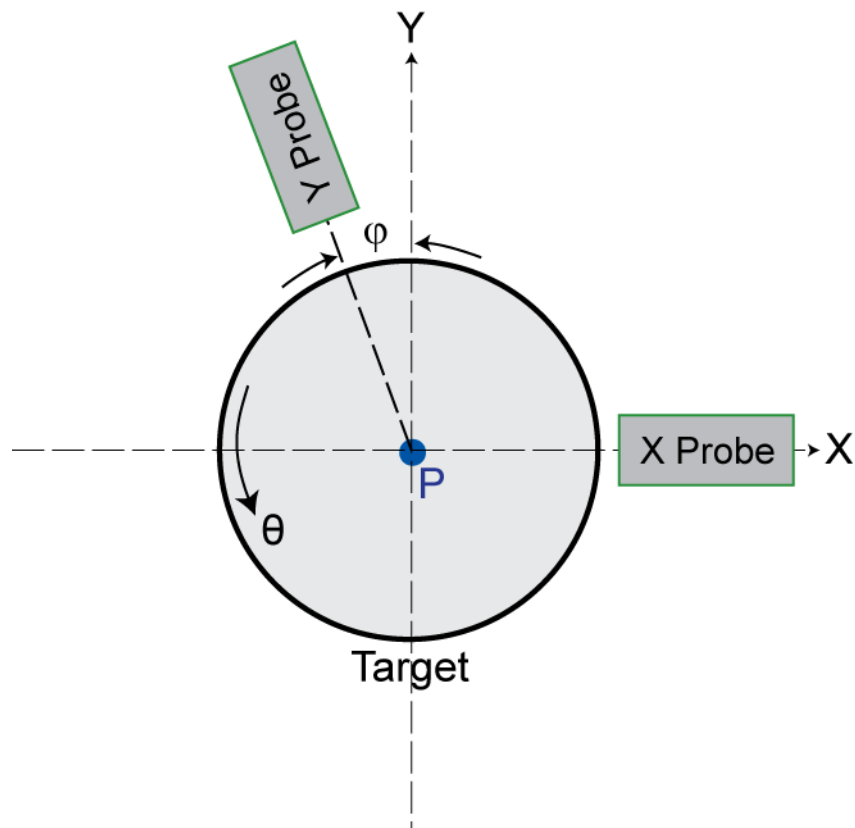


Figure 3.9. Indexing error on the spindle metrology setup.

3.2. Experiments on a ball bearing spindle

Figure 3.10 shows a 5-axis machining center with a ball bearing tool spindle. The machine work table is selected as the metrology reference frame; therefore, the measured axis of rotation error motion includes both bearing error motion and structural error motion. Two capacitance probes (10- μm stroke, part number C5-D by Lion Precision), are clamped onto the table by an L-shaped probe holder and a target ball with 10 nm roundness is mounted on the tool spindle rotor. The probes measure the relative motion between the target ball and the machine table in X and Y directions in the plane coincident with the target ball center. These probes have a nominal sensitivity of 0.5 $\mu\text{m}/\text{V}$ for a flat target surface. However, the actual sensitivity is corrected to 0.405 $\mu\text{m}/\text{V}$ due to the ball radius of 12.7 mm. The spindle's built-in encoder is used to measure the spindle rotary position. This rotary encoder outputs analog quadrature signals at 192 lines per

revolution. A dSPACE 1103 digital control system is used to collect data. Table 3-1 summarizes the specifications of the measurement system.

Table 3-1. Sensors and data acquisition system.

Sensor	Sensitivity	Data acquisition	Resolution
Y probe	0.405 $\mu\text{m}/\text{V}$	+/- 10V, 16 bit, ADC	0.2 nm
X probe	0.405 $\mu\text{m}/\text{V}$	+/- 10V, 16 bit, ADC	0.2 nm
Rotary encoder	192 line/rev	256-fold interpolation	0.01 deg

All sensor signals are sampled at 10 kHz. In order to facilitate the angle domain processing of the radial motion data, these signals are interpolated at equally spaced rotary angles to 500 samples per revolution, which is equivalent to 0.72 degree per sample. Since the target ball roundness (10 nm) is much less than the micron level radial error motion of the spindle, the ball out-of-roundness is neglected. In the following sections, the spindle error motion is evaluated at two constant speeds of 1000 and 4000 rpm using the 2D method. In addition, the change in error motion across speed from 100 up to 4500 rpm is presented.

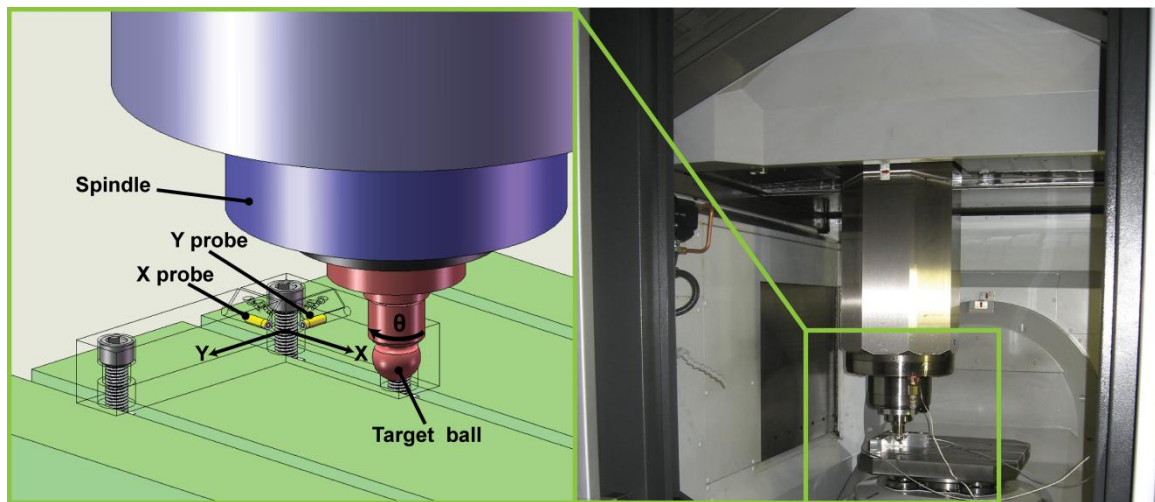


Figure 3.10. Radial error motion measurement setup of the ball bearing spindle.

3.2.1. Experimental results at 1000 rpm

3.2.1.1. Test ball motion measurement

After running the spindle at 1000 rpm for 30 minutes, 500 revolutions of data are collected. Figure 3.11 shows 20 revolutions overlaid on top of each other for both X and Y directions. From revolution to revolution, some of the motion components consistently repeat and are

referred as synchronous error motion. The rest of the motion components are referred as asynchronous error motion.

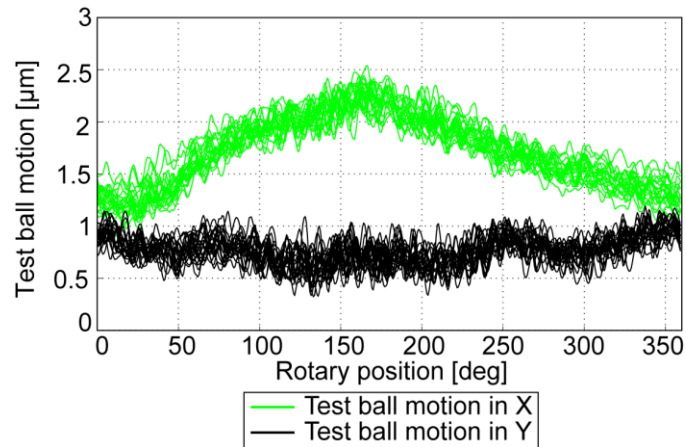
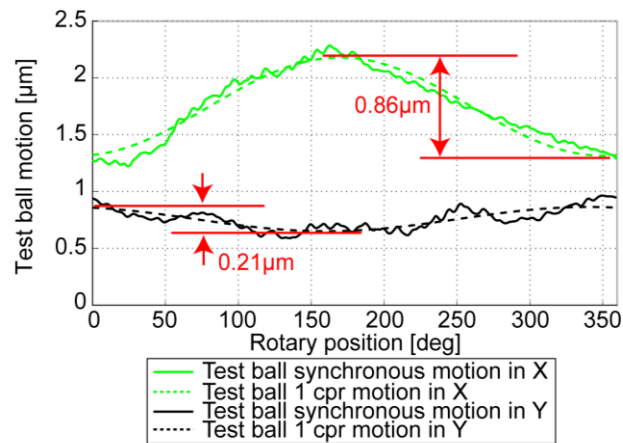
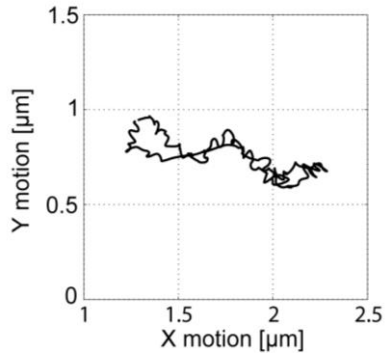


Figure 3.11. Test ball motion measurement data over 20 revolutions at 1000 rpm.

Averaging the captured 500 revolutions gives the test ball synchronous motion shown in Figure 3.12. The first harmonic components of X and Y motion are also plotted in the dashed lines. X motion has a first harmonic component with peak-valley (p-v) amplitude of $0.86\ \mu\text{m}$. In comparison, Y motion has a first harmonic component with much smaller p-v amplitude of $0.21\ \mu\text{m}$. This indicates that the spindle has fundamental radial error motion at 1000 rpm.



(a) X and Y motion versus rotary angle.



(b) Y versus X motion trace plot.

Figure 3.12. Test ball synchronous 2D motion on the ball bearing spindle at 1000 rpm.

By combining the X and Y motion into complex values, Fourier coefficients of the test ball 2D synchronous radial motion can be calculated, as shown in Figure 3.13. The DC component ($k=0$) is related to the probe installation and offset settings, and doesn't represent spindle motion performance. Additionally, the $k=1$ component is related to the test ball installation eccentricity and is not part of spindle error motion. The $k=-1$ component with the amplitude of $0.21\ \mu\text{m}$ represents the fundamental spindle radial error motion.

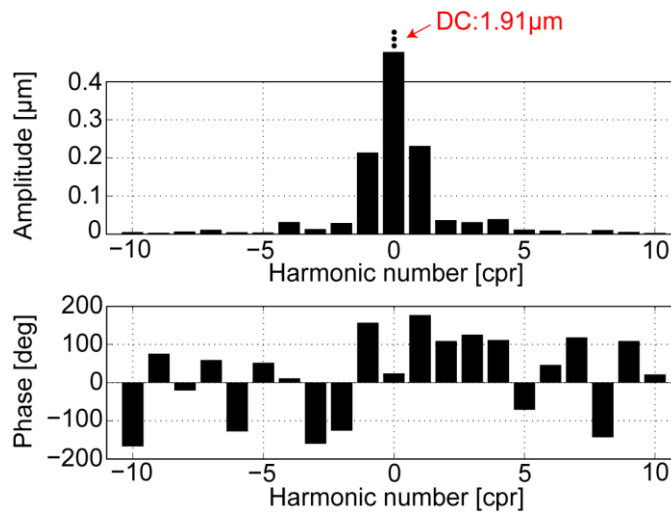


Figure 3.13. Fourier coefficients of the test ball 2D motion at 1000 rpm.

The difference between the test ball total motion in Figure 3.11 and its synchronous component in Figure 3.12 is the test ball asynchronous motion. Figure 3.14 shows the asynchronous motion over 4 revolutions with p-v amplitude of less than $0.7\ \mu\text{m}$ in both X and Y directions.

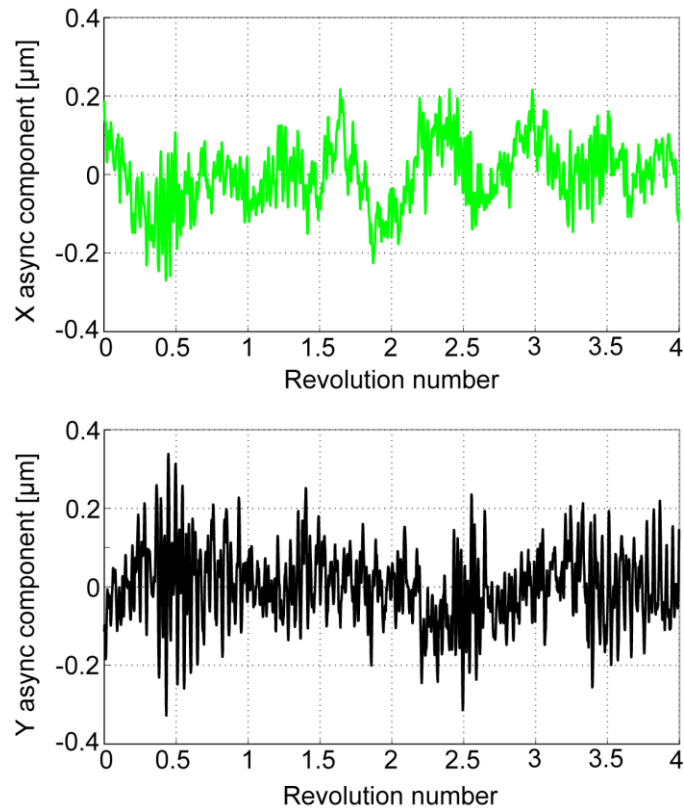
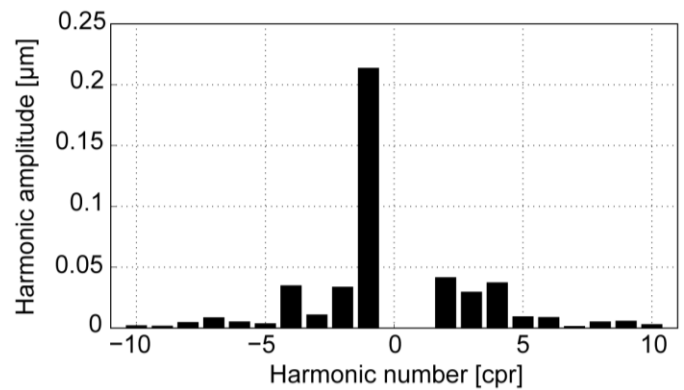


Figure 3.14. The test ball asynchronous motion in X and Y directions at 1000 rpm.

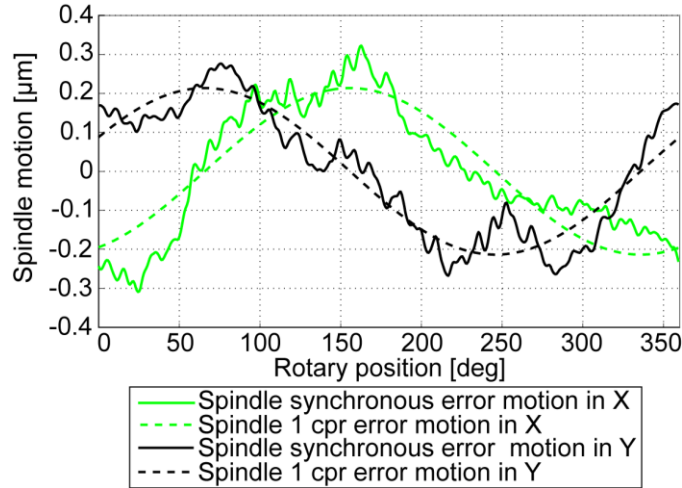
3.2.1.2. Spindle 2D radial error motion

By eliminating the $k = 0$ and $k = 1$ components from Figure 3.13, the Fourier coefficients of the axis of rotation 2D radial error motion are obtained as shown in Figure 3.15(a). Further, by applying the inverse Fourier transform on these Fourier coefficients, the spindle 2D radial error motion in angle domain is determined as shown in Figure 3.15(b). Both X and Y components of spindle radial error motion contain the 1 cpr harmonic components as shown in the dashed lines.



k	-4	-3	-2	-1	2	3	4
$ V[k] [\mu\text{m}]$	0.04	0.01	0.03	0.21	0.04	0.03	0.04

(a) Fourier coefficients of the axis of rotation radial error motion.



(b) The axis of rotation radial error motion in the spatial domain.

Figure 3.15. The ball bearing spindle synchronous radial error motion measurement result at 1000 rpm.

3.2.1.3. Comparison with current standards

Figure 3.16 compares the error motion result using the current standard [3] and that using the 2D method in three cases: a) the error motion in X using the fixed sensitive direction method [3] and using the 2D method; b) the error motion in Y using the fixed sensitive direction method [3] and using the 2D method; c) the error motion in the rotating radial direction using the rotating sensitive direction method [3] and using the 2D method. In case (a) and (b), the radial error motion specified by the current standards is significantly different from the one calculated by the 2D method. The reason is that the fundamental radial error motion ($k = -1$) is removed in the current standard. In case (c), the difference is relatively small, as the $k = 2$ radial error motion missed from the rotating sensitive direction method is small for the tested spindle at 1000 rpm.

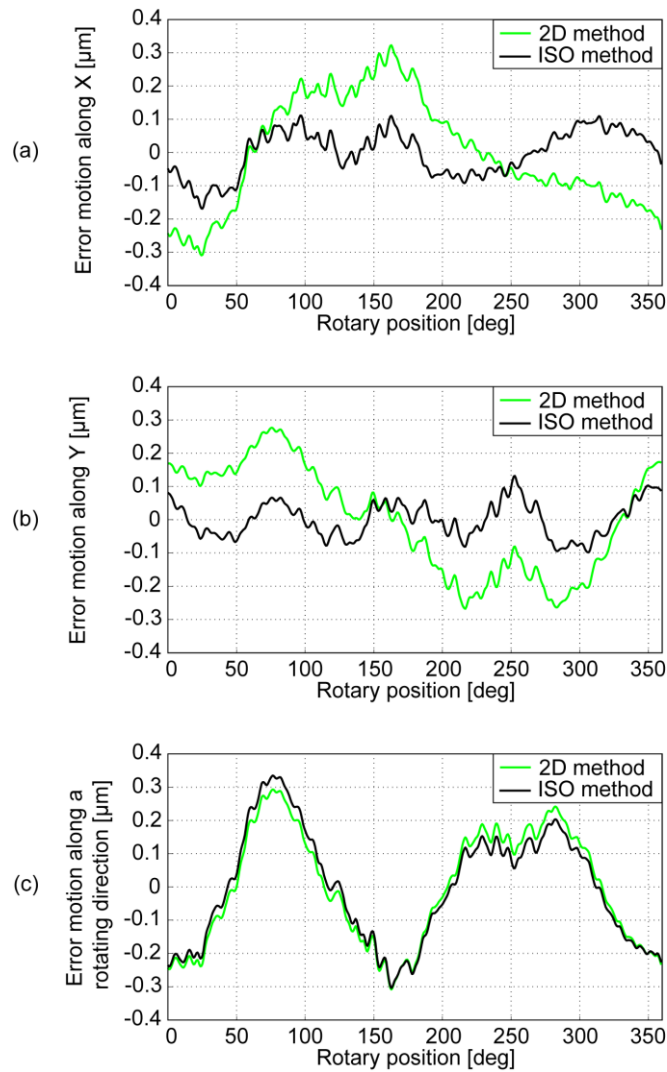


Figure 3.16. Radial error motion comparison between the current standards and the new 2D method.

3.2.2. Experimental results at 4000 rpm

3.2.2.1. Test ball motion measurement

In a similar way to the experiment at 1000 rpm, the ball-bearing spindle radial error motion is measured at 4000 rpm. The first 20 revolutions of the test ball motions measurement are overlaid on top of each other in Figure 3.17.

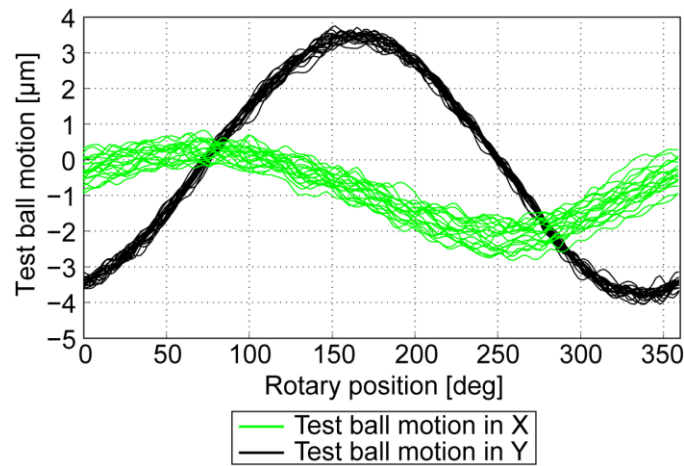
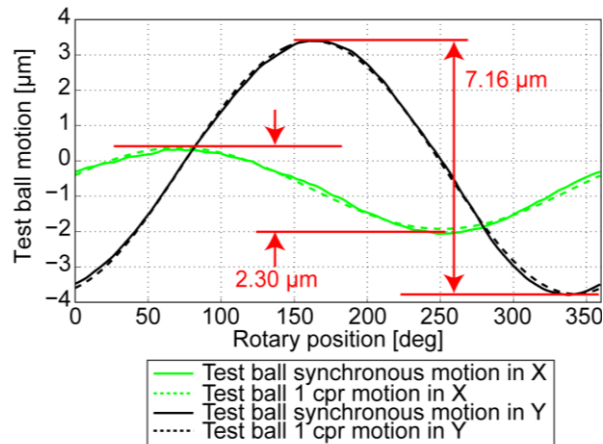
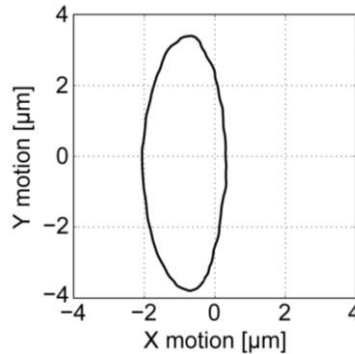


Figure 3.17. Test ball motion measurement over 20 revolutions at 4000 rpm.

Figure 3.18 shows the test ball synchronous motion. The first harmonic component in the X direction is $2.30 \mu\text{m}$ p-v, which is much smaller than $7.16 \mu\text{m}$ p-v in the Y direction. In comparison, the test results at 1000 rpm show a bigger first harmonic component in X direction than that in the Y direction. This indicates that X and Y first harmonic components vary significantly from one speed to another.



(a) X and Y motion versus rotary angle.



(b) X and Y motion versus rotary angle.

Figure 3.18. Test ball synchronous 2D motion on the ball bearing spindle at 4000 rpm.

From the X and Y motion in Figure 3.18, Fourier coefficients of the test ball 2D radial motion can be calculated, as shown in Figure 3.19. The fundamental radial error motion represented by $k = -1$ component has amplitude of $1.22 \mu\text{m}$.

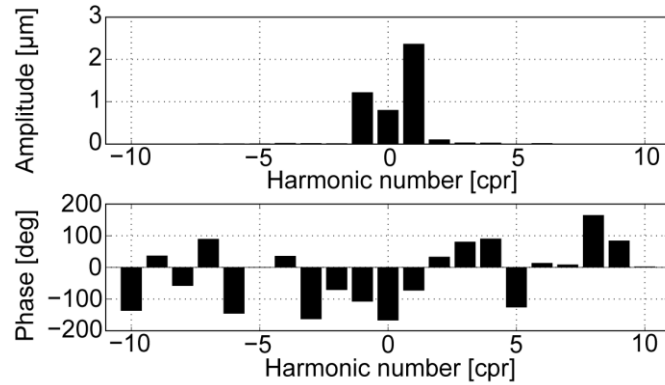


Figure 3.19. Fourier coefficients of the test ball 2D radial motion at 4000 rpm.

Figure 3.20 is the test ball asynchronous motion over 4 revolutions at 4000 rpm. The asynchronous motion is $1.2 \mu\text{m}$ p-v in X direction and $0.7 \mu\text{m}$ p-v in Y direction.

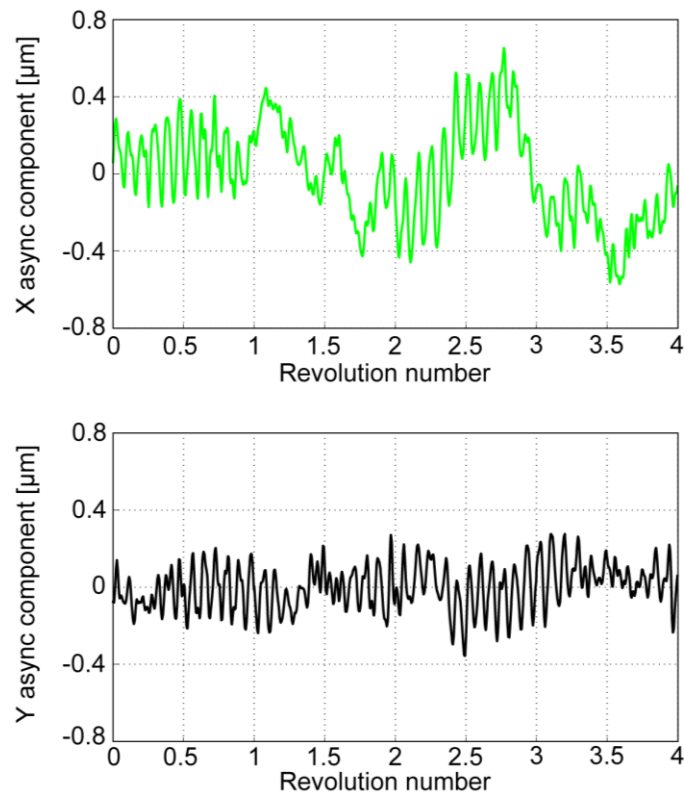
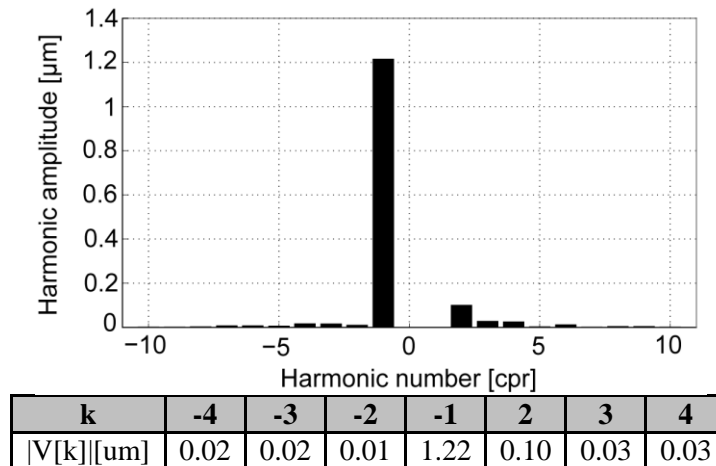


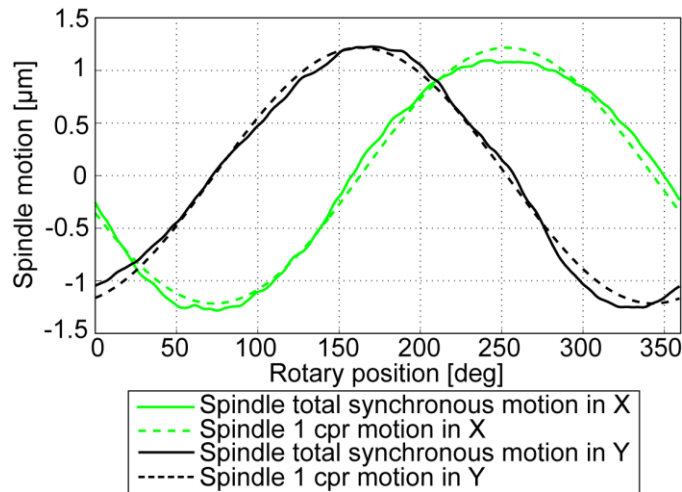
Figure 3.20. The test ball asynchronous motion in X and Y directions at 4000 rpm.

3.2.2.2. Spindle 2D radial error motion

By eliminating the $k=0$ and $k=1$ components from Figure 3.19, the Fourier coefficients of the spindle radial error motion are obtained as shown in Figure 3.21(a). Furthermore, by applying the inverse Fourier transform on these coefficients, the spindle radial error motion in both X and Y directions is found, as shown in Figure 3.21 (b). Both X and Y components of spindle radial error motion contain 1 cpr harmonic component.



(a) Fourier coefficients of the axis of rotation radial error motion.



(b) The axis of rotation radial error motion in the spatial domain.

Figure 3.21. The test ball asynchronous motion in X and Y directions at 4000 rpm.

3.2.2.3. Comparison with current standards

Figure 3.22 compares the error motion result using the current standard [3] and that using the 2D method in three cases: a) the error motion in X using the fixed sensitive direction method [3] and

using the 2D method; b) the error motion in Y using the fixed sensitive direction method [3] and using the 2D method; c) the error motion in the rotating radial direction using the rotating sensitive direction method [3] and using the 2D method. For cases (a) and (b), neglecting the fundamental radial error motion ($k = -1$) in the current standard causes a significant decrease in the error motion amplitude. For case (c), neglecting $k = 2$ radial error motion in the current standard causes a small difference.

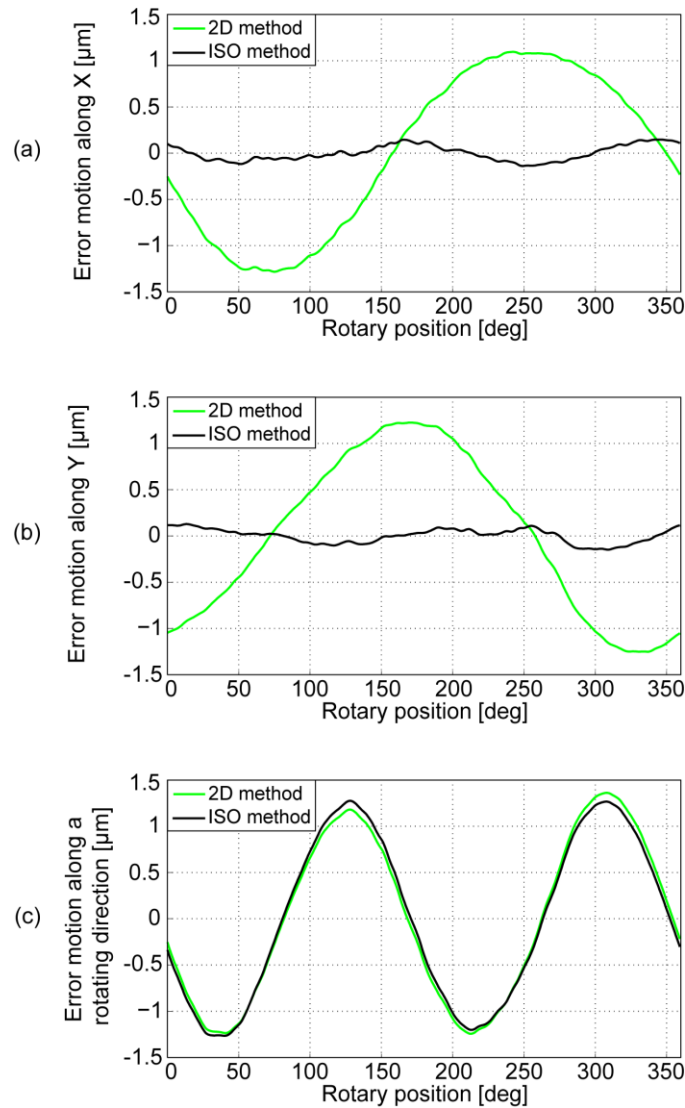


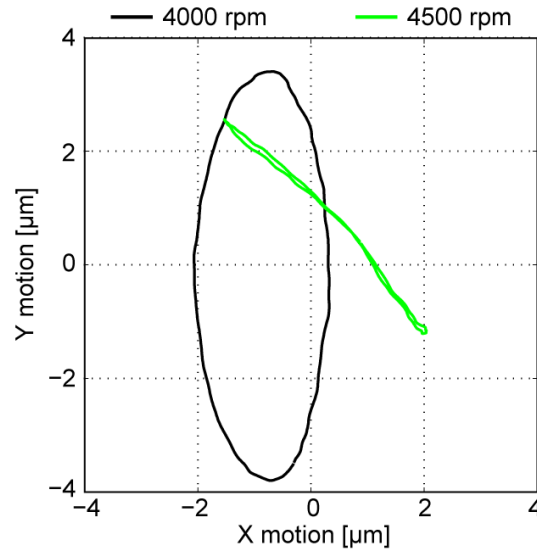
Figure 3.22. Radial error motion comparison between the current standards and the 2D method.

3.2.3. Experiments across speed

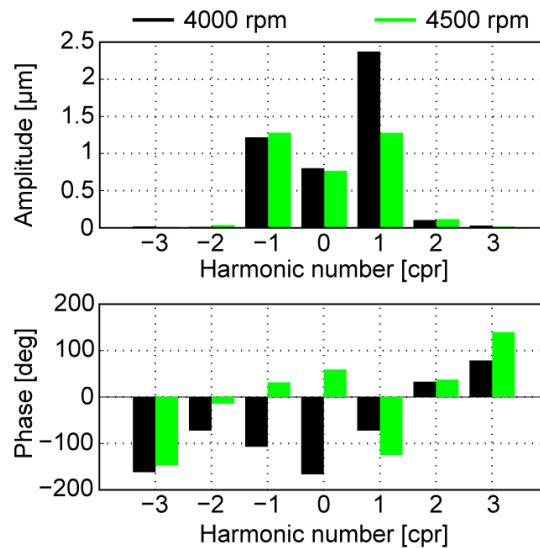
Experiments on the Mori Seiki machine is carried out at several speeds in the range of 100 to 4500 rpm. At each measured speed, 500 revolutions are used to calculate synchronous motion.

and the spindle error motion is then derived using the 2D method. This section uses the 2D method to characterize some of these measurements.

Figure 3.23(a) shows the trajectories of synchronous test ball center motion in X-Y plane at 4000 and 4500 rpm. Figure 3.23(b) shows the Fourier coefficients for the two trajectories.



a) Y versus X motion trace plot.



b) Complex Fourier coefficients of the test ball motion
Figure 3.23. Test ball motion at 4000 rpm and 4500 rpm

Using the complex Fourier coefficients, the test point trajectories can be fully characterized. The difference in magnitude of $V(+1)$ and $V(-1)$ components determine the shape of the trajectory. At 4000 rpm, the magnitude of $V(+1)$ and $V(-1)$ components are significantly different and as a result the trajectory is an ellipse. At 4500 rpm, their magnitude is very similar and as a result

the trajectory is close to a straight line. Higher order harmonics generate ripples on the motion path.

The phase of $V(+1)$ and $V(-1)$ components determine the orientation of the trajectory. At 4000 rpm, $V(+1)$ and $V(-1)$ phases are both close to -90 degree; as a result the major axis of the ellipse is along Y direction. At 4500 rpm, phase of $V(+1)$ is close to -90 deg while the phase of $V(-1)$ is close to zero; as a result the line is oriented diagonally.

At 4000 rpm the test point motion moves in the same direction of spindle rotation since $V(+1)$ component is bigger than $V(-1)$ component. At 4500 rpm, test point reverses direction since the opposite is the case.

Figure 3.24 shows the first few Fourier coefficients of the spindle 2D radial error motion versus speed. For this spindle, all coefficients vary with speed. The fundamental ($k = -1$) radial error motion amplitude is significantly larger than all other error motion components for all the measured speeds. The very large fundamental radial error motion ($k = -1$) around 4000 rpm is mainly caused by the interaction between unbalance and axis-asymmetric supporting structure compliance which has a resonance at 70 Hz. This is discussed in more detail in section 4.6.1.

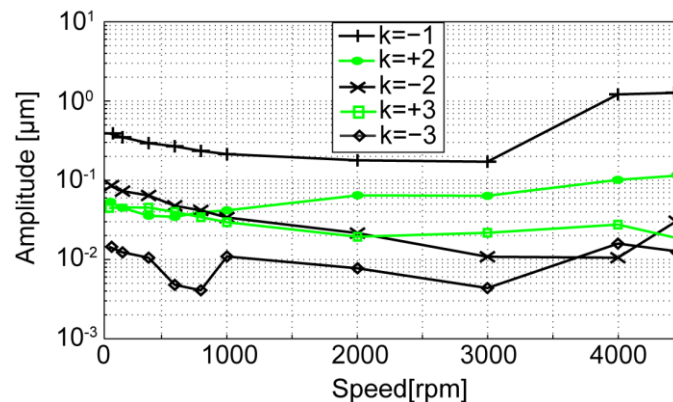


Figure 3.24. Spindle 2D radial error motion Fourier coefficients versus speed.

The $k = 1$ Fourier coefficient is plotted versus speeds in Figure 3.25.

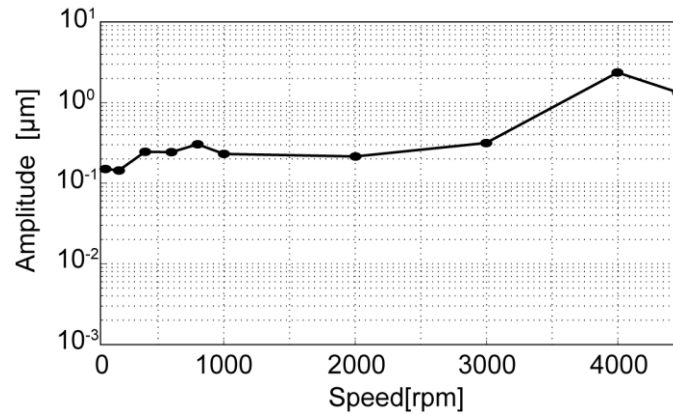


Figure 3.25. The change of axis of rotation position relative to the test ball center, $V_p(+1)$.

Although $V(+1)$ component is not part of the spindle error motion, it reflects the test ball center offset from the spindle axis of rotation. The variation of the $k = 1$ component reflects the shift of the axis of rotation inside the spindle rotor. The test ball has not been moved during the whole test but the following two factors cause the change in $V(+1)$ component:

- 1) Change of test point due to motion of the axis average line. At each speed, the new test point has a different location relative to rotation center and therefore different $V(+1)$ component.
- 2) Change of axis of rotation on the rotor which affects both the spindle error motion and $V(+1)$ component of the test point.

3.3. Experiments on an aerostatic bearing spindle

Figure 3.26 shows the experimental setups used to measure the radial error motion of an aerostatic bearing spindle (10R Block-Head by Professional Instruments). Three independent setups are used to measure the axis of rotation radial error motion at the same axial location:

- a) The ball-probe measurement setup where a 50- μm stroke capacitance probe (model number: C2-A by Lion Precision) labeled as P3 is used to sequentially measure the radial motion of a target ball (20 nm out-of-roundness, 25.4 mm diameter) in two orthogonal directions;

- b) The ring-probe measurement setup where two 10- μm stroke capacitance probes (model number: C5-D by Lion Precision) labeled as P1 and P2 are used to simultaneously measure the radial motion of an encoder scale ring (209-mm diameter) in two orthogonal directions. This is done at the same axial location as the target ball's equator.
- c) The encoder measurement setup where four equally spaced encoder heads (model number: Heidenhain 4282C) H1, H2, H3, and H4 are used to measure the spindle encoder rotary position. The spindle radial error motion is then derived from calibrated error map of the four encoder heads.

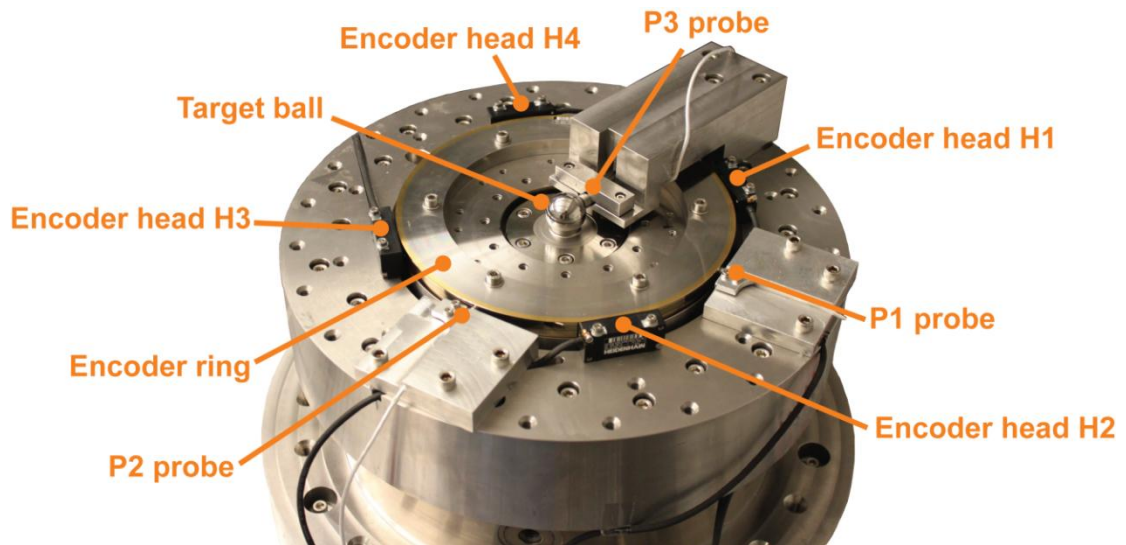


Figure 3.26. Aerostatic bearing spindle test setups.

Table 3-2 summarizes the specifications of the used instruments. P3 probe has a nominal sensitivity of 2.5 $\mu\text{m}/\text{V}$ for a flat target surface. However, the actual sensitivity is corrected to 2.2 $\mu\text{m}/\text{V}$ due to the ball radius of 12.7 mm. The probes P1 and P2 has a nominal sensitivity of 0.5 $\mu\text{m}/\text{V}$ for a flat target surface, and this number is left uncorrected as the target ring radius is much larger than the probe sensing area. The capacitance probe output signals are collected by a dSPACE 1103 digital control system at 10 kHz. This data is then spatially interpolated at 0.36 degree sample intervals to facilitate the angle domain processing. Customized time-counting electronics capture the encoder signals for error map calibration [21].

Table 3-2. Sensors and data acquisition system.

Sensor	Sensitivity	Data acquisition	Effective resolution
P3	2.2 $\mu\text{m}/\text{V}$	+/- 10V, 16 bit, ADC	0.7 nm
P1, P2	0.5 $\mu\text{m}/\text{V}$	+/- 10V, 16 bit, ADC	0.2 nm
H1, H2, H3, H4	32768 line/rev	600 MHz time capture	<2 nm at 200rpm

In the next three sections, the radial error motion measurement from each setup is presented. The comparison of results from the three setups is discussed afterwards.

3.3.1. Radial error motion measurements using the ball-probe setup

3.3.1.1. Measurement procedures and theories

Figure 3.27 shows the four steps used to measure the radial motion of the target ball in the ball-probe setup. In step (i), P3 probe is installed in the X_B direction. The probe measurement result is the combination of the ball out-of-roundness, $R_B(\theta)$, and the test ball radial error motion,

$x_B(\theta)$, in the X_B direction:

$$m_i(\theta) = R_B(\theta) + x_B(\theta) \quad (3-14)$$

For step (ii), the test ball installation is the same as step (i), but probe P3 is installed in the Y_B direction. The measurement becomes:

$$m_{ii}(\theta) = R_B(\theta - \pi / 2) + y_B(\theta) \quad (3-15)$$

where $y_B(\theta)$ is the test ball motion in direction Y_B . Step (iii) is a standard Donaldson's reversal procedure [7] with respect to step (i). The probe is moved to the direction opposite of X_B , and the ball is rotated 180 degree relative to the spindle rotor, resulting in the measurement $m_{iii}(\theta)$:

$$m_{iii}(\theta) = R_B(\theta) - x_B(\theta) \quad (3-16)$$

Simlary, step (iv) is a standard Donaldson's reversal procedure [7] with respect to step (ii). The probe is moved to the direction opposite of Y_B , and the ball installation is the same as step (iii), resulting in the measurement $m_{iv}(\theta)$:

$$m_{iii}(\theta) = R_B(\theta - \pi / 2) - y_B(\theta) \quad (3-17)$$

The test ball out-of-roundness can be derived from the measurements in the X direction as follows

$$R_B(\theta) = \frac{1}{2}(m_i(\theta) + m_{iii}(\theta)) \quad (3-18)$$

Alternatively, the measurements in the Y direction can be used to derive the ball out-of-roundness:

$$R_B(\theta - \pi / 2) = \frac{1}{2}(m_{ii}(\theta) + m_{iv}(\theta)) \quad (3-19)$$

Note that in Eq. (3-18) and (3-19), the DC and fundamental components need to be removed from the measurements as there is no once-per-revolution out-of-roundness. Further, the test ball radial motion can be calculated:

$$x_B(\theta) = m_i(\theta) - R_B(\theta) \quad (3-20)$$

$$y_B(\theta) = m_{ii}(\theta) - R_B(\theta - \pi/2) \quad (3-21)$$

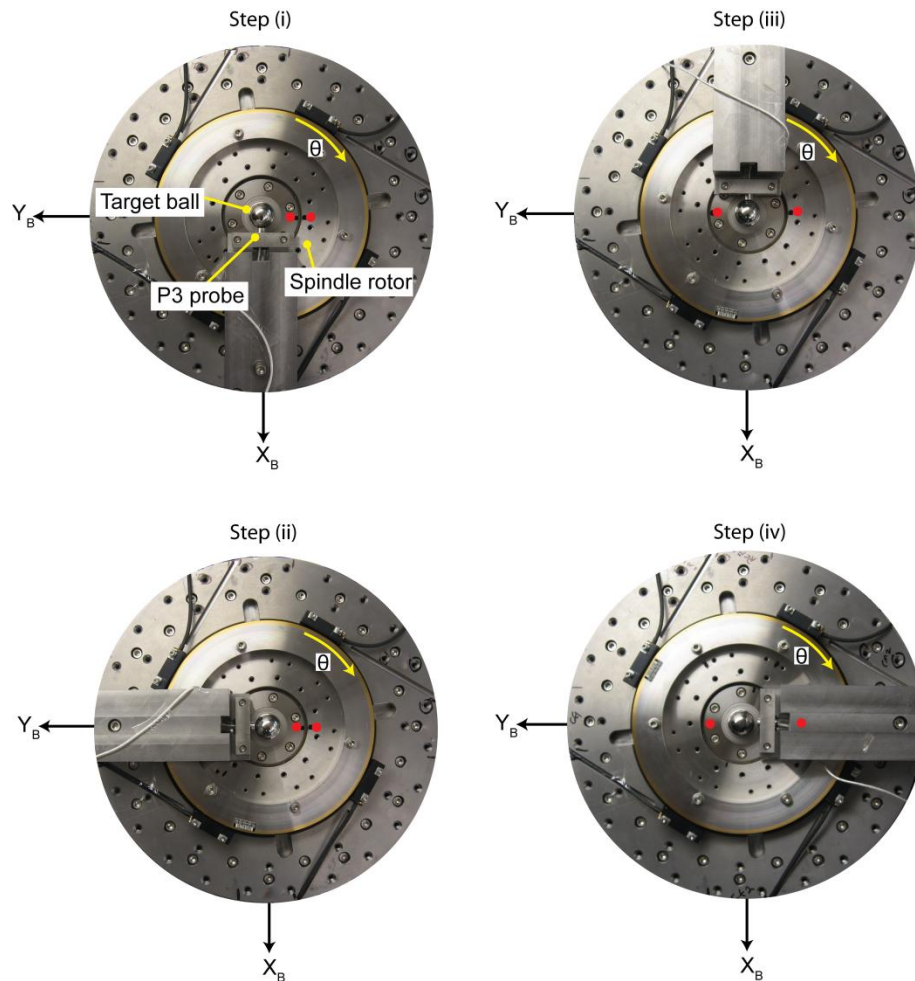


Figure 3.27. Four steps in spindle radial error motion test using setup (a).

3.3.1.2. Experimental results at 400 rpm

In Figure 3.28, the first 20 revolutions of the probe measurement at 400 rpm are overlaid.

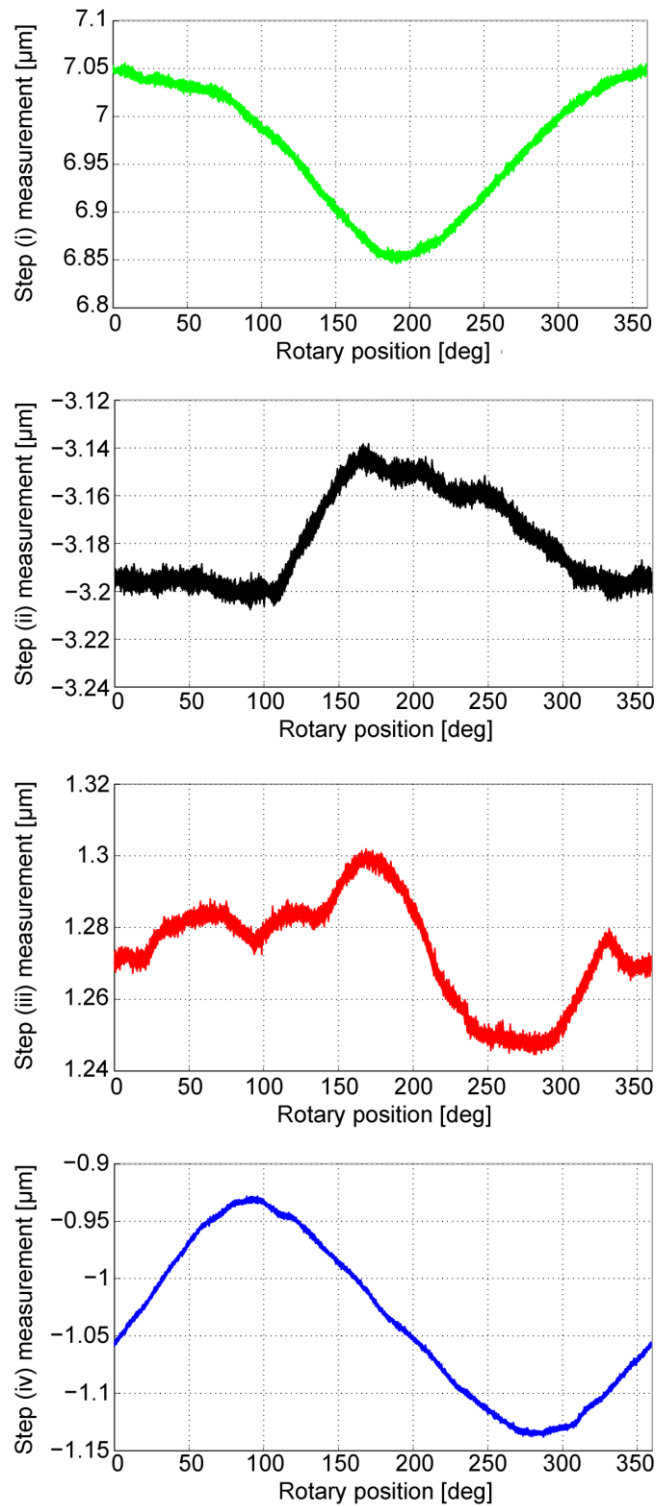


Figure 3.28. Probe measurement results at 400 rpm from the four steps. 20 revolutions are overlaid.

Figure 3.29 shows the synchronous component of the measurements obtained by averaging 500 revolutions at 400 rpm.

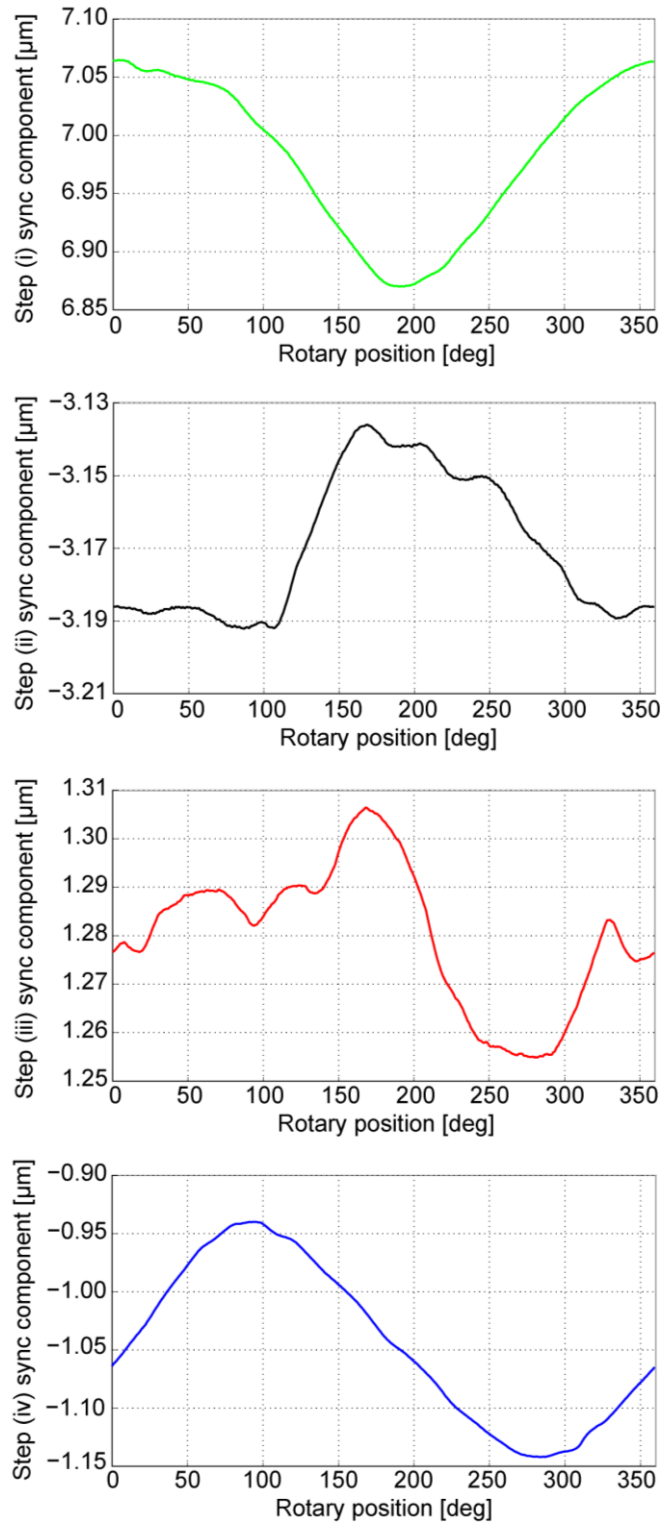


Figure 3.29. Synchronous component of the measurements from the four steps at 400 rpm.

Figure 3.30 shows the asynchronous component of the measurements over four revolutions at 400 rpm. The increase in structural loop vibrations seen in steps (i) and (ii) is due to the probe holder mounting.

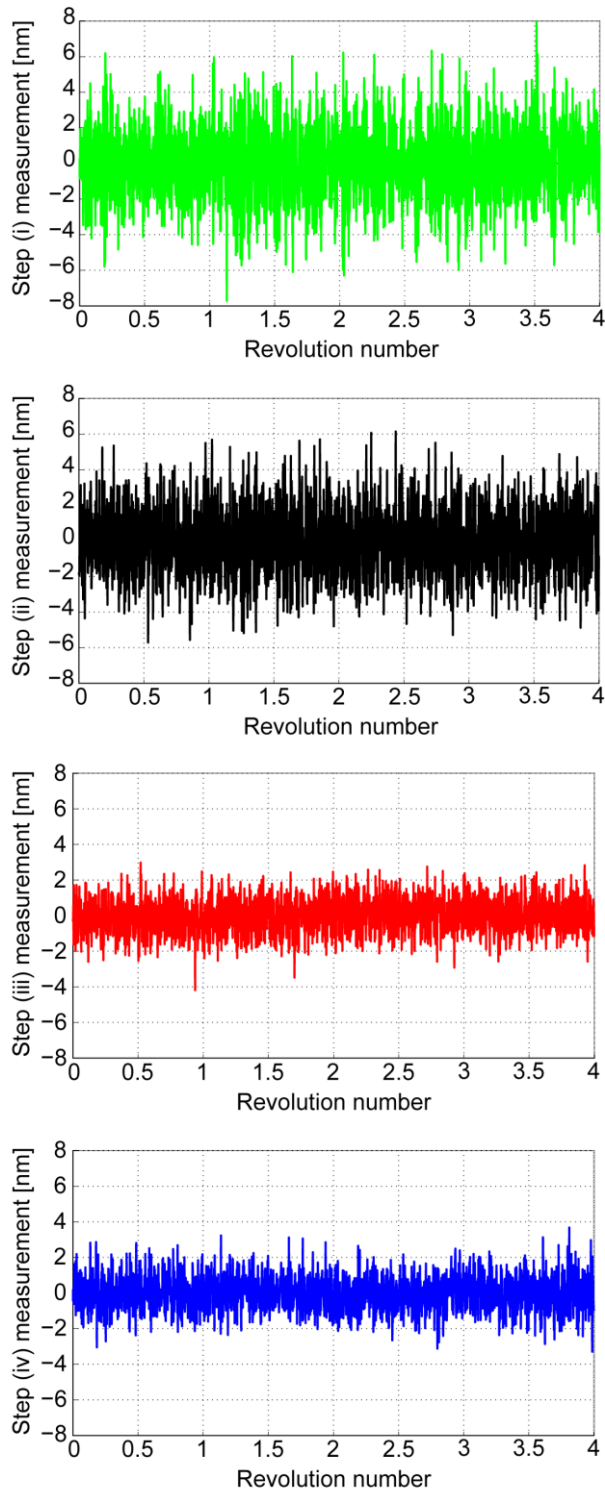


Figure 3.30. Asynchronous component of the measurements from the four steps at 400 rpm.

Figure 3.31 shows the ball roundness extracted from the synchronous components of the measurements shown in Figure 3.29. The result from steps (i) and (iii) measurement $R_{B_x}(\theta)$ is shifted by 90 degrees for better comparison with the result from steps (ii) and (iv) measurements, $R_{B_y}(\theta)$.

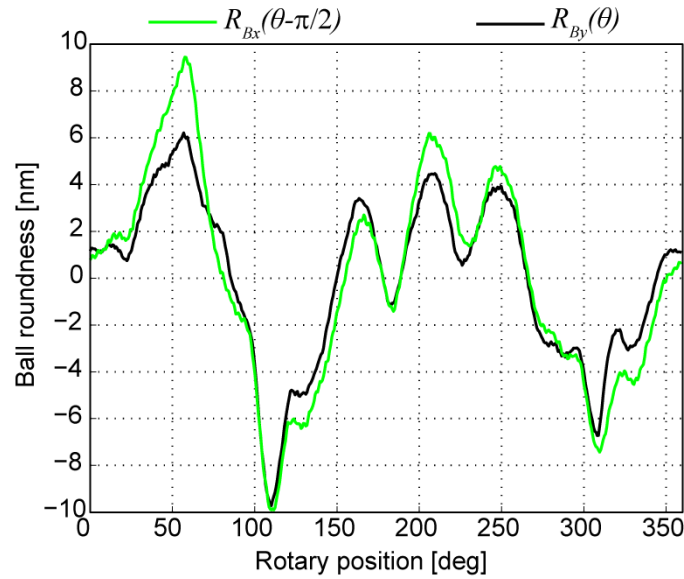


Figure 3.31. The test ball out-of-roundness.

Further, by applying Eq. (3-20) and (3-21), the test ball synchronous motion in X_B and Y_B directions are extracted and shown in Figure 3.32. From Figure 3.32, it is clear that the motion in the X_B direction has a significantly larger first harmonic component than the motion in the Y_B direction. As a result, the test ball motion path in the X-Y plane is close to a line in the X_B direction.

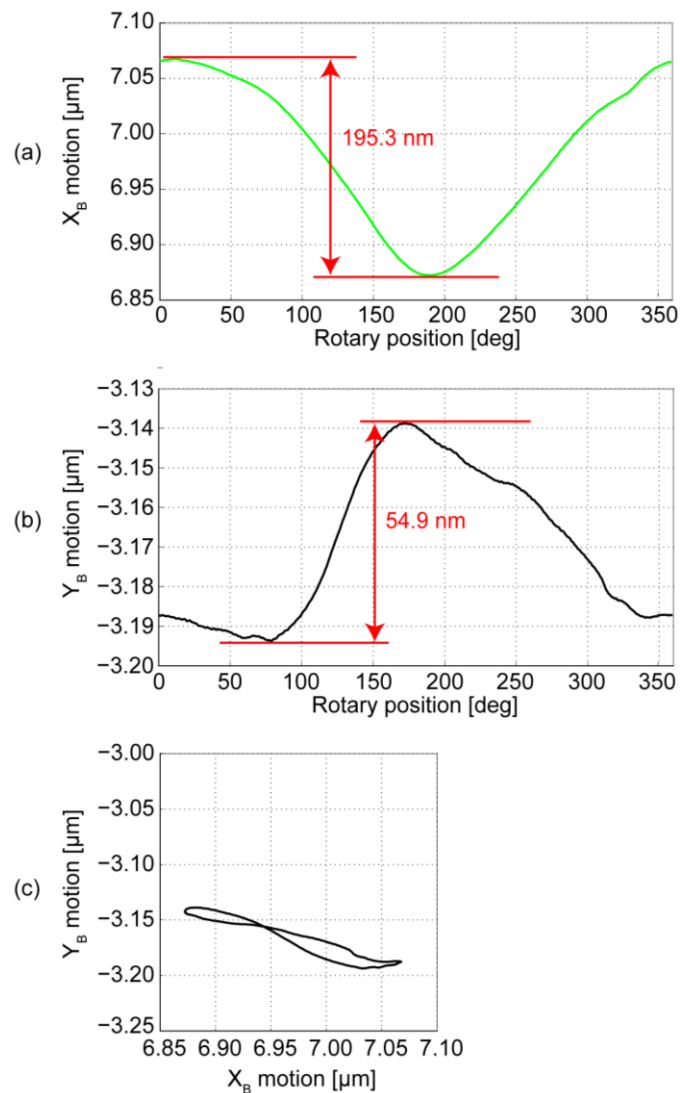


Figure 3.32. Target ball synchronous 2D motion of the aerostatic bearing spindle at 400 rpm, using the ball-probe setup. (a) X_B motion versus rotary angle. (b) Y_B motion versus rotary angle. (c) Y_B versus X_B motion trace plot.

In order to demonstrate that the fundamental radial error motion is independent from the test ball installation, a second measurement test was performed on the same spindle at 400 rpm: the target ball was installed in a different location on the spindle rotor from the previous test and the three steps are repeated for this second test. Figure 3.33 shows the test ball synchronous motion measurement result from the second test. The X_B - Y_B motion path is now close to a line in Y_B direction, which is due to large first harmonic component in the Y_B direction. Obviously, the target ball in the two tests has very different eccentricity.

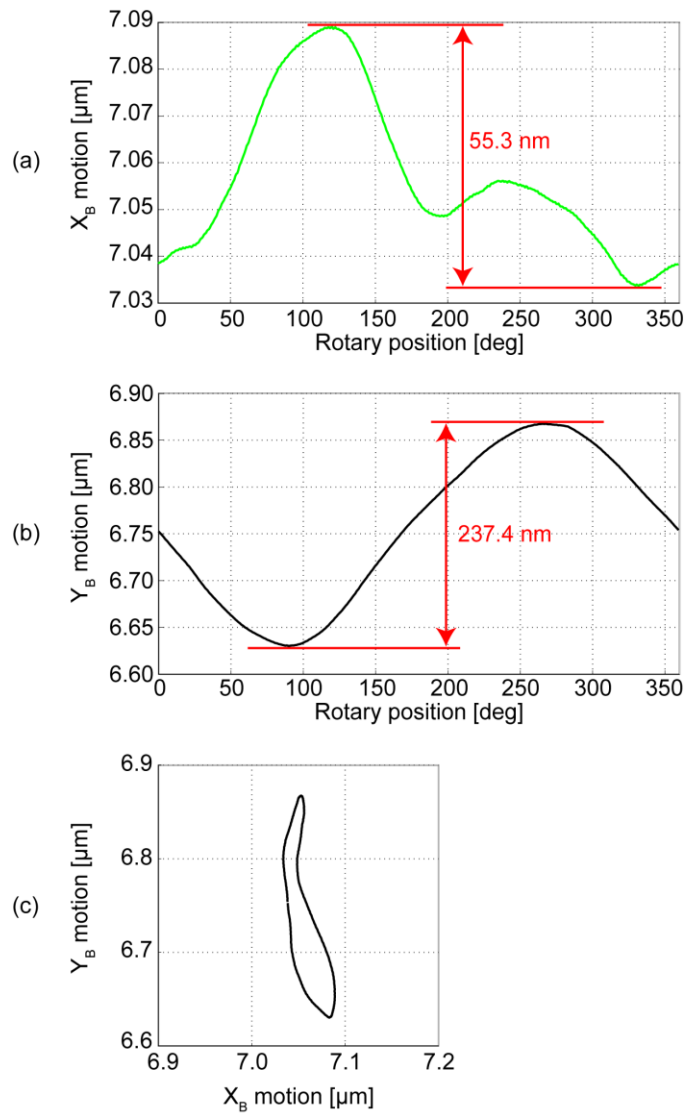
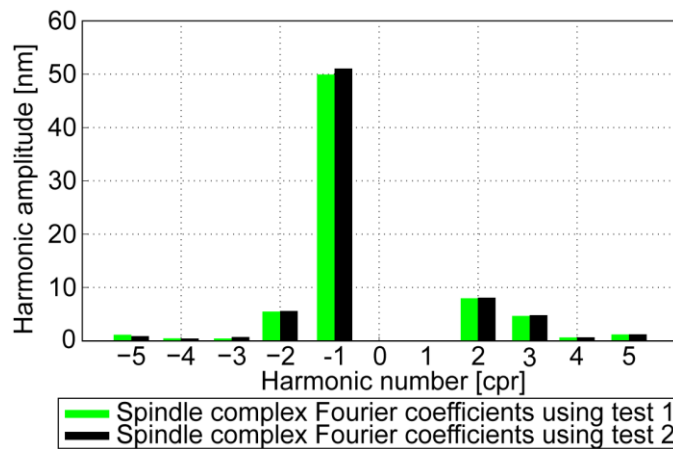
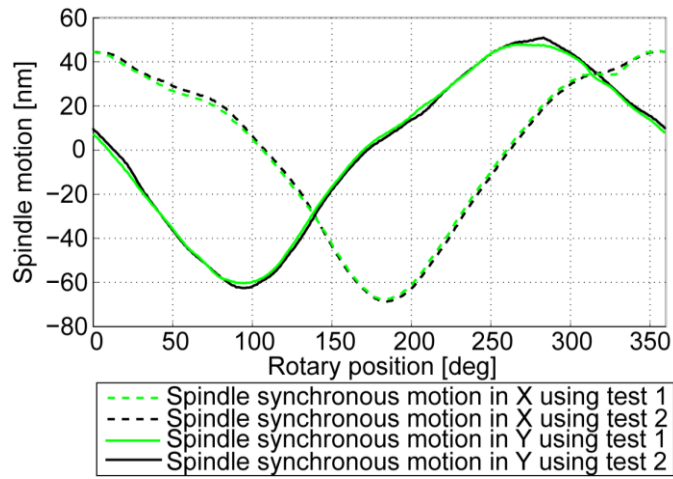


Figure 3.33. A second test of the target ball synchronous 2D motion at 400 rpm. The target ball installation location on the rotor is changed to a rotor location different from the one in Figure 3.32 results. (a) X_B motion versus rotary angle. (b) Y_B motion versus rotary angle. (c) Y_B versus X_B motion trace plot.

After applying the 2D theory in part 1 and removing the $k=+1$ harmonic component (test ball eccentricity), the spindle radial error motion in X_B and Y_B directions can be calculated for both tests, as shown in Figure 3.34(a). The results from the two tests are very consistent. Figure 3.34(b) shows the Fourier coefficients comparison of the 2D synchronous radial error motion from these two tests. The consistency confirms that the fundamental radial error motion, $V(-1)$, is not related to the test ball installation eccentricity.



Test	k	-5	-4	-3	-2	-1	2	3	4	5
1	$ V[k] $ [nm]	1.0	0.4	0.3	5.4	49.8	7.9	4.5	0.5	1.1
2	$ V[k] $ [nm]	0.8	0.3	0.6	5.5	50.9	8.0	4.7	0.6	1.1

Figure 3.34. Spindle radial error motion measurement results from two tests with very different target ball eccentricity.

3.3.1.3. Comparison with current standards

Figure 3.35 shows the comparison between radial error motion specified in the current standard [3] and the 2D radial error motion in three radial directions: the X_B direction, the Y_B direction, and the rotating direction. For the directions X_B and Y_B , the 2D method gives a significantly higher error motion than that obtained from the fixed sensitive direction method [3], which does not include $k = -1$ component. For the rotating direction, the difference in results is caused by the missing $k = 2$ component in the rotating sensitive direction method [3].

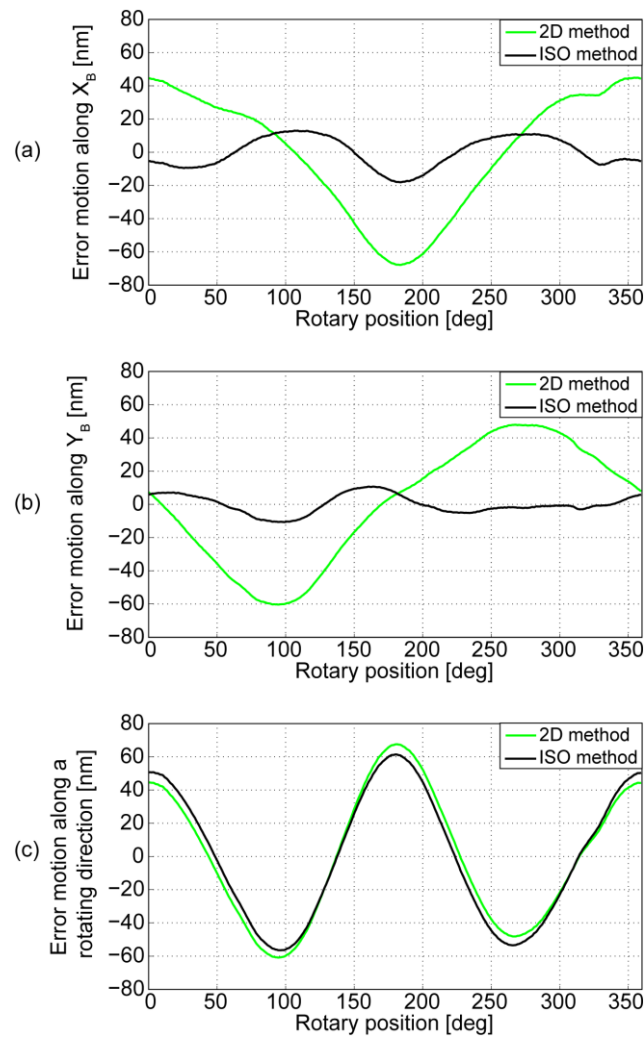


Figure 3.35. Radial error motion comparison between the current standards and the 2D method.

3.3.2. Radial error motion measurements using the ring-probe setup

In order to further confirm the existence of the fundamental radial error motion, $V(-1)$, the spindle radial error motion was measured with another independent setup: two probes, P1 and P2, simultaneously measuring against a gold plated encoder scale ring, as shown in Figure 3.36. The probes are orthogonally installed in X_R and Y_R directions.

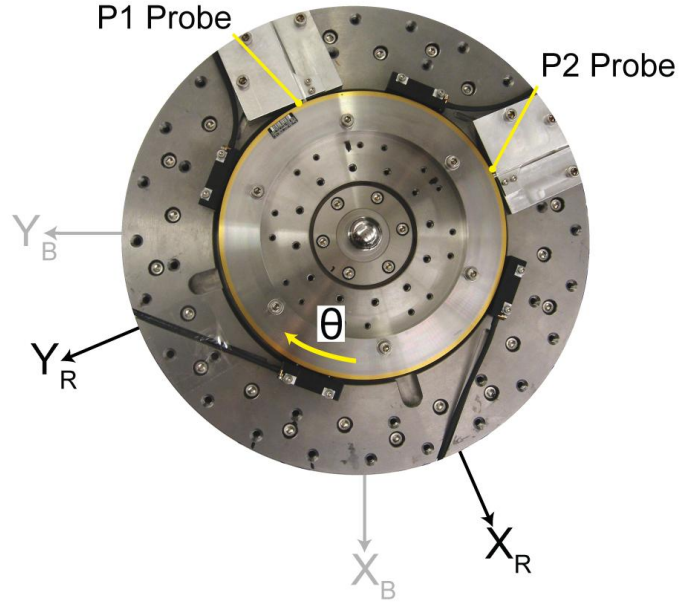


Figure 3.36. The ring-probe setup for axis of rotation radial error motion measurement.

The measurement in X_R is the combination of the ring radial motion in X_R direction, $x_R(\theta)$, and the ring out-of-roundness, $R_R(\theta)$:

$$m_x(\theta) = x_R(\theta) + R_R(\theta) \quad (3-22)$$

Similarly, the measurement in Y_R directions is

$$m_y(\theta) = y_R(\theta) + R_R(\theta - \pi/2) \quad (3-23)$$

where $y_R(\theta)$ is the ring radial motion in Y_R direction. As the ring target is much more flexible than the test ball, it is difficult to ensure the same roundness in a reversal test; therefore, the roundness is not removed from the measurement in this setup. Transferring Eq. (3-22) and (3-23) into frequency domain, the k -th Fourier coefficients of the measurement become

$$M_x(k) = X_R(k) + R_R(k) \quad (3-24)$$

$$M_y(k) = Y_R(k) + j^{-k} R_R(k)$$

where $R_R(k)$, $X_R(k)$ and $Y_R(k)$ are the k -th Fourier coefficients of $R_R(\theta)$, $x_R(\theta)$ and $y_R(\theta)$, respectively. The ring out-of-roundness can be eliminated from the measurements using the following Eq.:

$$M_x(k) - j^k M_y(k) = X_R(k) - j^k Y_R(k) \quad (3-25)$$

Particularly, for $k = -1$,

$$M_x(-1) + j M_y(-1) = X_R(-1) + j Y_R(-1) = V_R(-1) \quad (3-26)$$

where $V_R(-1)$ is the fundamental radial error motion. Therefore, the $k = -1$ component can be calculated from the ring-probe measurement without removing the ring roundness.

Figure 3.37 shows the 500 revolutions of overlaid probe measurement results at 400 rpm. By averaging the measurement, the synchronous components can be extracted as shown in Figure 3.38. The X and Y results are dominated by out-of-roundness of the ring and show a very similar pattern aside from a 90 degree phase shift. Using Eq. (3-26), the amplitude of $k = -1$ component of the 2D radial motion is calculated as $|V_R(-1)| = 50.2$ nm, which matches the two test results using ball-probe setup in Figure 3.34. Again, this confirms that $|V_R(-1)|$ is an error motion component independent of target shape and installation. The asynchronous component of the probe measurements over four revolutions is shown in Figure 3.39. These are the asynchronous radial error motions in X_R and Y_R directions plus electrical noises.

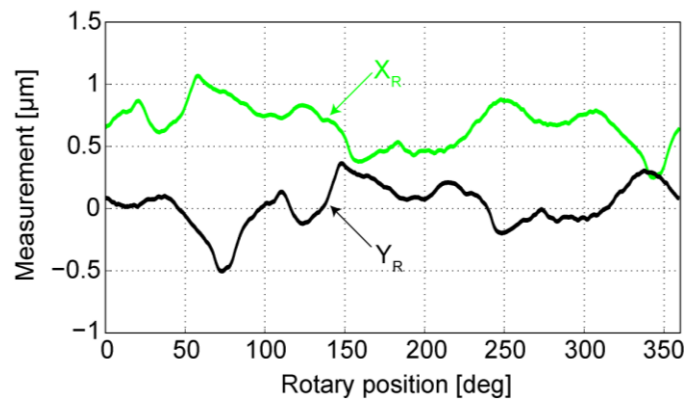


Figure 3.37. Probe measurement results at 400 rpm using the ring-probe setup. 500 revolutions are overlaid.

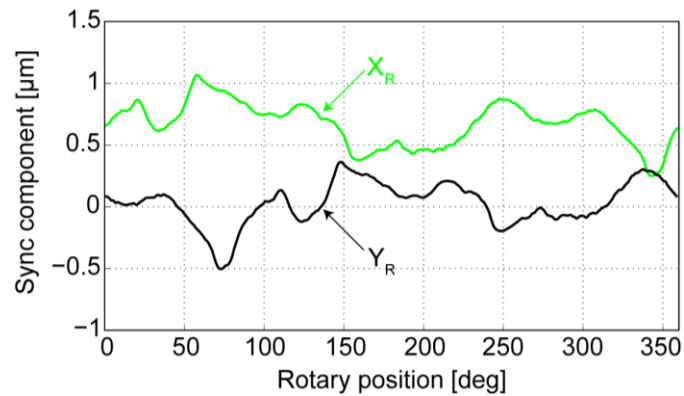


Figure 3.38. Synchronous motion of the ring-probe setup measurements.

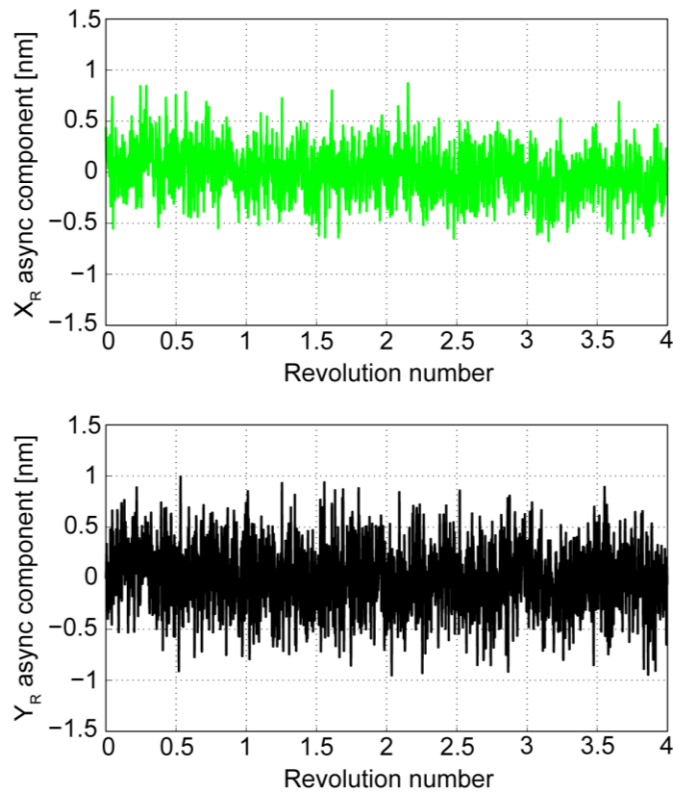


Figure 3.39. Asynchronous radial error motion results.

3.3.3. Radial error motion measurements using the four encoder head setup

Figure 3.40 shows setup (c) in top view. Four encoder heads are equally spaced around the encoder ring and are used to measure spindle rotation. Each encoder head output signal has measurement error due to ring scale grating error and radial error motion. With the self-calibration method presented in [23] and [24], the error map for each head can be calibrated.

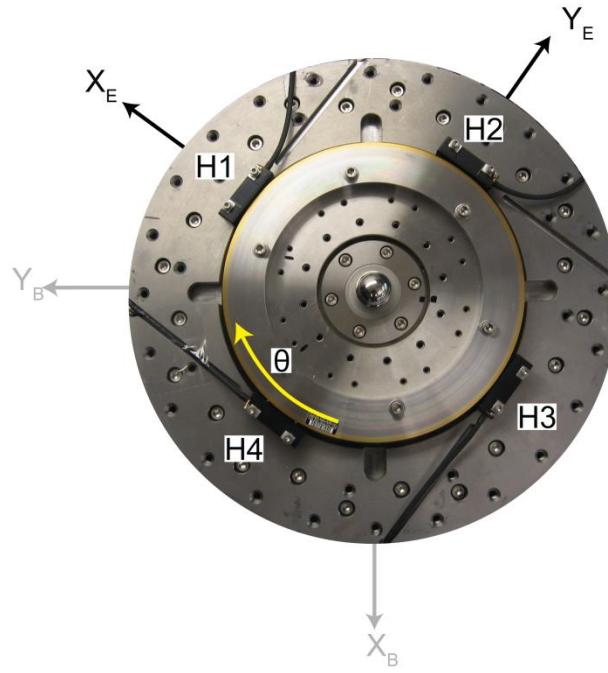


Figure 3.40. Setup (c): radial error motion measurement using four encoder scanning heads.

The calibrated error maps can be expressed as:

$$\begin{aligned}
 q_{H1}(\theta) &= g(\theta) & + & y_E(\theta) \\
 q_{H2}(\theta) &= g(\theta - \pi/2) & - & x_E(\theta) \\
 q_{H3}(\theta) &= g(\theta - \pi) & - & y_E(\theta) \\
 q_{H4}(\theta) &= g(\theta - 3\pi/2) & + & x_E(\theta)
 \end{aligned} \tag{3-27}$$

where $q_{H1}(\theta)$, $q_{H2}(\theta)$, $q_{H3}(\theta)$, and $q_{H4}(\theta)$ are encoder error maps from head H1, H2, H3 and H4 respectively; $g(\theta)$ is the scale grating error; $x_E(\theta)$ and $y_E(\theta)$ are the encoder ring scale radial motion in X_E and Y_E directions, respectively. By Fourier transform, these equations can be formulated as:

$$\begin{aligned}
 Q_{H1}(k) &= G(k) & + & Y_E(k) \\
 Q_{H2}(k) &= G(k)j^{-k} & - & X_E(k) \\
 Q_{H3}(k) &= G(k)j^{-2k} & - & Y_E(k) \\
 Q_{H4}(k) &= G(k)j^{-3k} & + & X_E(k)
 \end{aligned} \tag{3-28}$$

where $Q_{Hi}(k)$ is the k -th Fourier coefficient of $q_{Hi}(\theta)$, for $i=1, 2, 3, 4$; $G(k)$, $X_E(k)$, and $Y_E(k)$ are the k -th Fourier coefficients of $g(\theta)$, $x_E(\theta)$ and $y_E(\theta)$, respectively. Particularly, for $k=-1$, the spindle radial error motion can be calculated Eq. (3.28) as:

$$Q_{H1}(-1)j - Q_{H2}(-1) = X_E(-1) + jY_E(-1) = V_E(-1). \tag{3-29}$$

Figure 3.41 shows the calibrated encoder error maps of the four heads at 400 rpm. According to Eq. (3-29), the calculated fundamental radial error motion amplitude is $|V_E(-1)| = 50.4\text{nm}$, which matches the previous results obtained from the ball-probe and ring-probe setups.

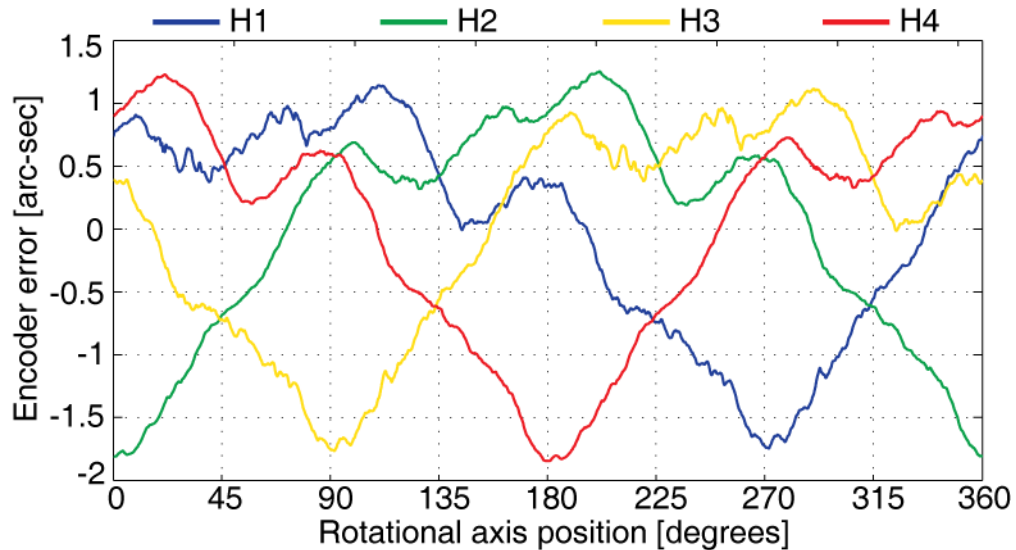


Figure 3.41. Calibrated encoder error maps of four encoder scanning heads at 400 rpm.

The radial error motion measurement using four encoder head setup is carried out as part of the “On-Axis self-calibration of angle encoders” research by Richard Graetz [24].

3.3.4. Comparison of three methods for spindle motion measurement

In this section, the fundamental spindle error motion obtained from the three setups is compared. To make the comparison, measurements in setup (a) and (c) frame are transformed to setup (c) frame. Figure 3.42 shows the relationship between the three frames.

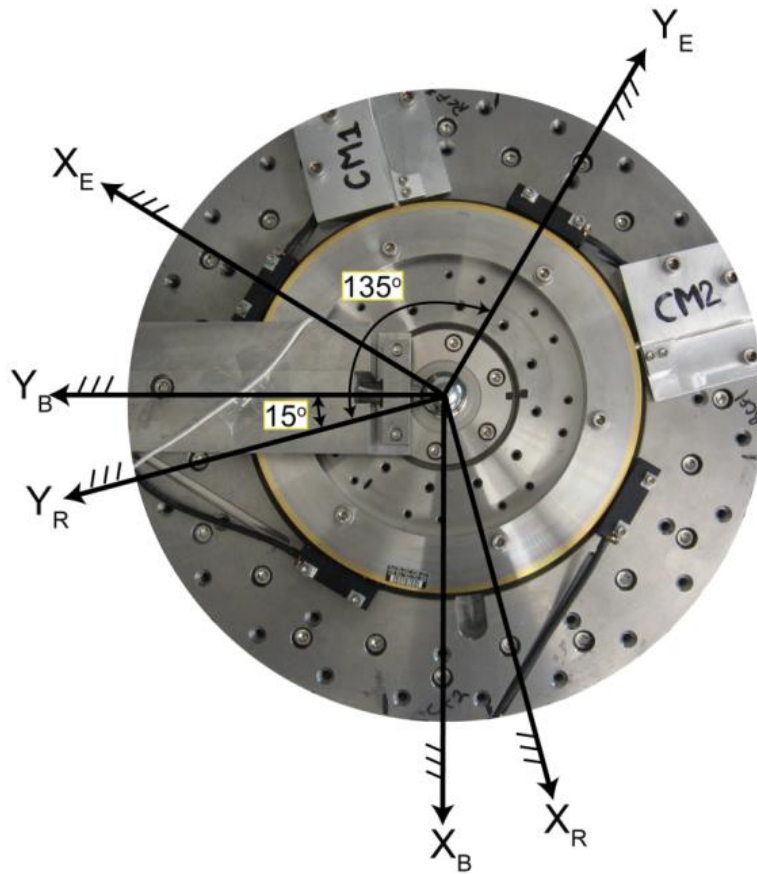


Figure 3.42. Relationship between the measurement coordinate of the three setups

For the ball-probe setup measurement, the transformation is:

$$v_R(\theta) = v_B(\theta)e^{j15} \quad (3-30)$$

where $v_R(\theta)$ is the test ball motion in the ring setup frame and $v_B(\theta)$ is the test ball motion in the ball setup frame. Similarly, for the encoder head setup, the transformation is:

$$v_R(\theta) = v_E(\theta)e^{j135} \quad (3-31)$$

Since this aerostatic bearing spindle has less than 1 nm asynchronous radial error motion, as shown in Figure 3.39, the fundamental radial error motion calculated from one revolution of data is nearly identical to that calculated from 500 revolutions. In order to efficiently compare the measurement results from three setups over a wide speed range, the spindle radial error motion is calculated while the spindle is freely slowing down using only one revolution.

Figure 3.43, shows that the fundamental radial error motion results from the three setups match within 2 nm. Also note that the results change with speed by only few nanometers. This comparison confirms that the fundamental radial error motion is a spindle motion property independent of test setup and artifact installation offset. The different phase of $V(-1)$ in the three

setups is caused by the deviation between the nominal probe/encoder installation location and their actual locations.

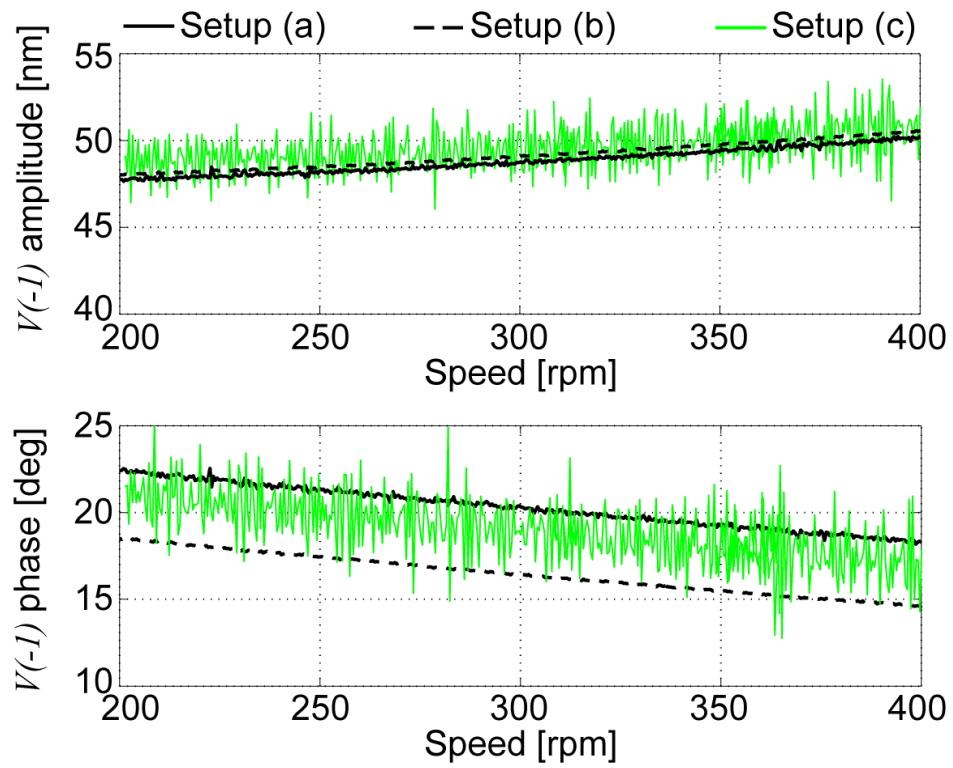


Figure 3.43. Comparison of the fundamental radial error motion measurement $V(-1)$ results from the three setups.

Chapter 4. Physical causes of fundamental error motion

So far in the thesis, the existence of fundamental error motion has been proved based on the kinematic analysis of the spindle motion in space. In this chapter, the aim is to understand what can cause the spindle rotor to move such that its rotation center move once-per-revolution in the opposite direction of spindle rotation.

In general, the axis of rotation would have no error motion if two conditions were satisfied:

- 1) The drive motor torque which causes rotation around the desired axis is the only force acting on the rotor.
- 2) All the other components of the structural loop have no motion relative to the gage head. This type of motion could be caused by external sources such as shop floor vibration exerting force on the spindle supporting structure.

As the spindle rotates, the motion of any component in the structural loop except the spindle is not synchronized with the rotation. In general, to have synchronous error motion, there should be interaction between a force acting on the spindle shaft and the stiffness element associated with it. Table 4-1 summarizes the type of interactions which causes synchronous error motion as discussed in [25].

Table 4-1. Types of interaction which cause spindle synchronous error motion.

Radial force	Stiffness element	Example on a lathe machine	Example on a boring machine
Fixed	Fixed	Cutting force and spindle support	Gravity and spindle support
	Rotating	Cutting force and work piece	Gravity and boring bar
Rotating	Fixed	Unbalance force and machine support	Cutting force and spindle support
	Rotating	Unbalance force and work piece	Cutting force and boring bar

The fundamental error motion is a synchronous motion and can only be caused by the forces acting on the spindle itself. In particular, this type of error motion is generated when the force acting on the shaft rotates once-per-revolution and the stiffness element is fixed. In all other cases given in Table 4-1, the resulting motion cannot be once-per-revolution.

Table 4-2 summarizes several examples where there is an interaction between a rotating radial force and a fixed stiffness element. Following subsections explain how each of these interactions can cause spindle to have fundamental error motion. Experimental results on both the Mori Seiki ball bearing spindle and Professional Instruments aerostatic bearing spindle will also be presented to confirm the analysis.

Table 4-2. Types of interaction which cause spindle fundamental radial error motion.

Rotating Radial force	Fixed stiffness element
Unbalance	Axis-asymmetric radial stiffness of the spindle bearing
	Axis-asymmetric stiffness of the supporting structure
Off axis load	Axis-asymmetric tilt stiffness of the spindle bearing
Rotor surface misalignment	Asymmetric bearing tilt stiffness
Magnetized rotor	Stator magnetic field

4.1. Interaction between unbalance and spindle bearing axis-asymmetric stiffness

Asymmetric bearing stiffness could be caused by the out-of-roundness of the stator surface. Figure 4.1(a) shows such an example with aerostatic bearings: the rotor is perfectly round, but the stator surface is elliptical. As a result, when the stator center O coincides with the rotor geometric center G at zero speed, the air gap in the X direction is bigger than that in the Y direction. Usually, aerostatic bearings with larger nominal gaps exhibit lower supporting stiffness under the same supply pressure. This axis-asymmetric air gap can result in axis-asymmetric radial stiffness, where the stiffness k_x in the X direction is smaller than the stiffness k_y in the Y direction.

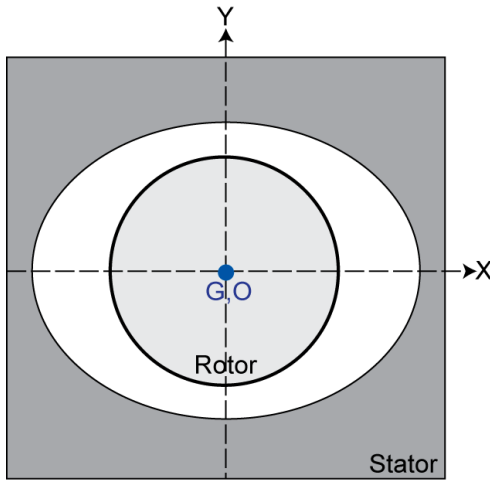


Figure 4.1. Axis symmetric air gap between rotor and stator of an aerostatic bearing spindle at zero speed.

When the radial stiffness is axis-asymmetric, the axis of rotation can exhibit fundamental radial error motion under a rotating excitation. In the following subsection, it is shown how unbalance can generate fundamental radial error motion.

4.1.1. Unbalance

As shown in Figure 4.2(a), when unbalance exists on the rotor, the inertial center of the rotor is at point E, which is offset from the rotor geometric center G by a distance δ . This unbalance could have been caused by factors such as installation misalignment of a direct drive motor or internal hole misalignment in the rotor. When the rotor rotates at constant speed ω , point G will deviate from the stator elliptical center O. Using the dynamics model shown in Figure 4.2(b), the force balance equations in X and Y directions will be

$$\begin{cases} m\ddot{x}_G + k_x x_G = m\delta\omega^2 \cos\theta \\ m\ddot{y}_G + k_y y_G = m\delta\omega^2 \sin\theta \end{cases} \quad (4-1)$$

Seeking solutions of the form $x_G = A \cos\theta$ and $y_G = B \sin\theta$, the steady state trajectory of point G can be calculated as:

$$\begin{cases} x_G = \frac{m\delta\omega^2}{k_x - m\omega^2} \cos\theta \\ y_G = \frac{m\delta\omega^2}{k_y - m\omega^2} \sin\theta \end{cases} \quad (4-2)$$

where θ is the angle between the X axis and the eccentricity vector (from point G to point E), and m is the rotor mass. The 2D motion of point G can be combined as a complex number:

$$\begin{aligned}
v_G &= x_G + jy_G \\
&= \frac{m\delta\omega^2}{2} \frac{k_y + k_x - 2m\omega^2}{(k_x - m\omega^2)(k_y - m\omega^2)} e^{j\theta} + \frac{m\delta\omega^2}{2} \frac{k_y - k_x}{(k_x - m\omega^2)(k_y - m\omega^2)} e^{-j\theta}
\end{aligned} \tag{4-3}$$

Therefore, the $k = +1$ motion component (eccentricity of the rotor geometric center G) is

$$\bar{V}_G(+1) = \frac{m\delta\omega^2}{2} \frac{k_y + k_x - 2m\omega^2}{(k_x - m\omega^2)(k_y - m\omega^2)} \tag{4-4}$$

and the $k = -1$ error motion component is

$$\bar{V}_G(-1) = \frac{m\delta\omega^2}{2} \frac{k_y - k_x}{(k_x - m\omega^2)(k_y - m\omega^2)} \tag{4-5}$$

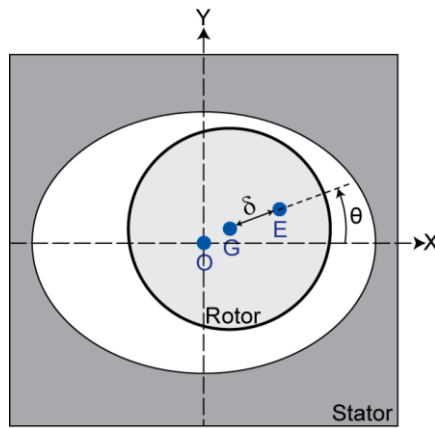
It is evident that the motion of point G is the superposition of two rotating vectors: $\bar{V}_G(+1)$ rotating in the same direction as the spindle rotation, and $\bar{V}_G(-1)$ rotating in the opposite

direction of spindle rotation. If the rotor behaves as the model presented, then at $\omega = \sqrt{\frac{k_x + k_y}{2m}}$,

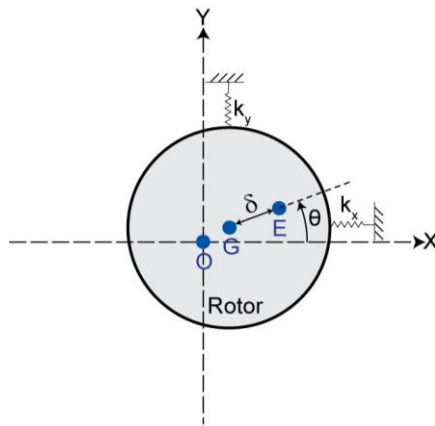
$\bar{V}_G(+1)$ component of rotor geometric center vanishes. In this speed, the rotation center will be the rotor geometric center moving once-per-revolution opposite to spindle rotation with amplitude of

$$\sqrt{\frac{\delta(k_y - k_x)}{2(k_y + k_x)}} \tag{4-6}$$

In the field of rotor dynamics, complex coordinates has previously been used the same way as the analysis in this section [26]. The general solution of homogenous equation of motion (no unbalance excitation $m\delta\omega^2 e^{j\theta}$) is expressed as sum of two vectors rotating in forward and backward direction. Both vectors rotate with the speed equal to the natural frequency of the rotor ($\sqrt{k/m}$). The motion in the forward direction is referred as circular forward whirl and the motion in the opposite direction is referred as circular backward whirl. Unbalance force cause an excitation force with a frequency equal to the spin speed of the rotor. The spin speed which coincides with the rotor natural frequency is referred as critical speed. At this speed the unbalance response of the rotor shows a peak.



a) The unbalance of the spindle



b) Dynamic model of the spindle

Figure 4.2. An unbalanced spindle with axis-asymmetric radial stiffness.

4.2. Interaction between unbalance and supporting structure axis-asymmetric stiffness

Most of the machine tools in use today have axis-asymmetric supporting stiffness. Figure 4.3 shows one example of a five axis machine where a spindle is installed on stacked X and Y linear stages. Since the moving mass in X and Y directions are very different, the supporting structure lateral stiffness becomes axis-asymmetric. Another example is a diamond turning machine shown in Figure 4.4(a) where an aerostatic spindle is installed on the X slide, which is driven by linear motor and guided by hydrostatic static bearings. As shown in Figure 4.4(b), in the vertical Y direction, the spindle housing support stiffness is determined by the hydrostatic bearing, while in the X direction the spindle housing support stiffness comes from the linear motor closed-loop

control. In general, the stiffness of hydrostatic bearing is very different from that of the linear motor control stiffness, resulting in axis-asymmetric stiffness.

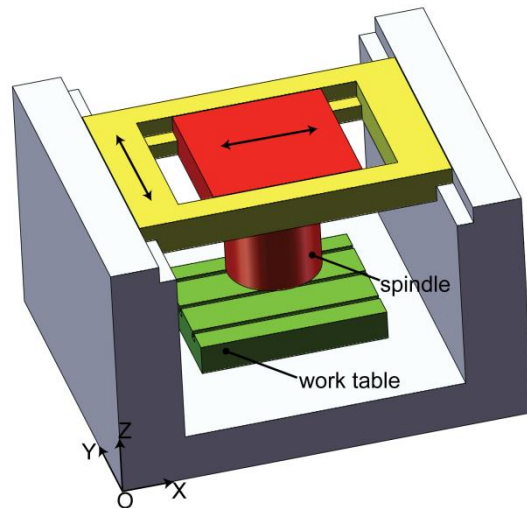


Figure 4.3. Axis-asymmetric stiffness of a five axis machine.

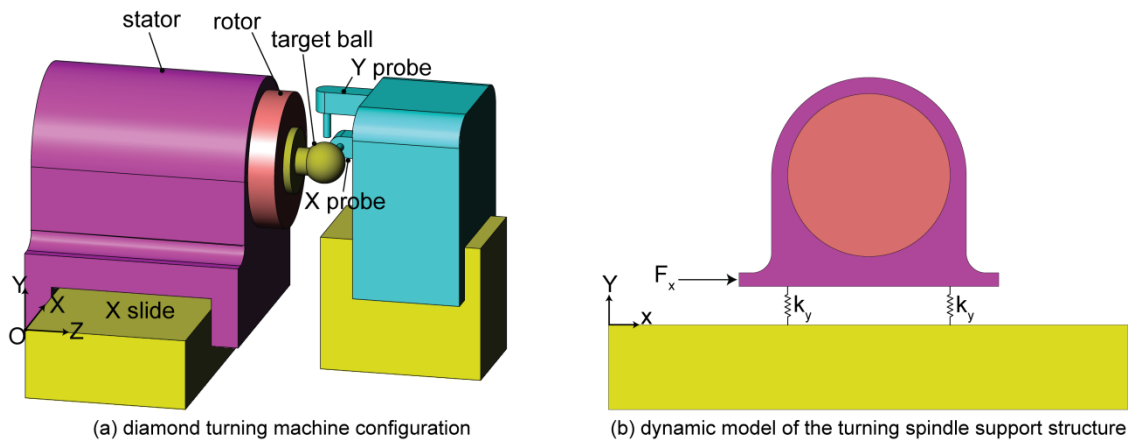


Figure 4.4. Axis-asymmetric stiffness of a diamond turning machine.

Similar to the analysis done in section 4.1, spindle will exhibit fundamental error motion due to interaction between unbalanced mass or rotating cutting force and the axis-asymmetric stiffness of the structure.

4.3. Interaction between off-axis load and spindle bearing axis-asymmetric tilt stiffness

As pointed out in [27], when the tilt stiffness of a vertical spindle is axis-asymmetric, any static unbalance of the spindle rotor can cause fundamental radial error motion. In Figure 4.5, the X-

axis tilt stiffness, k_x , is assumed unequal to the Y-axis tilt stiffness, k_y . A weight w is installed offset from the rotor geometric center O by a distance δ to simulate rotor static unbalance. The part applies a torque that rotates with the rotor. The test ball's center has height h above the tilt center. Assuming at this axial location the radial error motion is zero, the point ball's center P motion can be calculated as

$$\begin{cases} x_p = \frac{wh\delta \cos \theta}{k_x} \\ y_p = \frac{wh\delta \sin \theta}{k_y} \end{cases} \quad (4-7)$$

where θ is the angle between the X axis and the vector pointing from the rotor geometric center O to w . The 2D motion can be represented as:

$$v_p = x_p + jy_p = \frac{wh\delta(k_x + k_y)}{2k_x k_y} e^{j\theta} + \frac{wh\delta(k_x - k_y)}{2k_x k_y} e^{-j\theta} \quad (4-8)$$

Therefore, the $k = -1$ error motion component is:

$$\bar{V}_p(-1) = \frac{wh\delta(k_x - k_y)}{2k_x k_y} \quad (4-9)$$

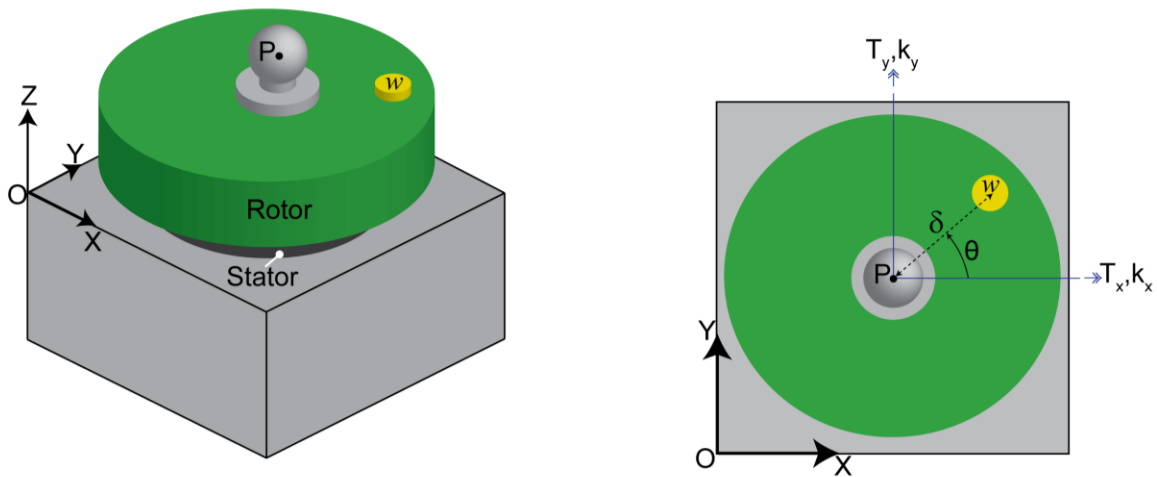


Figure 4.5. Off-axis load on a rotary table.

4.4. Rotor surface misalignment and spindle bearing axis-asymmetric tilt stiffness

Figure 4.6 presents an aerostatic spindle example where the rotor shaft is round but the thrust plate has an alignment angular error α . As shown in Figure 4.6(a), the stator inner surface has an elliptical shape with long axis along X and short axis along Y. As a result, the Y-axis tilt stiffness, k_y , is smaller than the X-axis tilt stiffness, k_x . Figure 4.6(b) shows the rotor at rotary position, $\theta = 0^\circ$. The mis-aligned thrust plate will generate a tilt angle β_y between the rotor surface center line and the stator surface center line. The equilibrium condition for the rotor internal moment is

$$k_y \beta_y = k_p (\alpha - \beta_y) \quad (4-10)$$

where k_p is the tilt stiffness between the thrust plate and its stator mating surface. Rearranging the terms in Eq. (4-10) gives:

$$\beta_y = \frac{k_p \alpha}{k_s + K_y} \quad (4-11)$$

when the rotor rotates 90 degrees, the tilt angle around the X axis can similarly be calculated as:

$$\beta_y = \frac{k_p \alpha}{k_s + k_x} \quad (4-12)$$

From this it can be seen that the shaft center line is moving in an elliptical cone once per revolution and the radial error motion will have $k = -1$ component.

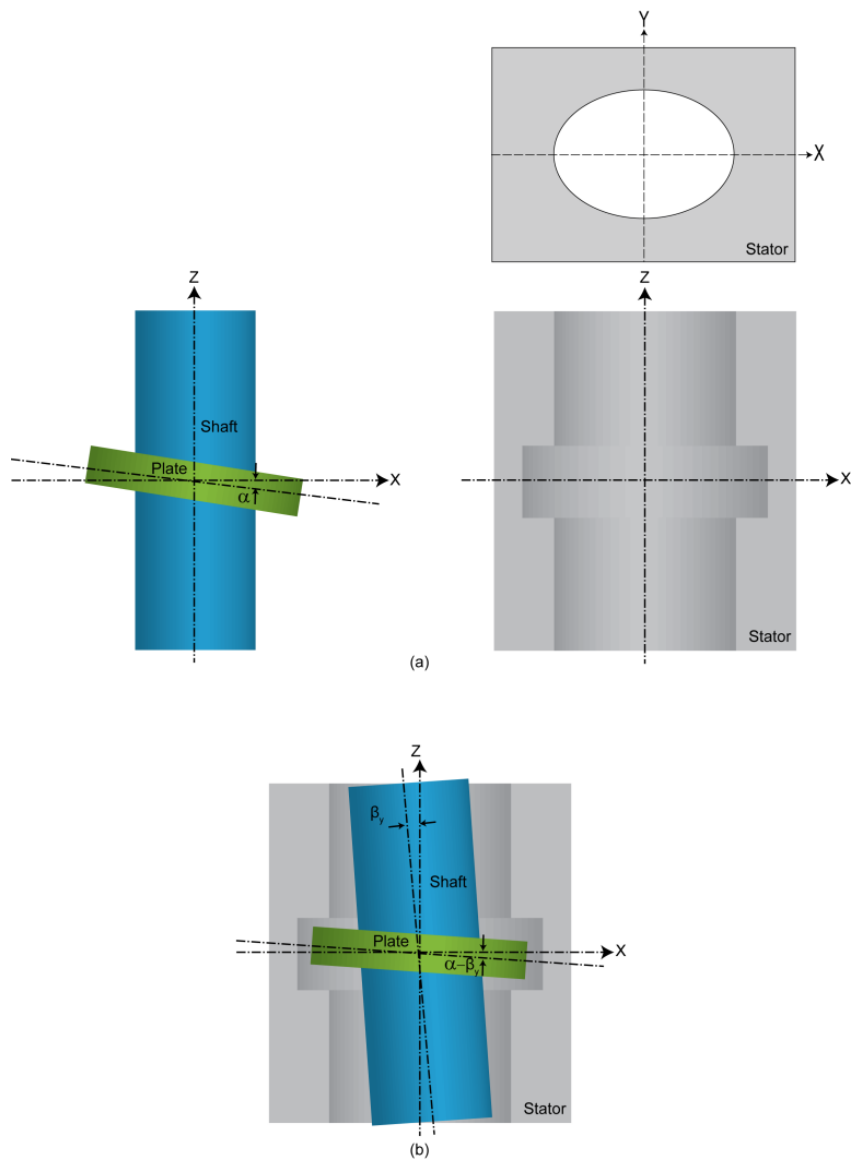


Figure 4.6. An aerostatic spindle with misaligned rotor thrust plate and elliptical stator surface. a) spindle rotor and stator. b) assembled rotor and stator.

4.5. Interaction between magnetized rotor and stator

Figure 4.7 shows an example of a spindle exhibiting fundamental error motion caused by magnetization of stator and rotor. Both the spindle rotor and the stator are somehow magnetized. The rotor has only one pair of poles and its magnetic field is once per revolution. The stator has two pairs of poles with magnetic field varying twice per revolution. The magnetic interaction force between the rotor and stator depends on the rotation angle. At $\theta = 0^\circ$ and $\theta = 180^\circ$, the rotor North pole is repelled from the stator North Pole. At $\theta = 90^\circ$ and $\theta = 270^\circ$ the rotor North pole is attracted toward the stator South pole. This interaction causes the rotor geometric center

C to move in the opposite direction of the rotor rotation. In this case, the rotor center C is the rotation center and its vector motion contains $k = -1$ component.

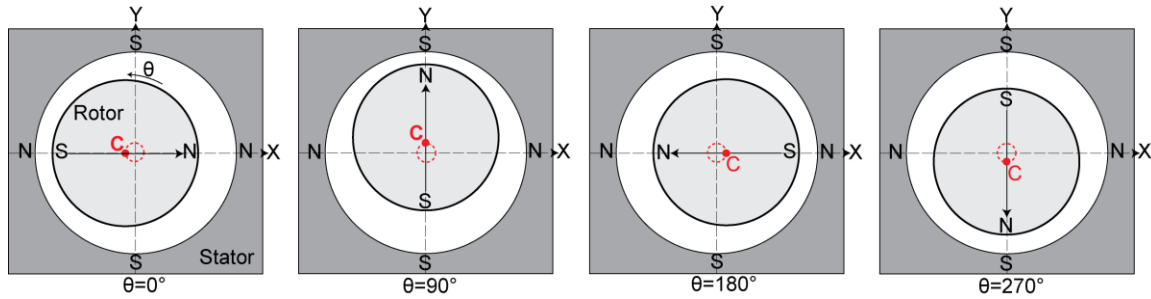
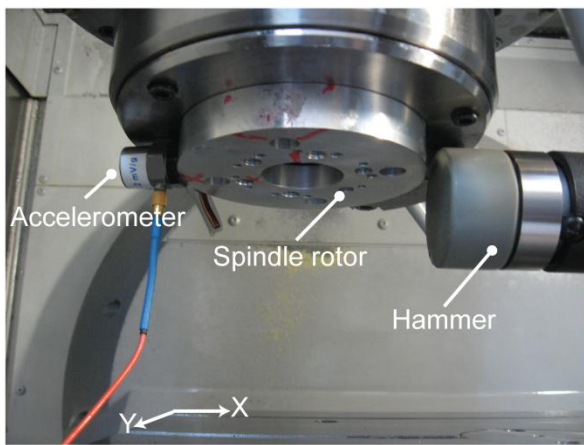


Figure 4.7. Interaction between a spindle stator and rotor's magnetic fields.

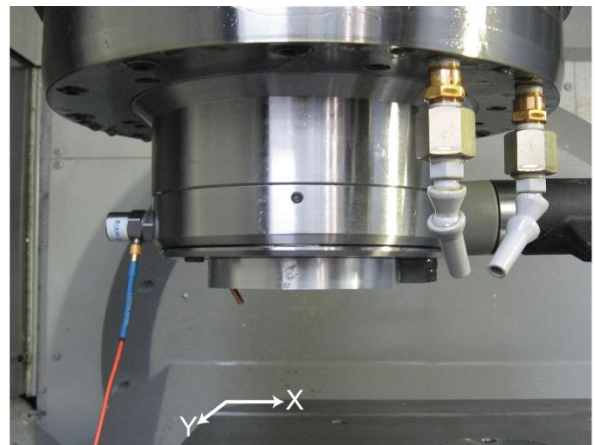
4.6. Physical cause experiments on the ball bearing spindle

The compliance of the Mori Seiki ball bearing spindle is tested with an impact hammer (IMI Sensors Model 086C41) and accelerometer (PCB Quartz Shear ICP Model 353B31). The spindle is positioned at the same place where it was located for the error motion measurements (Machine coordinates: X: 247.8mm, Y: -298.4mm Z: -435.8mm C: 0 Z: 0). Figure 4.8 shows the stiffness tests carried out on the spindle:

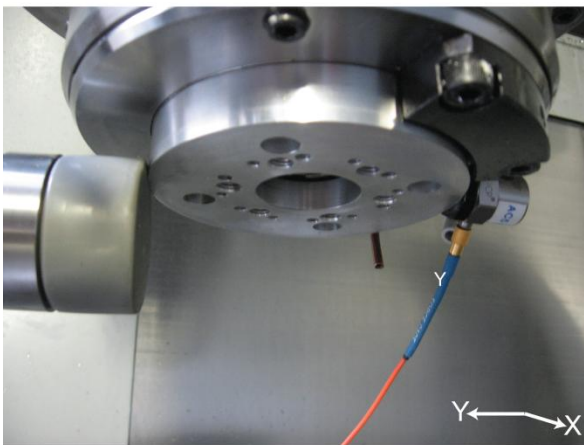
1. Test (i): Accelerometer mounted on rotor. Hammer hits on rotor (X direction).
2. Test (ii): Accelerometer mounted on rotor. Hammer hits on rotor (Y direction).
3. Test (iii): Accelerometer mounted on housing. Hammer hits on housing (X direction).
4. Test (iv): Accelerometer mounted on housing. Hammer hits on housing (Y direction).



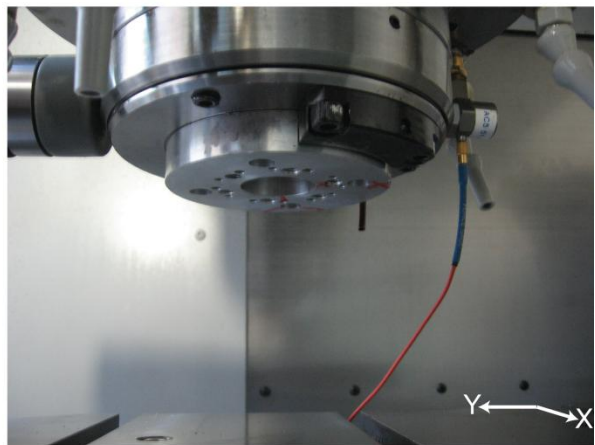
Test (i)



Test (iii)



Test (ii)



Test (iv)

Figure 4.8. Experimental setup for radial compliance measurement.

The measured compliance in X and Y directions are shown in Figure 4.9. The measurement on the spindle rotor and housing give similar results which indicate that asymmetry is caused by the stiffness between spindle housing and machine structure. This is reasonable since the spindle is installed on one rail in X direction and two rails in Y direction.

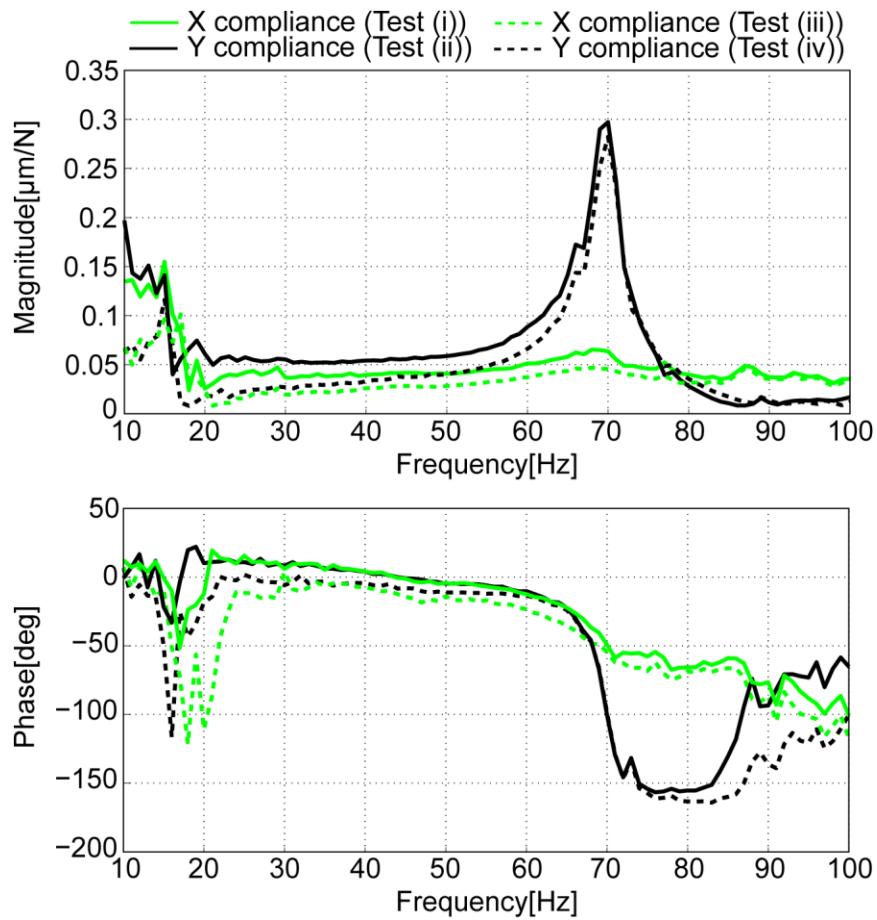


Figure 4.9. Spindle compliance measurement test results.

This axis-asymmetric structural compliance causes fundamental error motion under unbalance excitation. In particular at 70 Hz, which corresponds to 4200 rpm, the spindle structural compliance shows an evident resonance mode, with motion mainly in Y direction. This result matches the significant increase in $k = -1$ amplitude at 4000 rpm in Figure 3.24. Additional compliance test results on the Mori Seiki machine is presented in Appendix D.

4.7. Physical cause experiments on the aerostatic bearing spindle

4.7.1. Unbalance experiment

The effect of unbalance on the radial error motion of the aerostatic bearing spindle is investigated by placing a mass of 0.5kg on the shaft at the positions shown in Figure 4.10. All the mounting holes are at the radius of 50 mm. The mass of the spindle shaft including the parts mounted onto it is 52 kg. The spindle error motion is measured using the probes looking at the

encoder ring (setup (b) explained in chapter 3). The measurement is during the spindle freely slowing down and one revolution data at each speed is used to calculate the error motion.

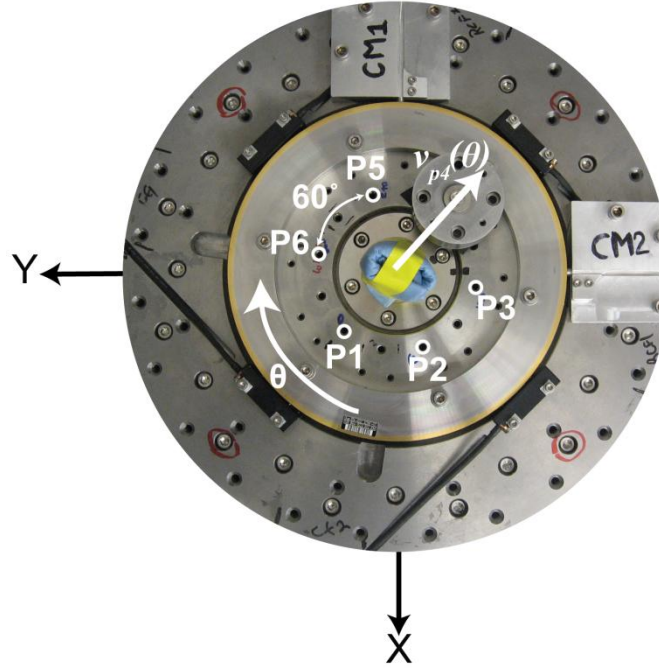


Figure 4.10. Unbalance mass mounted on the aerostatic spindle rotor.

When the mass is at position i , the radial error motion vector due to unbalance is

$$v_{P_i}(\theta - \psi_i) = v_{G(\text{mass at } P_i)}(\theta - \psi_i) - v_{G(\text{no mass})}(\theta) \quad (4-13)$$

where $v_G(\theta)$ is the motion vector measured by the probes. Neglecting harmonics higher than

$|k|=1$, $v_{P_i}(\theta)$ can be written as

$$v_{P_i}(\theta - \psi_i) = V_{P_i}(+1)e^{j\theta} + V_{P_i}(-1)e^{-j\theta} \quad (4-14)$$

Using Eq. (4-3), $V_{P_i}(+1)$ and $V_{P_i}(-1)$ Fourier coefficients are:

$$V_{P_i}(+1) = \frac{m\delta\omega^2}{2} \frac{k_y + k_x - 2m\omega^2}{(k_x - m\omega^2)(k_y - m\omega^2)} e^{-j\psi_i} \quad (4-15)$$

$$V_{P_i}(-1) = \frac{m\delta\omega^2}{2} \frac{k_y - k_x}{(k_x - m\omega^2)(k_y - m\omega^2)} e^{j\psi_i}$$

Since the mounting holes are placed 60 deg apart ($\psi_{i+1} - \psi_i = 60^\circ$), the relationship between

$V_{P_i}(+1)$ Fourier coefficients can be written as

$$V_{P_{i+1}}(+1) = V_{P_i}(+1)e^{-j60} \quad (4-16)$$

Figure 4.11 shows the magnitude of $V_{p_i}(+1)$ Fourier coefficient for each of the positions shown in Figure 4.10. As expected the magnitude increases as the spindle speed, ω , increases. The difference in $V_{p_i}(+1)$ magnitude at different positions is due temperature and pressure effects as discussed later in section 4.6.3.

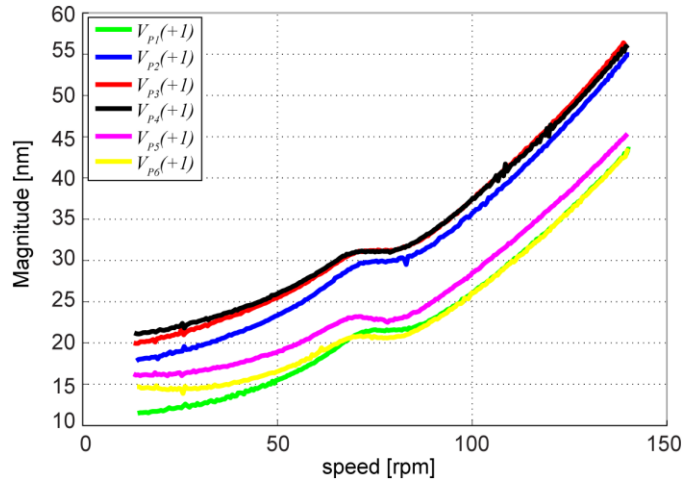


Figure 4.11. Effect of unbalance mass on magnitude of $V_{p_i}(+1)$.

Figure 4.12(a), shows the phase of $V_{p_i}(+1)$ Fourier coefficient for each of the tested positions. The difference in the phase of $V_{p_i}(+1)$ should be equal to 60 deg as shown in Eq. (4-19). To find the actual difference, the average phase value at each position is found and a least squares line is fit to the data (Figure 4.12(b)). The slope of this line is -55 deg due installation errors coming from the loose clearance of the mounting hole.

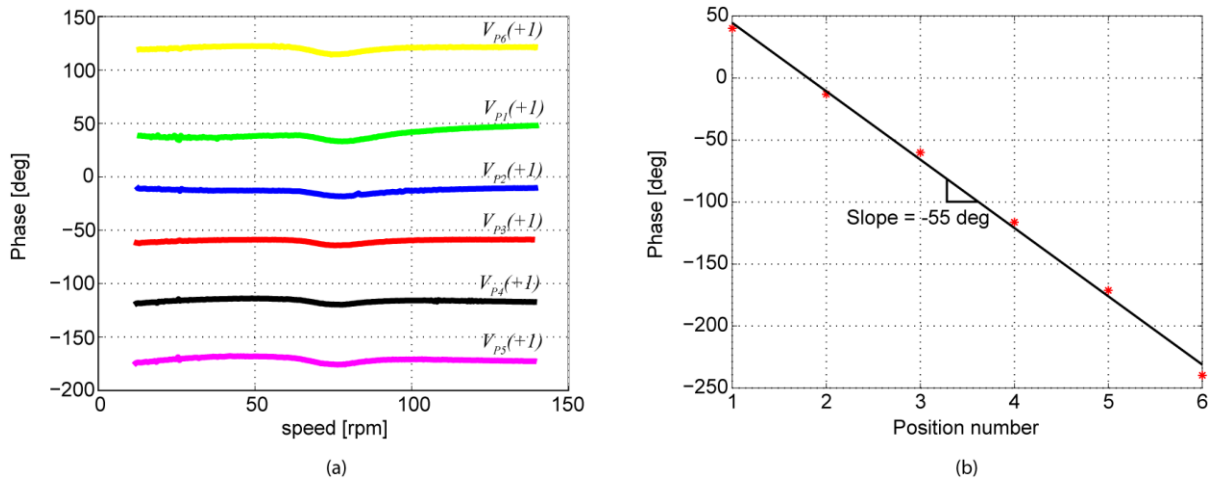


Figure 4.12. Effect of unbalance mass on phase of $V_{p_i}(+1)$. a) Phase of $V_{p_i}(+1)$ for all the mounting positions, b) difference between $V_{p_i}(+1)$ phases shown in (a).

The relationship between $V_{p_i}(-1)$ Fourier coefficients can be written as

$$V_{p_{i+1}}(-1) = V_{p_i}(-1)e^{j60} \quad (4-17)$$

Figure 4.13, shows the magnitude of $V_{p_i}(-1)$ Fourier coefficient for each of the positions shown in Figure 4.10.

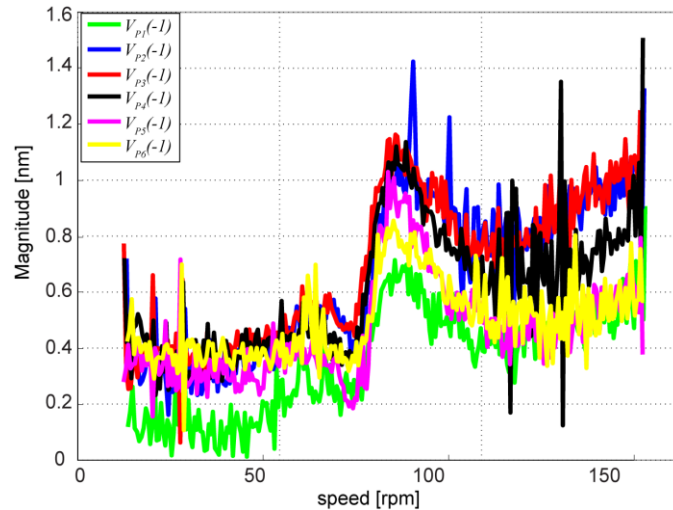


Figure 4.13. Effect of unbalance mass on magnitude of $V_{p_i}(-1)$.

This result shows that the unbalance mass has generated a very small $V_{p_i}(-1)$ component which indicates that the radial stiffness along X and Y directions are very similar. Figure 4.14(a) shows the phase of $V_{p_i}(-1)$ Fourier coefficient for each of the tested positions. The difference in the phase of $V_{p_i}(-1)$ should be equal to 60 deg as shown in Eq. (4-20). Similar to the method used for $V_{p_i}(+1)$ phase difference, the average phase value for each position is found and a least squares line is fit to the data (Figure 4.14(b)). The slope of this line is 50 deg due to installation errors coming from the loose clearance of the mounting holes. Comparing to the phase difference measured for $V_{p_i}(+1)$ Fourier coefficients, the results are not as accurate due to small effect of unbalance mass on generating $V_{p_i}(-1)$ component.

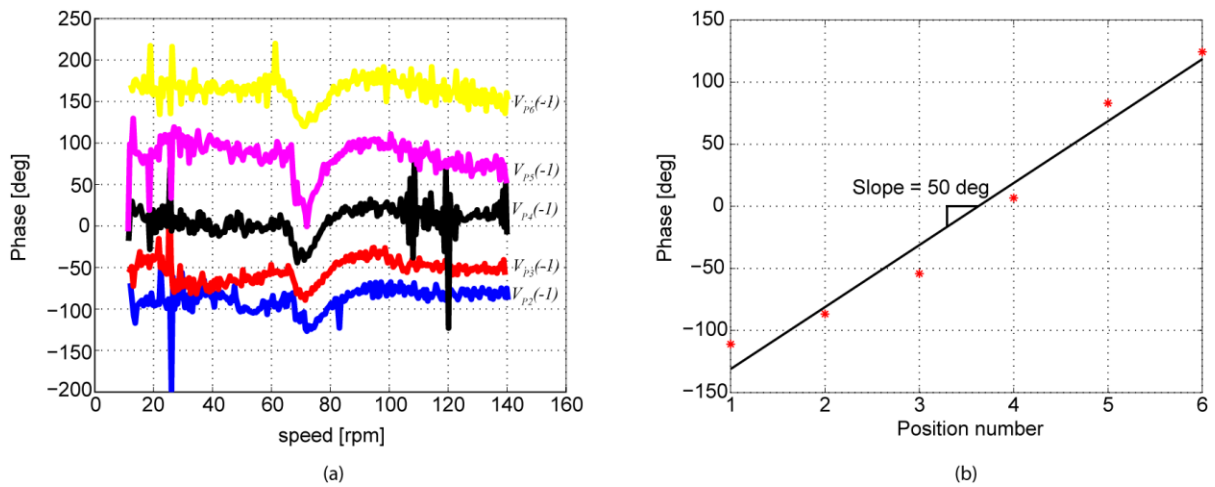


Figure 4.14. Effect of unbalance mass on phase of $V_{pi}(-1)$. a) Phase of $V_{pi}(-1)$ for all the mounting positions, b) difference between $V_{pi}(-1)$ phases shown in (a).

The sudden change in the magnitude of $V_{pi}(-1)$ and $V_{pi}(+1)$ around 70 rpm is due to the resonance frequency of the optical table where the spindle stator is mounted. Existence of $V_{pi}(-1)$ component shows that the aerostatic spindle has axis-asymmetric stiffness.

4.7.2. Tilt stiffness measurement

To verify the axis-asymmetric stiffness of the aerostatic bearing spindle, the static tilt stiffness is measured. Figure 4.15 shows the setup used in this experiment. The stiffness was measured along 6 different directions with angle β with respect to the stator reference point.

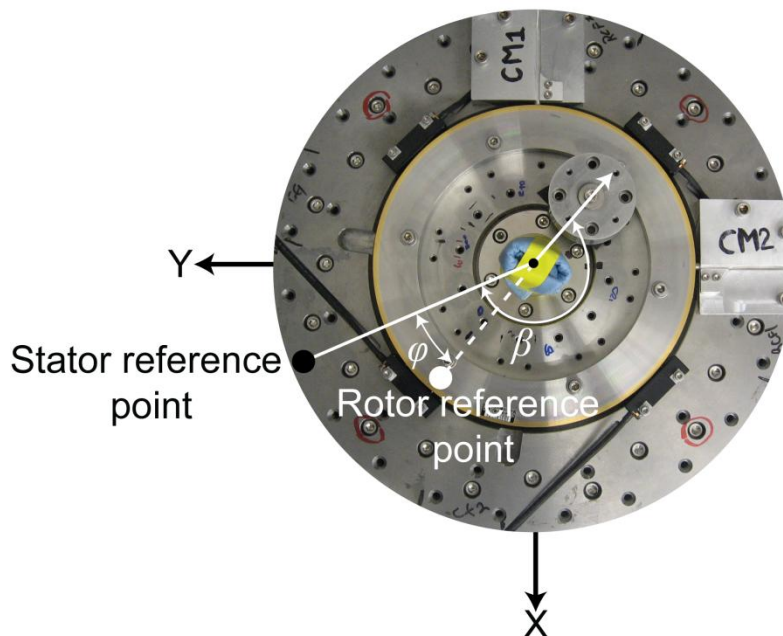
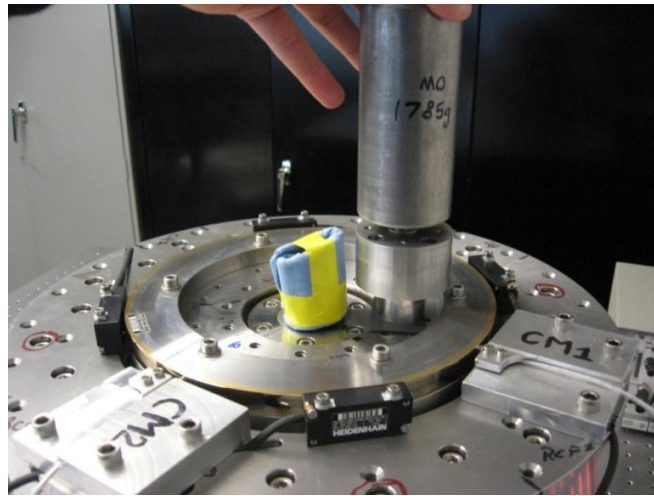
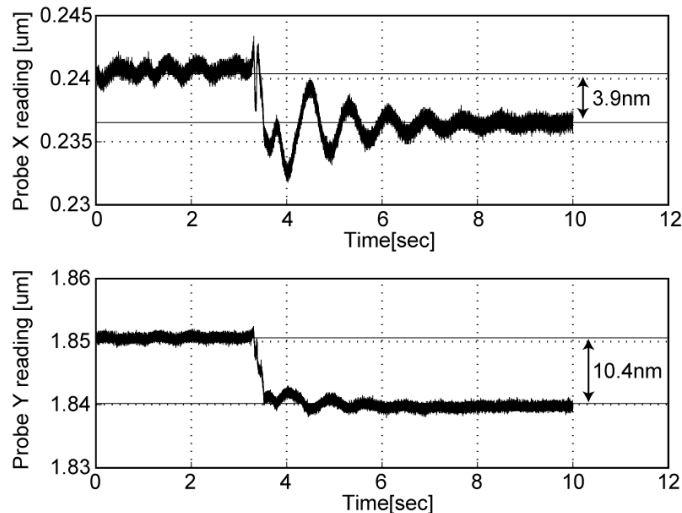


Figure 4.15. Experimental setup for tilt stiffness measurement.

To measure the tilt stiffness, mass was placed on the rotor and the static deformation of the rotor was measured using the capacitance probes (Figure 4.16(a)). This measurement is repeated for each direction ($\beta = 0^\circ, 60^\circ, \dots, 300^\circ$). Figure 4.16(b), shows one of the deformations measured using this method.



(a) Placing mass on the rotor



(b) Measured deformation of the rotor

Figure 4.16. Measuring static deformation of the the aerostatic spindle.

Above experiment was carried out for six different orientations of the rotor with respect to the stator. This orientation is given by φ which is the relative angle between the reference point on the rotor and the reference point on the stator (Figure 4.15). The measured tilt stiffness is shown in Figure 4.17.

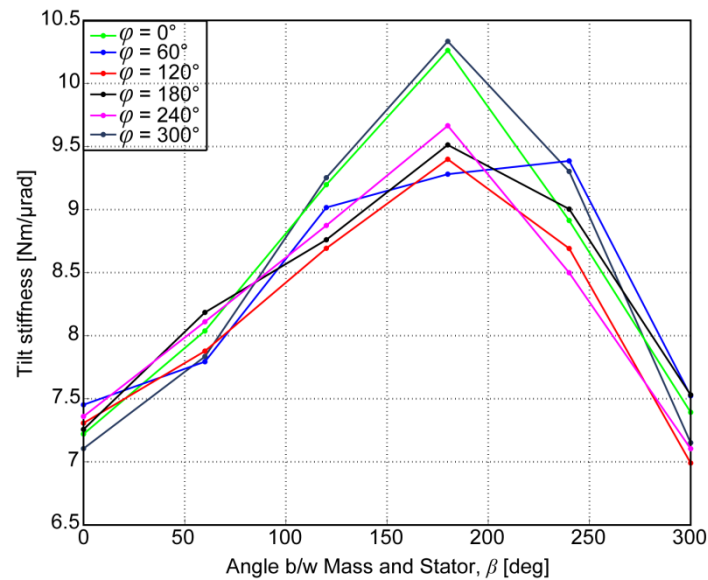


Figure 4.17. Static tilt stiffness of the aerostatic spindle.

Results show that at $\beta = 180^\circ$ the tilt stiffness is around $9.5 \text{ Nm}/\mu\text{rad}$ while at $\beta = 0^\circ$ the tilt stiffness is around $7.25 \text{ Nm}/\mu\text{rad}$. This does not make physical sense since it is not possible to have different stiffness along two directions which are 180 degrees apart. It is concluded that due to high tilt stiffness of the aerostatic bearing spindle, the method presented in the thesis is not adequate for measuring the tilt stiffness.

The other major cause of fundamental error motion on the aerostatic bearing spindle could be the non-round bearing surface shape. Investigating this cause is kept for future research.

4.7.3. Other physical factors affecting $V(-I)$

4.7.3.1. Loose bolt test

As pointed out in [28], the non flatness of the stator mating surfaces or the localized clamping force of the bolts can generate stress concentration and destroy the symmetry of the stator bearing surface. This distortion has an effect on the fundamental error motion of the spindle. This effect is tested by loosening 20 bolts which mounts ERA Head Mount Top onto ERA Head Mount Bottom (Figure 4.18). The four bolts closest to the encoder heads are left tightened to eliminate damaging the encoder ring.

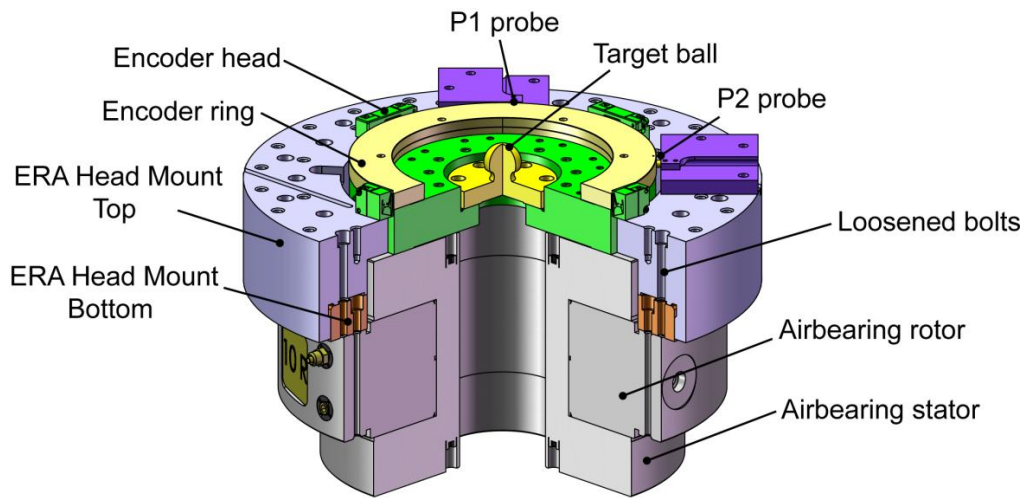


Figure 4.18. Aerostatic bearing assembly solid model.

The change in $V(-1)$ component before and after losing the bolts are shown in Figure 4.19. As expected changing the stress concentration on the stator affect the fundamental radial error motion by few nanometers, but this cannot be the major cause of the observed fundamental radial error motion.

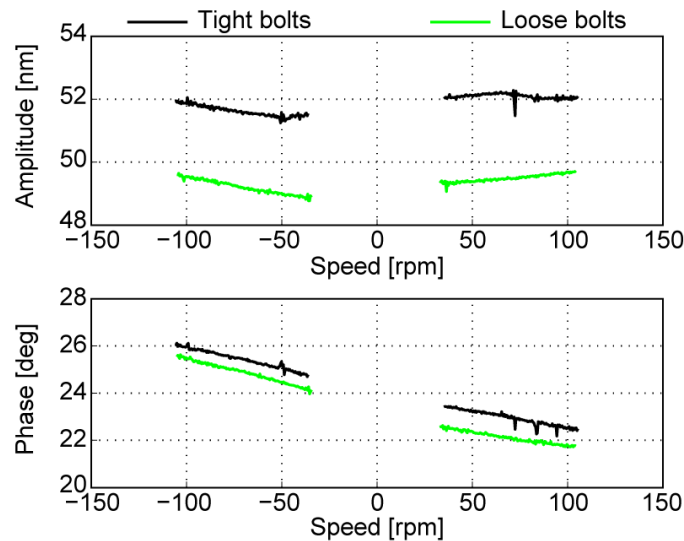


Figure 4.19. Effect of loosening the stator bolts on $V(-1)$.

4.7.3.2. Drift test

Environmental effects cause drift on the spindle motion measurement in the range of few nanometers. By placing the air bearing spindle on an optical table and regulating spindle air pressure, the effect of external vibrations and pressure change is minimized but some drift is still present in the measurement.

Figure 4.20(a) shows a 200 min test carried out to study the long-term drift of the spindle. The spindle is run for one hour at 400, 200, and 100 rpm and setup (b) is used to record the fundamental error motion, $V(-1)$. At the end of three hours, the fundamental component is also measured as the spindle freely slows down.

Figure 4.20(b) shows the $V(-1)$ motion drift at 200 rpm. The steps are related to cyclic change in the supply line pressure. In addition, as the spindle keeps rotating, its temperature rises. After one hour, the temperature rise has caused a 2% increase in the fundamental error motion. This shows that environmental effects such as change in temperature and spindle air pressure is negligible compared to the magnitude of 1 cpr motion.

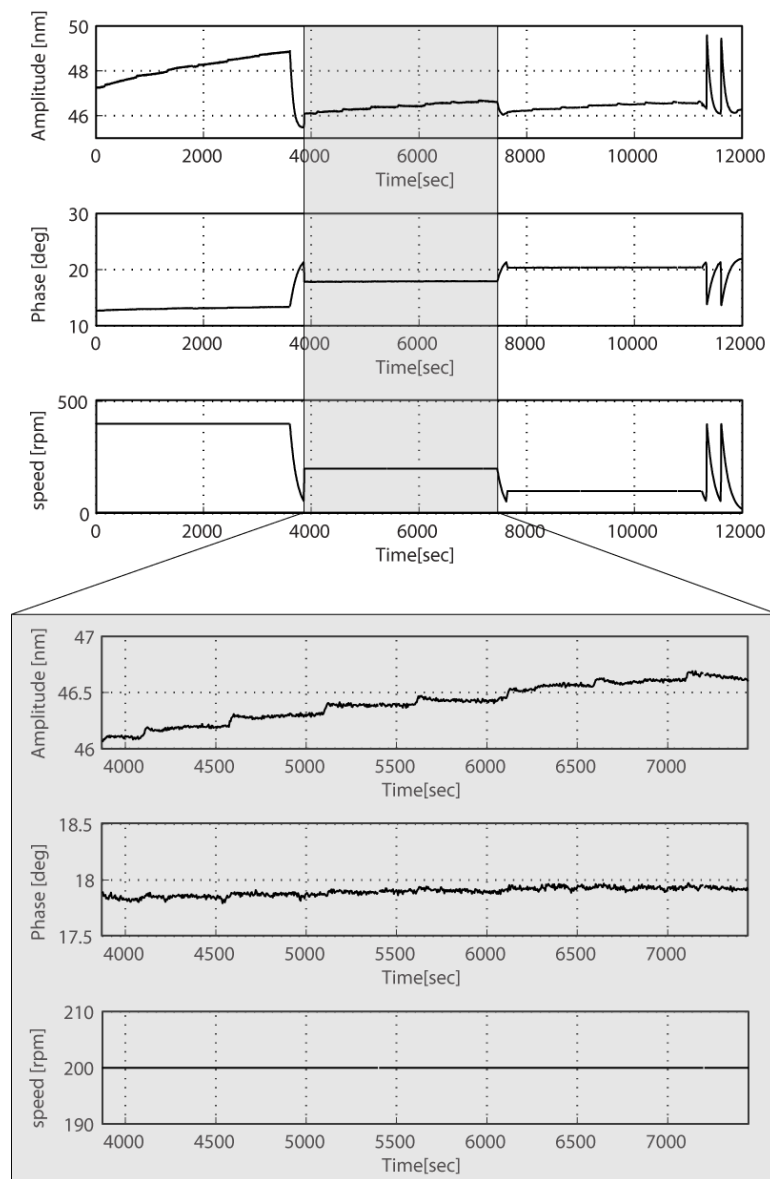


Figure 4.20. Change in $V(-1)$ due to temperature and pressure change.

Chapter 5. Conclusion and future work

5.1. Conclusion

This thesis presents a new 2D method for characterizing spindle radial error motion. This method provides a new framework in which the analysis can be carried out layer by layer:

- 1) The reference frame is chosen to measure the relative motion of the spindle with respect to a fixed frame.
- 2) The motion of a single point on the rotor is measured using two orthogonal probes.
- 3) Using complex Fourier series, the radial error motion of the spindle is extracted from the test point measurements.
- 4) The consequence of spindle radial error motion in different types of applications is analyzed.

This approach is quite different than the methods specified in the current standards which can only predict the consequence of spindle radial error motion in applications with a single sensitive direction (fixed or rotating). In comparison with these methods the new 2D method has the following advantages:

- 1) It can distinguish between radial error motion and its consequence and can be used to find the actual radial error motion of the spindle in two dimensions which is an application-independent geometric characteristic.
- 2) It can capture all the components of radial error motion including the fundamental error motion which is considered to be nonexistent in the current standards. The fundamental radial error motion is a vector motion rotating at the same speed as the spindle rotor but in the opposite direction.
- 3) It can give the consequence spindle radial error motion in all types of applications including the ones which have two sensitive directions.

Based on the application sensitive directions, spindle applications are categorized into three classes: applications with single fixed radial sensitive direction (SFSD), applications with single

rotating radial sensitive direction (SRSD), and applications with two radial sensitive directions (TSD). Examples of applications with TSD include axis-asymmetric pattern machining/measuring, and axis-symmetric pattern machining/measuring with multiple tools. For each application class, radial error motion consequence has been derived from 2D analysis.

The experimental results have demonstrated that both the ball bearing spindle and the aerostatic bearing spindle can have fundamental radial error motion. In these tests, the fundamental radial motion is the dominant component, and exhibits much larger amplitude than the rest of radial error motion components. The radial error motion calculated with the fixed direction method in the current standards is much smaller than the one calculated with the 2D method. This is due to the missed fundamental radial error motion component in the current standard. In the rotating direction, the radial error motion calculated with the rotating sensitive direction method in the current standards is also different from the one calculated with the 2D method. This difference is not as large as that in a fixed direction, because the $k=2$ cpr component missed in the rotating sensitive direction method of the current standard has a much smaller amplitude than the fundamental radial error motion for the spindles tested.

Fundamental radial error motion can be caused by the interaction between a rotating force and axis asymmetric stiffness of the spindle. On the ball bearing spindle, the axis asymmetric structure is verified by the impact hammer test. The significant increase at 4000 rpm occurs due to spindle speed coinciding with a structural resonance frequency.

5.2. Future work

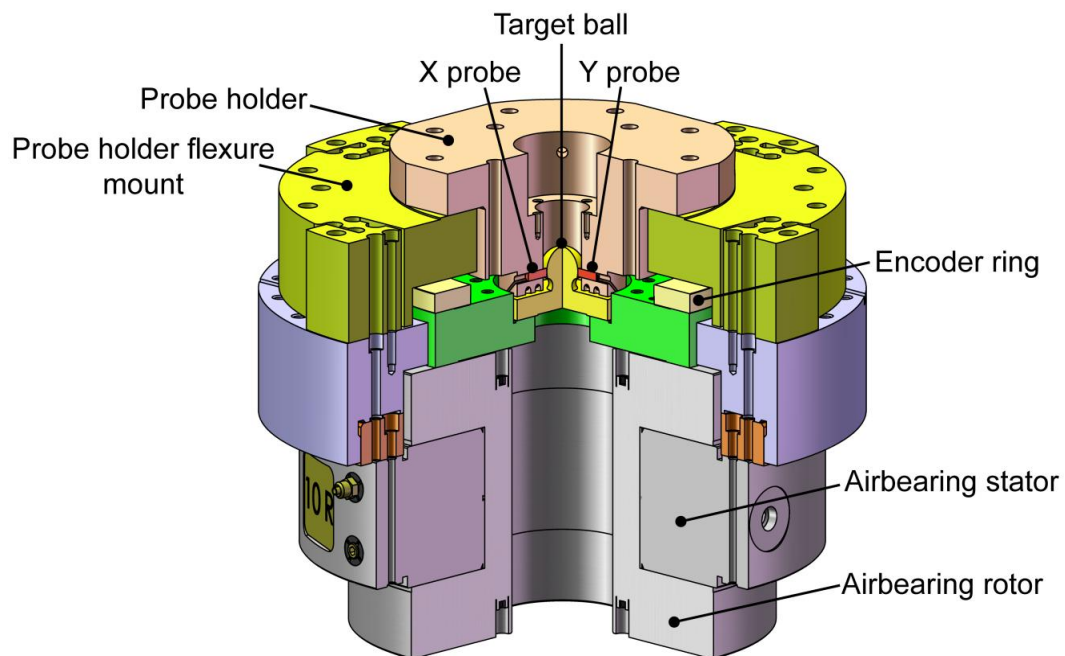
5.2.1. Experimental setup modifications

Setup (a) used in the aerostatic bearing spindle error motion measurements can be modified to reduce the effect of indexing and ball out-of-roundness on the error measurements. The mounting surface of the probe holder needs to be ground so that the height of the probes in X and Y directions become the same. This ensures that both probes measure the same ball out-of-roundness. In addition, to eliminate indexing errors for Donaldson reversal, the sliding bearing designed in [21] can be used to rotate the probe holder bolted to the stator top surface. Using the ERA encoder, the rotation angle can be precisely measured as the encoder read heads rotate around the fixed drum along with the probe holder.

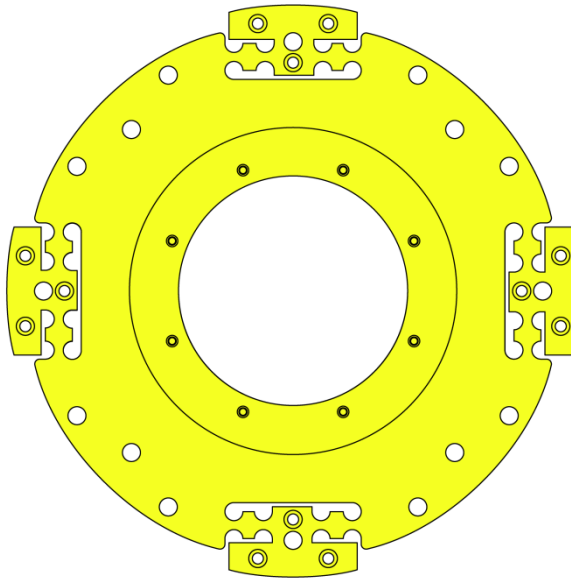
In addition, as pointed out by Donaldson [29], the interaction between the non-roundness of the rotor and the radial bearing stiffness could generate a twice-per-revolution “breathing” motion on the stator surface. As a result, the capacitance probes mounted on the stator move relative to the target and the breathing motion becomes part of spindle error motion measurement.

For the experimental results shown, the breathing effect is neglected since it has a twice per revolution rotational frequency and cannot contribute to the fundamental radial error motion $V(-1)$. On the aerostatic bearing spindle, three independent setups are used to measure the error motion. Setups (a) and (b) uses capacitance probes against a target to measure the spindle motion and are both sensitive to breathing effect. On the other hand, setup (c) extracts spindle error motion from the encoder error maps measured by the four read heads. Breathing effect has little effect on this setup as the error map is mostly sensitive to tangential motion of the read head. All three methods give the same $V(-1)$ measurement as shown in Figure 5.1 which confirms that breathing effect does not contribute to the fundamental error motion.

To measure all the components of spindle error motion accurately, a new probe holder is designed using flexures as shown in Figure 5.1. Under the breathing effect, the flexures elastically deform along with the stator surface but the probes remain stationary. Testing all the components of spindle radial error motion more accurately using this setup is kept for future research.



a) Modified aerostatic bearing assembly solid model



a) Probe holder flexure mount top view

Figure 5.1. Modifying aerostatic bearing spindle setup for more accurate radial error measurements.

5.2.2. Cause of fundamental radial error motion

Fundamental radial error motion is a new concept which has not been recognized in prior art. The ball bearing and aerostatic bearing spindles tested in this research both have this type of error motion. More tests need to be carried out on other types of spindles to find some design parameters which can reduce the fundamental error motion. In addition, the physical causes of this error motion needs to be investigated further. In particular, the fundamental radial error motion for the aerostatic bearing spindle is believed to be related to the bearing surface shape. Confirming this requires disassembling the spindle, which is not investigated in this paper and is kept for future research.

References

- [1]. C.P. Hemingray. A brief history of machine tool testing prior to 1945. *Precision Engineering* 1982; 4(1): 25-28
- [2]. ANSI/ASME B89.3.4M – 1985. *Axes of rotation: methods for specifying and testing*; 1985.
- [3]. ISO 230-7:2006. *Test code for machine tools—Part 7: geometric accuracy of axes of rotation*; 2006
- [4]. J. Tlustý. System and methods of testing machine tools. *Microtecnic* 1959; 13(4): 162-178.
- [5]. J. Bryan, R. Clouser, and E. Holland. Spindle accuracy. *American Machinist* 1967; 111(25):149-164.
- [6]. P. Vanherck, J. Peters. Digital axis of rotation measurements. *Annals of CIRP* 1973; 22(1).
- [7]. R. Donaldson. A simple method for separating spindle error from test ball roundness error. *Annals of CIRP* 1973; 21(1): 125-6.
- [8]. C. Evans, R. Hocken, W. Estler. Self-calibration: reversal, redundancy, error separation, and absolute testing. *Annals of CIRP* 1996; 45(2): 617-634.
- [9]. R. Spragg and D. Whitehouse. *Procedures of the Institute of Mechanical Engineers* 1968; 182: 397-405.
- [10]. S. Ozono. On a new method of roundness measurement based on the three points method. *Proceedings of the International Conference on Production Engineering* 1974; 457-462.
- [11]. K. Mistui. Development of a new measuring method for spindle rotation accuracy by three points method. *Proceedings of 23-rd International MTDR* 1982; 115-121.
- [12]. G. Zhang, R. Wang. Four-point method of roundness and spindle error measurements. *Annals of CIRP* 1993; 42(1): 593-596.
- [13]. M. Liebers, D. Oss, T. Sheridan. The master axis method for spindle error motion calibration. *Proceedings of ASPE Annual Conference*; 1998.
- [14]. J. Bryan. The history of axes of rotation and my recollections. *Proceedings of ASPE Summer Topical Meeting on Precision Bearings and Spindles*; 2007.
- [15]. E. Marsh. *Precision spindle metrology*. DEStech Publications; 2008.
- [16]. S. Noguchi, T. Tsukada, and A. Sakamoto. Evaluation method to determine radial accuracy of high-precision rotating spindle units. *Precision Engineering* 1995; 17(4): 266-273.

- [17]. ANSI B89.3.1 – 1972. Measurement of out-of-roundness; 1997.
- [18]. A. Oppenheim, A. Willsky, S. Nawab. Signals and systems. Prentice Hall; 1997.
- [19]. W. Srituravanich, L. Pan, Y. Wang, C. Sun, D. Bogy, X. Zhang. Flying plasmonic lens in the near field for high-speed nanolithography. *Nature Nanotechnology* 2008; 3(12): 733-737.
- [20]. R. Vallance, E. Marsh, and P. Smith. Effects of spherical targets on capacitive displacement measurements. *ASME Journal of Manufacturing Science* 2005; 126(4):822-829.
- [21]. D. Amin-Shahidi. Ultra-precise on-axis encoder self-calibration for fast rotary platforms. Master's thesis, University of British Columbia; 2008.
- [22]. R. Donaldson. A simple method for separating spindle error from test ball roundness error. *Annals of CIRP* 1972; 21(1): 125-6.
- [23]. X.-D. Lu, D.L. Trumper. On-axis self-calibration of rotary encoders. *Annals of the CIRP* 2007; 56(1).
- [24]. X.-D. Lu, R. Graetz, D. Amin-Shahidi, K. Smeds. On-Axis self-calibration of angle encoders. Accepted by *Annals of CIRP*; 2010.
- [25]. T. Dalrymple. The effects of asymmetrical radial stiffness in precision rotating machines: the duality of fixed and rotating sensitive directions. *Proceedings of ASPE Annual Conference*; 2004.
- [26]. G. Genta. Dynamics of rotating systems. Springer Science + Business Media, Inc; 2005.
- [27]. Personal email communication, James Bryan and Wolfgang Knapp. 2009.
- [28]. Personal email communication, Mel Liebers at Professional Instruments. 2009.
- [29]. Spindle blog constructed by X.-D. Lu for discussion among spindle experts. [Online], http://www.mech.ubc.ca/~xdlu/secure/euler/spindle_blog.htm

Appendices

Appendix A

Given N equally spaced points per revolution over M revolutions, the measurement at the n -th position $\theta = n \frac{2\pi}{N}$ in the m -th revolution can be expressed as for revolution i can be expressed as $p_m(n)$ where $0 \leq m \leq M-1$ and $0 \leq n \leq N-1$.

There are three methods to find synchronous component of the measurement data:

1) Averaging in time domain, 2) averaging in frequency domain and 3) extracting harmonics which are integer multiples of total number of revolutions, M . In this appendix, it is shown that these three methods are mathematically the same.

- 1) Averaging in time domain: In this method, the synchronous measurement can be found by averaging the data at each rotary position over the number of revolutions recorded:

$$\bar{p}(n) = \frac{1}{M} \sum_{i=0}^{M-1} p_m(n) \quad (\text{A-1})$$

- 2) Averaging in frequency domain: In this method the time domain data of each revolution is transferred to frequency domain using FFT. The Fourier coefficient for the data in the m -th revolution is expressed as

$$P_m[k] = \frac{1}{N} \sum_{n=0}^{N-1} p_m(n) e^{-j \frac{2\pi kn}{N}}, \quad 0 \leq k \leq N-1 \quad (\text{A-2})$$

The Fourier coefficients of the synchronous measurement can then be found by averaging each harmonic over all the revolutions:

$$\bar{P}[k] = \frac{1}{M} \sum_{m=0}^{M-1} P_m[k], \quad 0 \leq k \leq N-1 \quad (\text{A-3})$$

Accordingly, the synchronous measurement can be reconstructed from its Fourier coefficients as

$$\bar{p}(n) = \frac{1}{N} \sum_{k=0}^{N-1} \bar{P}[k] e^{j \frac{2\pi kn}{N}}, \quad 0 \leq n \leq N-1 \quad (\text{A-4})$$

- 3) Extracting synchronous harmonics in frequency domain: In this method FFT is applied to all the revolutions' data at once to get a single frequency spectrum.

$$P[k] = \frac{1}{NM} \sum_{n=0}^{N-1} \sum_{m=0}^{M-1} p_m(n) e^{-j \frac{2\pi k(n+mN)}{NM}}, \quad 0 \leq k \leq NM - 1 \quad (\text{A-5})$$

By dropping the $P[k]$ components that are not multiple of M (non-integer components), the synchronous component Fourier coefficients can be derived

$$\bar{P}[k] = P[kM], \quad 0 \leq k \leq N - 1 \quad (\text{A-6})$$

These three methods are mathematically identical. Consequently, all three methods give the same synchronous measurement. Once the synchronous motion component is extracted, asynchronous motion can be easily found using the following equation:

$$\tilde{p}[\theta] = p[\theta] - \bar{p}[\theta] \quad (\text{A-7})$$

Appendix B

Figure B.1. shows an example polar plot. The polar plot contains both DC , r_0 , and fundamental component, $a \cos(\theta - \psi)$:

$$r(\theta) = r_0 + a \cos(\theta - \psi) + e(\theta) \quad (\text{B-1})$$

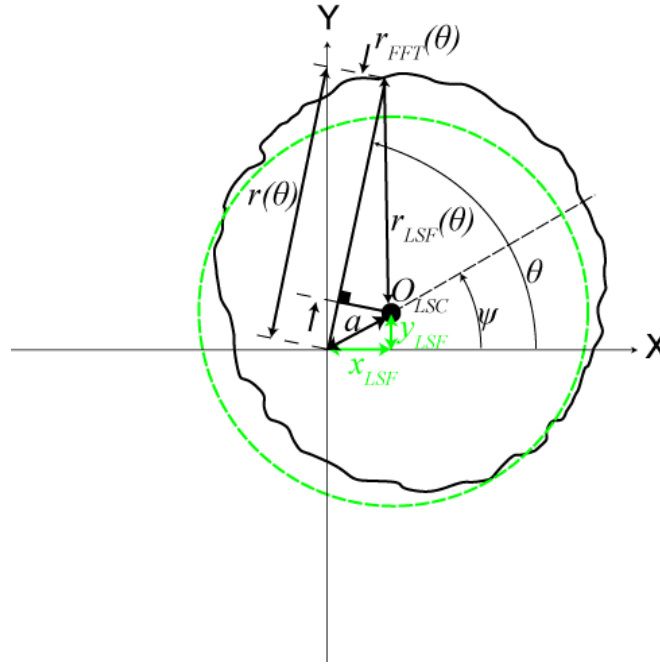


Figure B. 1. Example polar plot with centering error.

In the least squares fitting method, the least squares circle of the polar plot is found and the deviation of the polar plot from this circle is specified as radial error motion. The coordinates of the least squares circle center O_{LSF} are:

$$x_{LSF} = \frac{2}{N} \sum_{\theta=0}^{\frac{2\pi(N-1)}{N}} r(\theta) \cos(\theta) = \frac{2}{N} \sum_{\theta=0}^{\frac{2\pi(N-1)}{N}} a \cos(\theta - \psi) \cos(\theta) = a \cos(\psi) \quad (\text{B-2})$$

$$y_{LSF} = \frac{2}{N} \sum_{\theta=0}^{\frac{2\pi(N-1)}{N}} r(\theta) \sin(\theta) = \frac{2}{N} \sum_{\theta=0}^{\frac{2\pi(N-1)}{N}} a \sin(\theta - \psi) \sin(\theta) = a \sin(\psi) \quad (\text{B-3})$$

Once the Least square center is found, the polar plot relative to the new center is $r_{LSF}(\theta)$ as shown in Figure B.1.

In the frequency domain method, the fundamental component of the polar plot measurement given in Eq. (B-1) is removed from the measurement to get

$$r_{FFT}(\theta) = r_0 + e(\theta) \tag{B-4}$$

Figure B.1 shows that $r_{LSF}(\theta)$ and $r_{FFT}(\theta)$ are two sides of a right angle rectangle; therefore their difference is

$$r_{LSF}(\theta) - r_{FFT}(\theta) \cong \frac{(a \sin(\theta - \psi))^2}{2r_0} \tag{B-5}$$

The difference approaches zero as the base circle radius, r_0 , increases.

Appendix C

In practice, the test ball motion is usually measured at N equally-spaced rotary positions per revolution. Over M revolutions, the ball motion is recorded as:

$$v_p[n] = x_p[n] + jy_p[n], \text{ for } 1 \leq n \leq MN \quad (\text{C-1})$$

where $x_p[n]$ and $y_p[n]$ are X and Y motion of the test ball's center P at n -th rotary position.

The synchronous motion of the ball center P is calculated as the synchronized average value over M revolutions

$$\begin{aligned} \bar{v}_p[n] &= \frac{1}{M} \sum_{i=0}^{M-1} v_p[n + Ni] = \bar{x}_p[n] + j\bar{y}_p[n] \\ \bar{x}_p[n] &= \frac{1}{M} \sum_{i=0}^{M-1} x_p[n + Ni] \\ \bar{y}_p[n] &= \frac{1}{M} \sum_{i=0}^{M-1} y_p[n + Ni] \end{aligned} \quad (\text{C-2})$$

which represents the motion components repeatable at integer cycles per revolution. The asynchronous $\tilde{v}_p[n]$ is accordingly calculated as:

$$\tilde{v}_p[n] = v_p[n] - \bar{v}_p[n] \quad (\text{C-3})$$

which represents the motion components not repeatable at integer cycles per revolution.

As a complex-valued function, the k -th Fourier coefficient of $\bar{v}_p[n]$ can be calculated as:

$$\bar{V}_p[k] = \frac{1}{N} \sum_{n=1}^N \bar{v}_p[n] e^{-j2kn\pi/N}, \quad 1 \leq k \leq N \quad (\text{C-4})$$

The motion of the spindle rotation center C at the specified axial location can be found as

$$v_C[n] = v_p[n] - \bar{V}_p[1] e^{j2n\pi/N} \quad (\text{C-5})$$

The synchronous and asynchronous motions of the spindle rotation center C can be calculated from the test point P motion as:

$$\bar{v}_C[n] = \bar{v}_p[n] - \bar{V}_p[1] e^{j2n\pi/N} \quad (\text{C-6})$$

$$\tilde{v}_C[n] = \tilde{v}_p[n] \quad (\text{C-7})$$

Further, the location of rotation center average point A is

$$v_A = \bar{V}_p[N] \quad (\text{C-8})$$

The Fourier coefficients of the test ball's center's 2D motion have the following physical meanings:

1. $\bar{V}_p[1]$ is the vector pointing from spindle rotation center C to the test ball's center when the spindle is at zero position, at the specified axial location.
2. Two rotation centers at two specified axial locations set the axis of rotation
3. $\bar{V}_p[N]$ is the position of the rotation center average point (the average position of spindle rotation center C) in the reference coordinate axes.
4. Two rotation center average points at two specified axial locations set the axis average line.

The spindle radial error motion is:

$$\begin{aligned}\varepsilon[n] &= v_C[n] - v_A \\ &= v_p[n] - \bar{V}_p[1]e^{j2n\pi/N} - \bar{V}_p[N]\end{aligned}\quad (C-9)$$

The synchronous and asynchronous radial error motions of the test spindle are

$$\bar{\varepsilon}[n] = \sum_{k=2}^{N-1} \bar{V}_p[k] e^{j2kn\pi/N} \quad (C-10)$$

$$\tilde{\varepsilon}[n] = \tilde{v}_p[n] \quad (C-11)$$

The following quantities can be used to characterize the spindle radial error motion:

- (a) RMS synchronous error motion

$$\bar{\varepsilon}_{RMS} = \sqrt{\sum_{k=2}^{N-1} |\bar{V}_p(k)|^2} \quad (C-12)$$

- (b) RMS asynchronous error motion

$$\tilde{\varepsilon}_{RMS} = \sqrt{\frac{1}{MN} \sum_{n=1}^{MN} |\tilde{v}_p[n]|^2} \quad (C-13)$$

- (c) RMS total error motion

$$\varepsilon_{RMS} = \sqrt{\bar{\varepsilon}_{RMS}^2 + \tilde{\varepsilon}_{RMS}^2} \quad (C-14)$$

- (d) maximum synchronous error motion

$$\bar{\varepsilon}_{MAX} = \max_{1 \leq n \leq N} |\varepsilon[n]| \quad (C-15)$$

- (e) maximum asynchronous error motion

$$\tilde{\varepsilon}_{MAX} = \max_{1 \leq n \leq NM} |\tilde{\varepsilon}[n]| = \max_{1 \leq n \leq NM} |\tilde{v}_p[n]| \quad (C-16)$$

- (f) maximum total error motion

$$\varepsilon_{MAX} = \max_{1 \leq n \leq NM} |\varepsilon[n]| \quad (C-17)$$

The spindle radial motion in a specified radial direction is:

$$\varepsilon_{\phi}[n] = \text{Re} \left[\varepsilon[n] e^{-j\phi} \right] \quad (C-18)$$

where ϕ is the angle between the X-axis and the sensitive direction. In applications with single fixed radial sensitive direction (SFSD), the synchronous radial error motion consequence $\bar{A}_{\phi_0}[n]$ and asynchronous radial error motion $\tilde{A}_{\phi_0}[n]$ are:

$$\bar{A}_{\phi_0}[n] = \text{Re} \left[\sum_{k=2}^{N-2} \bar{V}_p[k] e^{j(k2n\pi / N - \phi_0)} \right] \quad (C-19)$$

$$\tilde{A}_{\phi_0}[n] = \tilde{x}_p[n] \cos \phi_0 + \tilde{y}_p[n] \sin \phi_0 \quad (C-20)$$

where ϕ_0 is the angle between the sensitive direction and the X axis. In applications with single rotating radial sensitive direction (SRSD), the synchronous error motion consequence $\bar{A}_{\theta}[n]$ and asynchronous radial error motion consequence $\tilde{A}_{\theta}[n]$ are:

$$\bar{A}_{\theta}[n] = \text{Re} \left[\sum_{k=3}^{N-1} \bar{V}_p[k] e^{j(k-1)2n\pi / N} \right] \quad (C-21)$$

$$\tilde{A}_{\theta}[n] = \tilde{x}_p[n] \cos \theta + \tilde{y}_p[n] \sin \theta \quad (C-22)$$

For applications with 2D radial sensitive directions (TSD), the synchronous error motion consequence $\bar{A}[n]$ and asynchronous radial error motion consequence $\tilde{A}[n]$ are:

$$\bar{A}[n] = \bar{\varepsilon}[n] = \sum_{k=2}^{N-1} \bar{V}_p[k] e^{j2kn\pi / N} \quad (C-23)$$

and

$$\tilde{A}[n] = \tilde{\varepsilon}[n] = \tilde{v}_p[n] \quad (C-24)$$

Appendix D

In addition to the compliance results shown in Figure 4.9, Chapter 4, Mori Seiki spindle was tested using another impact hammer (PCB ICP Model 086C05) and same accelerometer (PCB Quartz Shear ICP Model 353B31). This impact hammer can excite frequency range of 50 to 500 Hz on the machine. The spindle is positioned at the same place where it was located for the error motion measurements (Machine coordinates: X: 247.8mm, Y: -298.4mm Z: -435.8mm C: 0 Z: 0). In all the tests, accelerometer is mounted on the rotor on the opposite side of where the hammer hits. Figure D. 1 shows the stiffness tests carried out on the spindle:

1. Test (x_0): Rotor at $\theta = 0^\circ$ with respect to stator. Hammer hits on rotor in X direction.
2. Test (x_90): Rotor at $\theta = 90^\circ$ with respect to stator. Hammer hits on rotor in X direction.
3. Test (y_90): Rotor at $\theta = 90^\circ$ with respect to stator.. Hammer hits on rotor in Y direction.
4. Test (y_180): Rotor at $\theta = 180^\circ$ with respect to stator.. Hammer hits on rotor in Y direction.

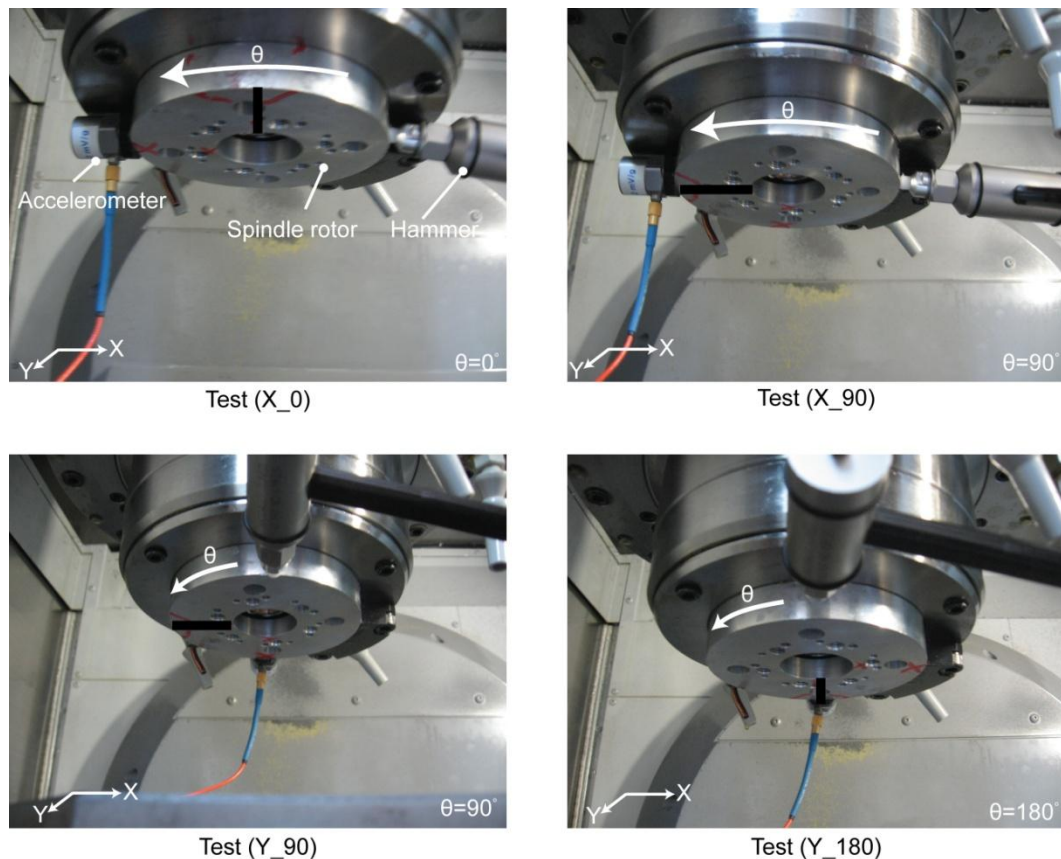


Figure D. 1. Experimental setup for radial compliance measurement.

The measured compliance in X and Y directions are shown in Figure D.2.

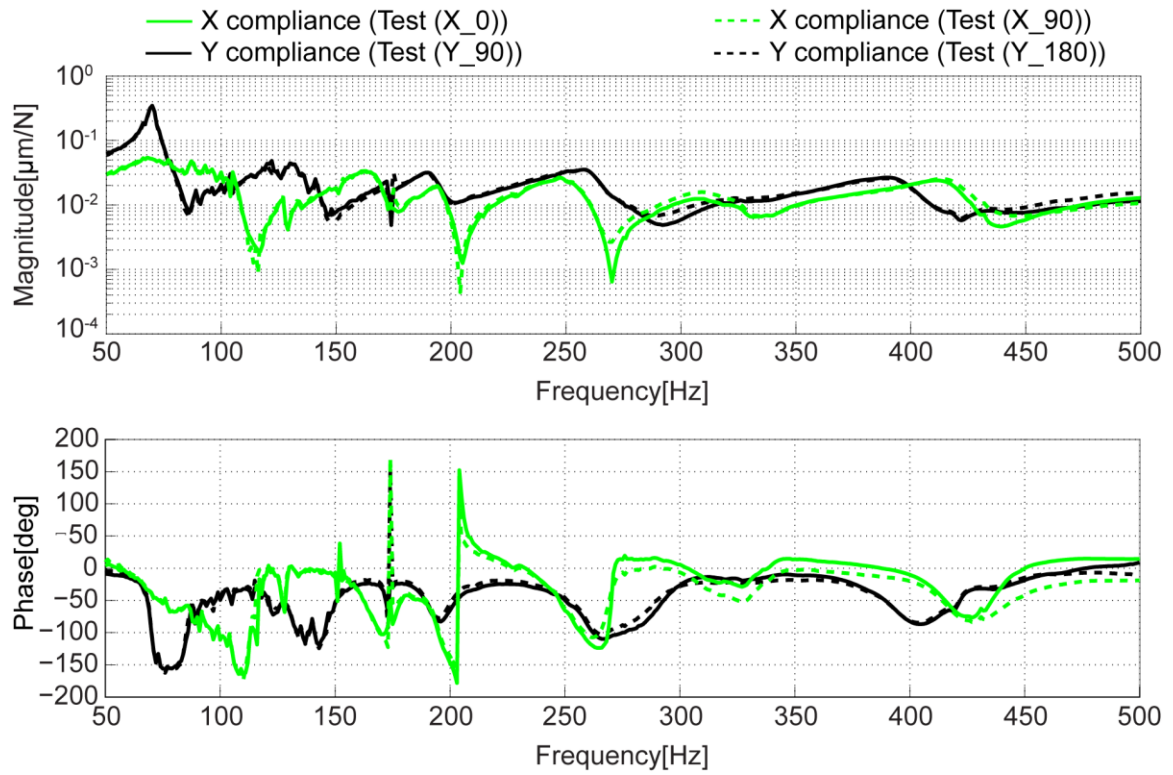


Figure D. 2. Spindle compliance measurement test results.

As shown in the above Figure, changing the orientation of the rotor with respect to the stator does not affect the measured compliance. On the other hand, the measured compliance in X and Y directions are different which shows the spindle has axis-asymmetric stiffness.